REPORT DOCUMENTATION PAGE

Form Approved OMB No. 0704-0188

1. REPORT DATE *(DD-MM-YYYY)*	2. REPORT TYPE	3. DATES COVERED *(From - To)*
05-24-2001	Technical Report	02-15-2001 to 05-24-2001

4. TITLE AND SUBTITLE

MicroAUV - MEMS Report

5a. CONTRACT NUMBER
MDA972-01-C-0011

5b. GRANT NUMBER
na

5c. PROGRAM ELEMENT NUMBER
Milestone 3

6. AUTHOR(S)
John Cranney, Dave Stone
(with help from Dr. Denise Wilson, Todd Massengil @ Univ of Washington)

5d. PROJECT NUMBER
na

5e. TASK NUMBER
na

5f. WORK UNIT NUMBER
na

7. PERFORMING ORGANIZATION NAME(S) AND ADDRESS(ES)

USTLAB
(Unmanned Systems Technology Laboratory, Inc)
510 Clearwater Loop No. 2
Post Falls ID 83835

8. PERFORMING ORGANIZATION REPORT NUMBER
USTLAB TR - 01.003

9. SPONSORING / MONITORING AGENCY NAME(S) AND ADDRESS(ES)

Defense Advanced Research Projects Agency
Advanced Technology Office
ATTN: Mr. Charles Nurse
3701 North Fairfax Drive
Arlington, VA 22203-1714

10. SPONSOR/MONITOR'S ACRONYM(S)

11. SPONSOR/MONITOR'S REPORT NUMBER(S)

12. DISTRIBUTION / AVAILABILITY STATEMENT

Approved for public release; distribution unlimited

20010530 054

13. SUPPLEMENTARY NOTES

14. ABSTRACT

This Microminiature Autonomous Underwater Vehicle (MicroAUV) Project pursues a viable design of a very small AUV. Current MEMS industry miniaturization of electronics enables a "Clean Sheet" design of an underwater vehicle that could achieve an "order of magnitude" improvement in specific endurance (range per pound mass of vehicle) over currently fielded systems. Specifically, the authors target a 2-15 lb MicroAUV that can demonstrate a 20 nautical mile per pound mass specific range capability. The design includes a 20% payload fraction in weight and/or volume and a ~10% margin for payload power. MicroAUV shall provide the capability and endurance of other vehicles currently in the fleet and between 80 ~ 200 lbm displacement.

An initial report was provided to underscore the scope of possibility within the opportunity described above. This report summarizes results obtained in the previous report, and discusses work this period. This report captures the mass, volume, and power budgets of the components that provide the functional make up of MicroAUV, as well as the analysis of performance efficiencies and possible margins depending on vehicle geometric design and propulsive system.

In the previous report, the author's documented the viability of an 8 lbm MicroAUV with a net specific endurance capability of between 3 and 15 Nautical miles per pound mass, depending on operating profile and design margin resolutions. This report expands on the analyses and narrows the focus of the right sized vehicle.

The author's pose that the "physics of the small" provides the possibility of a unique opportunity to improve endurance. Specifically, the analyses completed herein identify the possibility of a "sweet spot" of vehicle hull diameter, length, shape and prismatic coefficient, wherein at low Reynolds Number (10^4–10^5) flow, a minimum hydrodynamic drag might be achievable.

15. SUBJECT TERMS

16. SECURITY CLASSIFICATION OF:			17. LIMITATION OF ABSTRACT	18. NUMBER OF PAGES	19a. NAME OF RESPONSIBLE PERSON
a. REPORT	b. ABSTRACT	c. THIS PAGE			john cranney
unclas	unclas	unclas	UL	55	19b. TELEPHONE NUMBER *(include area code)* 208 777 4736

Unmanned Systems Technology Laboratory, Inc.
510 Clearwater Loop #2
Post Falls, ID 83854

USTLAB TR – 01.003 MAY 2001
Milestone 3, *"Six (6) Month Technical Report"*

μAUV – MEMS Report

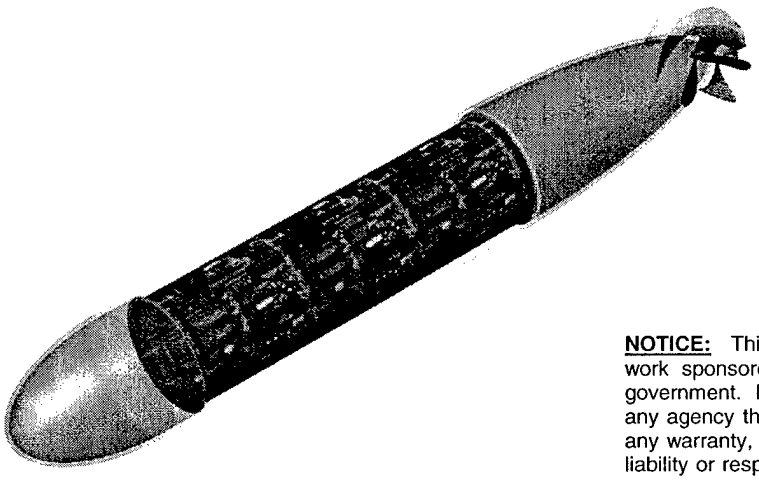

by john cranney, david l. stone,

with help from
Dr. Denise Wilson and Todd Massengill
University of Washington

Sponsored by:
Defense Advanced Research Projects Agency
(Micro AUV)
ARPA Order No. K017/19
Issued by DARPA/CMD under contract No.
MDA972-01-C-0011, CLIN 0001AA

Abstract

This Microminiature Autonomous Underwater Vehicle (MicroAUV) Project pursues a viable design of a very small AUV. Current MEMS industry miniaturization of electronics enables a "Clean Sheet" design of an underwater vehicle that could achieve an "order of magnitude" improvement in specific endurance (range per pound mass of vehicle) over currently fielded systems. Specifically, the authors target a 2-15 lb MicroAUV that can demonstrate a 20 nautical mile per pound mass specific range capability. The design includes a 20% payload fraction in weight and/or volume and a ~10% margin for payload power. MicroAUV shall provide the capability and endurance of other vehicles currently in the fleet and between 80 ~ 200 lbm displacement.

An initial report[1], was provided to underscore the scope of possibility within the opportunity described above. This report summarizes results obtained in the previous report, and discusses work this period. This report captures the mass, volume, and power budgets of the components that provide the functional make up of MicroAUV, as well as the analysis of performance efficiencies and possible margins depending on vehicle geometric design and propulsive system.

In the previous report, the author's documented the viability of an 8 lbm MicroAUV with a net specific endurance capability of between 3 and 15 Nautical miles per pound mass, depending on operating profile and design margin resolutions. This report expands on the analyses and narrows the focus of the right sized vehicle.

The author's pose that the "physics of the small" provides the possibility of a unique opportunity to improve endurance. Specifically, the analyses completed herein identify the possibility of a "sweet spot" of vehicle hull diameter, length, shape and prismatic coefficient, wherein at low Reynolds Number (10^4–10^5) flow, a minimum hydrodynamic drag might be achievable.

This report provides "Our milestone 3 requirement to the design and viability of right sizing MicroAUV to achieve 20 Nm/lbm displacement."

Report Disclaimer: "The views and conclusions contained in this document are those of the authors and should not be interpreted as representing the official policies, either express or implied, of the Defense Advance Research Projects Agency or the U. S. Government."

Declaration of Technical Data Conformity: The Contractor, USTLAB, hereby declares that, to the best of its knowledge and belief, the technical data delivered herewith under Contract No. MDA972-01-C-0011 is complete, accurate, and complies with all requirements of the contract.

Salient Findings: Salient findings of this study include the following items tied to the demonstrable milestone objectives from the contract. The index on the following page highlights these objectives in blue to identify the page numbers where the reader can find the supporting discussion.

DEMONSTRABLE MILESTONE OBJECTIVE	SALIENT FINDING(S)
Document the theoretical foundation to define the right MicroAUV size & design	Achieving 10 Nm/lb specific endurance is possible. There may be a optimum sized AUV platform hull shape, subject to some verification of results from hydrodynamic analyses discussed herein.
Identify MEMS Components to be used, including how and why	Short range "imaging" for MicroAUV requires only a small amount of acoustic imaging system power and a MEMS sonar design may be both viable and sufficient.
Identify Technical Issues	
Recommend "proof of concept" demos	
Refine and Defend task for additional work (Option 1)	Provided by separate report

INDEX

ATTACHMENTS

List of Figures

EXECUTIVE SUMMARY:

GOAL:

Our MicroAUV Team goal remains,

"Use current MEMS technologies to "clean sheet" design an optimally sized micro miniature autonomous underwater vehicle (MicroAUV) that can achieve 20 Nm/lbm displacement."

FIGURE 1. SPECIFIC ENDURANCE GOAL

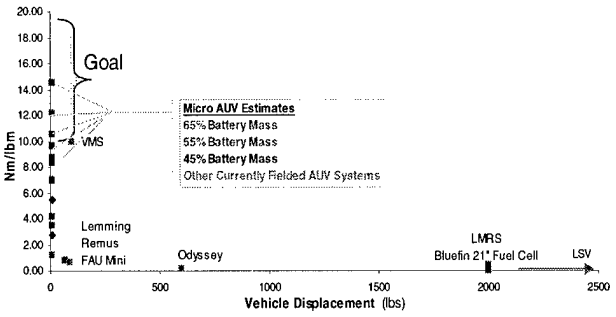

Further, through miniaturization, design MicroAUV to provide better than 10x the current 'endurance per lbm of vehicle displacement' over other vehicles currently in the fleet. Specifically, we seek to build MicroAUV at 2~15 lbm displacement and with 20 Nm/lbm endurance to achieve the functions of larger vehicles of 80~200 lbm displacement which have ~1 Nm/lbm displacement. Figure 1 shows our goal relative to other platforms.

REVIEW OF INITIAL WORK:

In our initial analysis, we focused on two technology thrusts:

- capture the scope of MEMS technology to be applied to MicroAUV design
- conceptualize point designs & estimate endurance for 3 operating profiles:
  - i. steady state level flight;
  - ii. high maneuvering, and;
  - iii. a 50%-50% mix.

FIGURE 2. INITIAL SPECIFIC ENDURANCE RESULTS

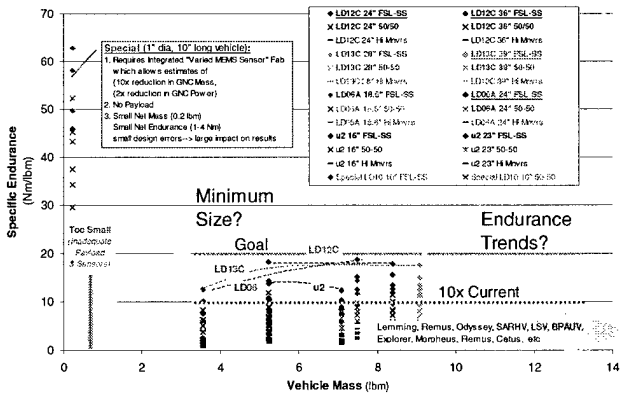

Using 10 point designs of specific vehicle configurations, our analysis showed that trends will exist (Figure 2). However, the small slope in the analysis set indicates that a more thorough examination of the trade space is warranted to:

- discern the exact trend(s) direction
- find an optimum vehicle configuration

NEW WORK - HYDRODYNAMICS:

We observed that at 5 kts (8.5 fps) forward velocity, a ~12" long vehicle provides for flow with Reynolds Numbers (N_R) as low as 10^4 to 10^5.

FIGURE 3. REYNOLDS NUMBER VS LENGTH

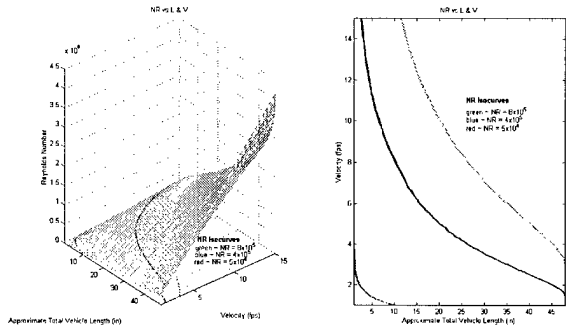

We then created an iterative design space examining 'body-of-rotation' vehicle designs from 1" to 5" diameter and from 1.6" to 49" length. Prismatic Coefficient for these vehicles vary from that of a pure prismoid solid rotated about the long axis (~Albacore hull, Cp ~0.667) to a right circular cylindrical shape (Cp=1). Using velocities from 1 to 15 fps, we calculated the Reynolds Number for each configuration.

Investigators in the body of hydrodynamic science for small vehicles (Goldstein[2], Taylor[3], Lighthill[4], others) address limitations in how N_R and C_D based calculations are not reliable to accurately evaluate all of the "physics of the small". They more fully develop hydrodynamics as analogue relationships, which apply and are integrated across body lengths and shapes. Numerous potential field and other based models for calculating hydrodynamic thrust and drag for small regimes have been developed.

Non-linear finite element (FEA) methods have been established using those analyses and provide the only reliable methods to calculate real drag, especially in regimes of small N_R. In general terms, these methods calculate pressure differentials across elemental size components and include viscous affects to resolve elemental drag and then integrate across the body structure to resolve total drag. These analytical methods resolve many of the non-trivial uncertainties and errors associated with CD based hydrodynamic force and power calculations.

However, in pursuit of our goal and as a first order approximation, we used Jackson's[5] relationships for vehicle drag coefficients, C_f and C_r:

$$C_f = \frac{0.075}{[\log_{10} N_R - 2]^2} \qquad C_r = C_f[1.5(D/L)^{3/2} + 7(D/L)^3 + 0.002(C_P - .6)]$$

$$C_D = C_r + C_f$$

$$F = \tfrac{1}{2}\rho \cdot C_D \cdot A \cdot V^2$$

and extend our analysis to calculate

- estimates of total drag force (shown in figure 4) and
- identify areas where the math is not well formed.

FIGURE 4. DRAG FORCE OF DATA SET

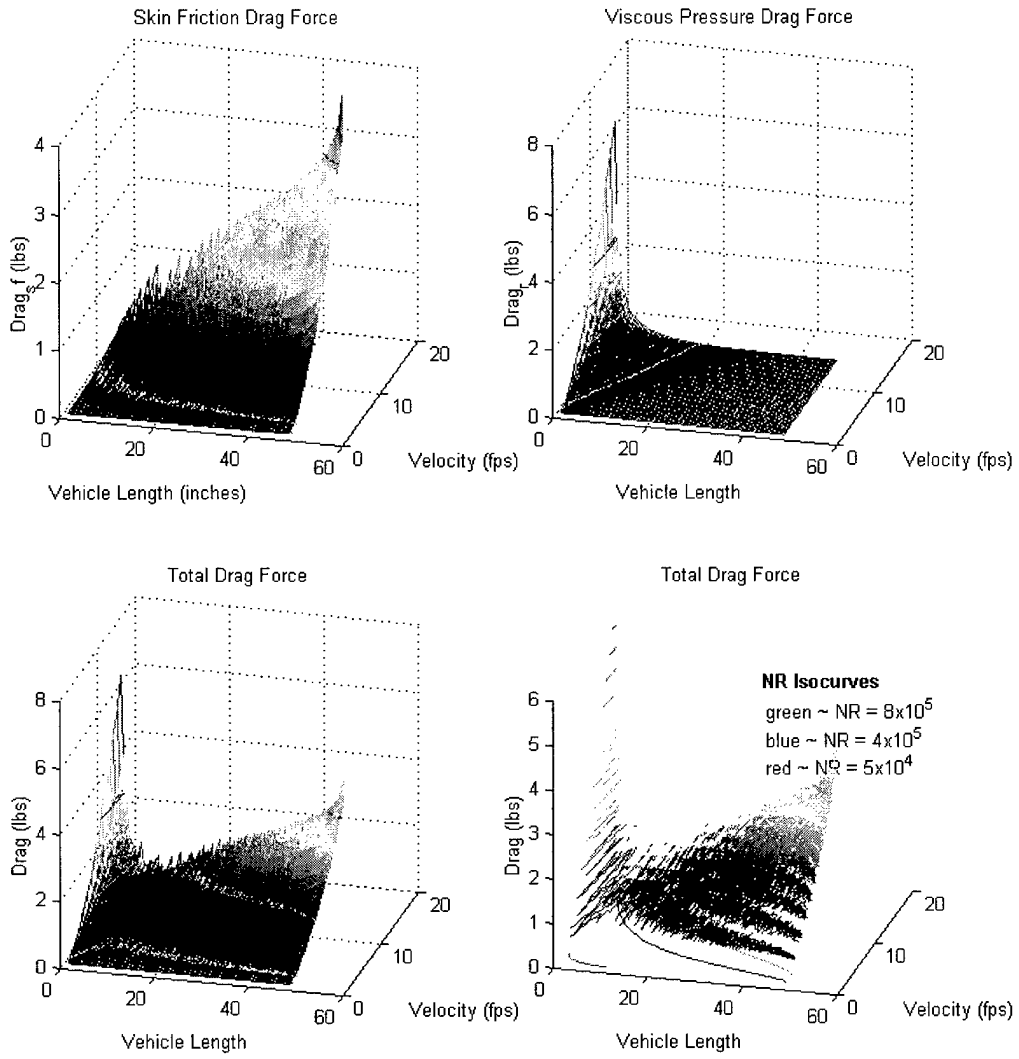

This analysis identifies either:

- a failure in the equations to characterize the hydrodynamics of the small, or
- a substantial, perhaps profound observation.

Specifically, note the intersection of the two drag forces, occurring at a minimum saddle between 10 and 20 inches in length and which becomes more dramatic with increasing velocity. This size is "interesting" due to:

- occurring in the regime of $N_R \sim 10^5$ (near laminar-turbulent transition regime)
- the 10"-20" size similarity to some faster, undulatory, carangiform fish such as trout or salmon.

Sustained swimming speeds of trout (and most fish) occur at up to 2 body lengths per second. For lengths between 10-20", this equates to 2-5 fps (1-2 kts) in the chart. Burst speeds occur at 4~8 body lengths per second (or 4-10 fps, 2-6 kts in the chart)[6]. Assuming trout use burst speed for

attack or escape events necessary for survival, "Natural's" design for survival is congruous with the minimum drag relationship shown.

Poignant to our pursuit, the skin friction drag observably increases as length (or length to diameter) increases. This is due to the larger wetted surface area in increased length platforms (holding diameter to similar values).

FIGURE 5. MICROAUV VOLUME AND ENERGY

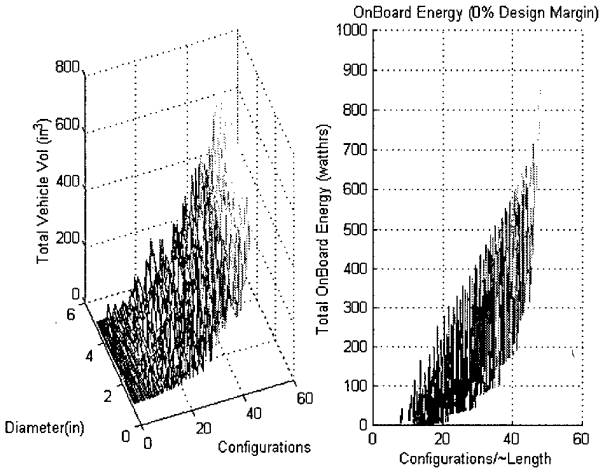

Later in this effort, we develop a volume and mass budget and resolve the volume available for energy storage. The results are shown in figure 5. Acknowledging our own packaging inefficiencies compared to nature, and limitations based on our sizing of various COTS components, the right half plot shows that no onboard energy storage exists for vehicle lengths below ~10". The upper bound of the colored area in this plot indicates the maximum energy storage per length, which is understandably associated with a larger diameter body (given approximately equal lengths).

Connecting:

- the larger drag for larger surface area, as implied in the curves of Figure 4 with
- the maximum energy for larger diameter platform story of Figure 5, and
- the minimum of the lower plot(s) of Figure 4,

says that the final optimum vehicle configuration is likely constrained on one end by the tactically defined maximum diameter of the vehicle and with a low L/D (4 to 6) and on the other side with a vehicle larger than 10" and also with a Low L/D.

Areas where the Math is not well formed.

The total drag minimum at ~10" in the bottom plot(s) of Figure 4 *(caused by C_f growing large rapidly as length goes toward zero)* says there ***"may be no value"*** in improving technology to make a vehicle smaller than 10". Alternatively, this result ***"may be"*** a limitation in our analytical method.

Discussions with Sandberg[7] identify that we can further continue this investigation, through a more refined evaluation of these various design configurations within Naval Research Laboratory's (NRL) Finite Element Fluid Flow (FEFLO) analytical routines. The FEFLO facility applies pressure difference across body elements and considers fluid viscosity to directly calculate forces at each element to define the force field about the vehicle. FEFLO can then sum the forces over the entire vehicle surface to get total drag (vice applying empirical drag coefficients to a total area per

Jackson). Pursuing the NRL FEFLO analysis would add validation to our results (or insight into our "gross method" limitations) and accurately define the trade space of drag force as parametric variation in design attributes such as diameter, length, shape (prismoid and volume coefficients) at a vehicle mass of 1 – 5 kg.

Additionally, as the vehicle size is increased, one might reasonably presume that the volume for stored energy becomes an increasingly larger percentage of the overall vehicle. We believe this is generally a good presumption, notwithstanding other issues associated with providing for sufficient additional structure to keep the large mass together in large vehicles (ie the ant vs the elephant power to mass ratio and structural disparities, which are well known).

Regardless, the minimum shown above hints that a vehicle of size comparable to trout, will reap some additional benefit in drag reduction and hence increased specific endurance over larger sized vehicles.

MEMS:

We pursue minimal, yet sufficient onboard hardware to enable MicroAUV to:

- Continually advance in environments of opportunity
- Communicate with (sense) the environment, sufficient to:
  - discern trajectory (obstacle avoidance)
  - measure some physical field parameter
- Carry and support a payload of some purpose
- Communicate with other "near by" units, and/or a supervisory node.

The MicroAUV Performance Specification[8] (§ 3.2.8) does not require an ability to communicate with other near by units. However, Future Navy Capabilities (FNC) clearly define needs for multiple and collaborative underwater vehicles. We have kept a keen "eye" towards opportunities that leverage in this direction in our design and discussed relative ranging and collaboration with multiple vehicles in our initial report[1] (see section on Operating Scenarios). We have matured the MicroAUV system design, shown in figure 6.

FIGURE 6. MICROAUV SYSTEM SCHEMATIC

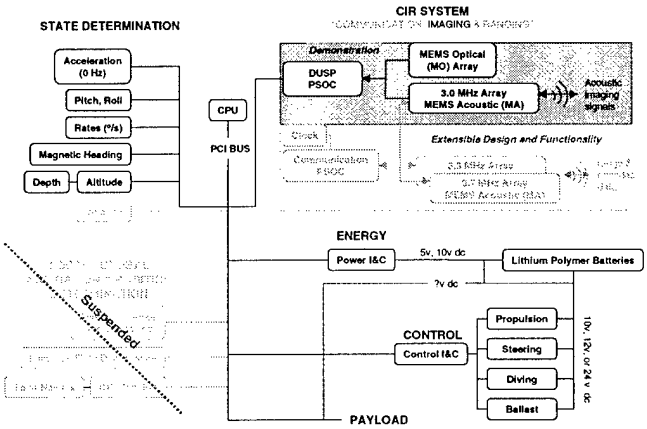

State Sensors

MEMS implementations of state sensors above are resolved through COTS products and are discussed in the System Design section of this report. In the system design report, we further discuss the integration of these sensors embedded into the hull structure.

The Communication & Ranging Subsystem

The Communication & Ranging (CR) Subsystem is our "conceptualized extension" of the Imaging System to gain more function from the Imaging System hardware, by augmenting with two additional MEMS transducers, tuned to two separate frequencies and thus to transmit and receive data embedded within an FSK architecture .

We are also examining whether or not the additional transducers can be developed as arrays and augment "imaging" efforts as well. Figure 7 provides a schematic of the Communication and Ranging subsystem of the CIR System.

FIGURE 7. COMMUNICATION & RANGING SUBSYSTEM

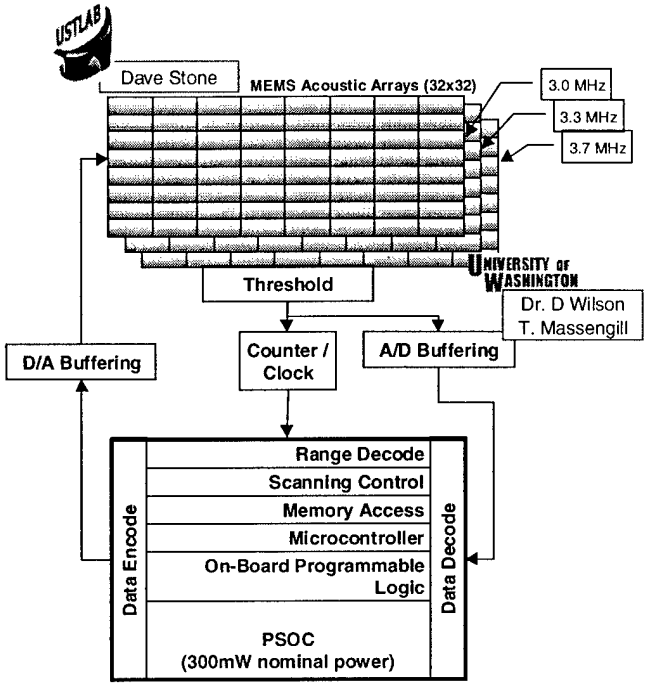

Conceptually, the CR subsystem is clock-synchronized with other peer or Mother AUV (MoAUV) unit(s) that would communicate and range with MicroAUV. First signal receipt triggers the clock driven counter and sets the range. The sequencing of the frequency pulses then serially received (transmitted) in the same signal sets the data word. Data words identify the MicroAUV unit number, its resolved relative location estimate, sensed local field data, (payload data) and other data from other units. The MicroAUV Team has submitted an STTR proposal to an ONR topic on Autonomous Distributed Systems[9] to more fully develop this technology and to work synergistically with our MicroAUV program effort.

In our initial report we communicated that to keep power budget down, the transmit range of the MicroAUV acoustic signal would be 20 to 30 meters. Ranging, timing synchronization and onboard processing (and hence, relative navigation between units) will be sufficient to enable multiple units to collaboratively survey to certain accuracy (~5 meters[10]) and/or advance to certain goals.

Further, multiple "peer" MicroAUV units will collaborate such that on appropriate command, all units will transmit certain signals simultaneously. Our current analysis estimates that a swarm of 99 MicroAUV units, spread out over a 1500-meter line array, could each transmit and their collective signal could be received in excess of 2 km away.

Novel "No Power" Sensors

Of note, we have suspended the intention to develop no-power navigation sensors. Analyses were started and a report is provided as attachment 3. Two observations are germane:

1. The attached report addresses interesting and fantastic notional conceptualizations for implementation of two biology-inspired systems to achieve highly accurate navigation:
   - Utilization of incoming sunlight angle (shallow water)
   - Sensor fabric to sense "ultra small" perturbations in the magnetic field

   However, the concepts require considerable development in science and chemistry to be viable. We expect ten years plus to develop (far outside the scope of MicroAUV).

2. The analyses in that area has been unable to format the report with referenceable claims Hence, we cannot verify the integrity of the data and the claims made.

We have terminated the contractor's efforts within MicroAUV program and encouraged his pursuit of these concepts to other sources (DARPA MEMS program, Nanotechnology development thrusts, etc.).

The phrase "No-Power Sensors" generates considerable "buzz" in some literature and other DOD programs today. To date, we have only resolved that many concepts are emerging, and that real products seem to be "down the road".

ISSUES

The technical issues in our plan include:

Issue	Approach to Resolve
1. **MA Sensitivity:** UW MEMS team members consider the MEMS acoustic (MA) image device buildable. CMU (G. Fedder) concurs. However, the receiver sensitivity may be marginal and because of edge effects in the MEMS sensor, the tuned frequency may be off our nominal design point.	1. Build prototype sensors in ASIMPS production run & test 2. Continually review design 3. Possibly back fill sensor gap with dielectric oil. 4. Increase in-water signal strength **BACKUP PLAN**: Build MicroAUV without imaging.
2. **Vehicle Control:** To avoid the mass & power penalty, control surfaces are not planned. Hence vehicle flight control must be accomplished by other means.	1. We have been identifying methods to vary propeller pitch on the fly and use that capability to control pitch and heading. At 4 kts forward speed, IPMCs, PVDFs and Shape Memory Actuators, integrated with Thermal Electric temp control (SMATE) all appear as viable methods to achieve a variable pitch and/or variable camber propeller. We are pursuing discussions with ORNL and ITN towards an upcoming opportunity to more fully develop this capability. 2. Implement control surfaces with IPMC, PVDF or SMATE material **BACKUP PLAN** Go back to more conventional control surface design
3. **MA Pressure Affects:** The MA device currently uses an air gap behind a spring of the same width as the wavelength of the incoming signal at 3.75 MHz. The air gap may allow pressure to degrade performance	1. Examine methods to "pre-load" sensor gap with a back-filled dielectric oil, gas bubble, or ... other means. Note that methods to back fill with something other than water may affect the dynamics of the sensor. 2. Examine dielectric coatings that are *pc* equivalent to water. 3. Conduct testing with prototype units

INTRODUCTION

As stated in the executive summary, the MicroAUV program pursues a novel underwater vehicle design to achieve an order of magnitude increase in specific endurance over currently fielded systems, by incorporating COTS MEMS electronics and additional innovation in integrating MEMS sensors within hull structure.

Currently fielded systems are captured in the body of such vehicles as REMUS, CETUS, and others. The specific endurance of these platforms is represented in Figure 1 above. Note that VMS (Variable Mooring System) is a glider vehicle, vice using active propulsion drive to accomplish speed of advance. Micro AUV goals will be to achieve the VMS endurance or better on active propulsion drive technology. Nominally, our goal is 20 Nautical Miles per pound mass displacement.

Current vehicle data were extracted from a FY2000 study on AUV developments[11]. Also, previous analysis of the Large Scale Vehicle (LSV) propulsion power at 6 kts, rendered a specific endurance of 0.008 nm/lbm and is summarized below.

Displacement		142 tons (282000 lbm)
Energy per cell	*(750 Ah * 2 vdc)*	1.5 KwH
Total Energy	*(~500 cellls * 1500 wthrs)*	750.0 KwH
Power (SOA ~ 6 kts)	*(~9 amps @ 230 vdc)*	2.0 Kw
Endurance		375.0 Hrs
Range		2250 nm
	Specific Endurance	**0.008 nm/lbm**

Note that ballast mass and other trials electronics could be replaced with additional batteries in order to increase range to as much as ~4000 nm (~0.013 nm/lbm)

METHODS & PROCEDURES

We have pursued the development of MicroAUV's design on several fronts.

COTS MEMS — After an initial review of MEMS technologies and survey of COTS MEMS devices available, we identified those COTS MEMS components we could locate in industry and identified that an adequately sufficient imaging system at low enough power for our application was not available. These components are discussed in the System Design section titled "COTS MEMS".

Other Components — Additionally, to ensure our power and endurance analyses were developed with integrity, we located all other components needed for MicroAUV. These components are discussed in the System Design section titled "Other Components".

Hydro Analyses — We continue to identify and locate the existence or lack of "sweet spots" in vehicle design drag, power and energy / endurance calculations.

We have collated the power of all components, as discussed in our System Design Section, into an integrated vehicle design and applied operational profiles to define power budgets. We then integrate our hydrodynamic analysis to calculate vehicle endurance as discussed in the RESULTS section.

ASSUMPTIONS & APPROXIMATIONS

We pursue minimal, yet sufficient onboard hardware to enable MicroAUV to:

- Continually advance in environments of opportunity
- Communicate with (sense) the environment, sufficient to:
  - discern trajectory (obstacle avoidance)
  - measure some physical field parameter
- Carry and support a payload of some purpose
- Communicate with other "near by" units, and/or a supervisory node.

Our 'design-guiding' approximations and/or assumptions include:

- the vehicle is expendable
- the vehicle does not cost much, when made in large production runs
- minimal but sufficient capability
- elegant and robust in simplicity not complexity

It is our vision that few enough capabilities on MicroAUV to enable mobility and networking can be substantially multiplied in many MicroAUVs operating together to achieve an overall high tactical effectiveness.

OPERATING SCENARIOS

We developed and submitted a MicroAUV Performance Specification[8], which defines expectations of MicroAUV including:

Specific Endurance	20 nm/lb.	
Payload Power	0.3 watts average	5 watts peak power
Speed	min > 3 kts	max $\geq$ 6 kts

Operating Profiles	Description
Transit or **FSL-SS**	Fly Straight & Level @ Steady State Speed (FSL-SS), Assume maximum propulsive efficiency.
High Maneuvering	Propel at ~8 kts, but advance ~5 kts, assume minimum propulsive efficiency
50/50	Consists of 50% mix of the above two modes

To examine High Maneuvering scenarios, we previously calculated a net higher power associated with a net higher speed of ~8 kts velocity in order to achieve a net forward speed of advance (SOA) of ~ 5kts.

However, MicroAUV will most likely be designed for an optimum but constant through water speed at 5~6 kts. "High Maneuvering" will likely be accomplished at this constant speed through water with a net reduction in Speed of Advance (SOA) over ground due to the maneuvers.

Hence, in endurance calculations, we now estimate "high maneuvering" at the same speed (power out) and use an SOA of 70% lower (~3.5 kts) for a net reduction in range.

OPERATING SCENARIOS AND IMPACT ON SENSORS:

At ~5 kts (8.5 fps) forward speed, the imaging envelope need only be up to 40 ft ahead. As either density of obstacles in the field or speed of advance reduces, imaging can operate at less sampling frequency and/or range of vision.

Our optical and acoustic imaging designs and power estimates are being developed to image up to 30 ft and beyond. Moreover, we are adjusting our power estimates of these sensors to operate at a higher sampling frequency at high maneuvering and at a lower sample frequency at FSL-SS.

HYDRODYNAMICS

In our hydrodynamic study, we are attempting to identify and locate any sweet spots in vehicle design, given our design constraints. Our analysis trade space would be nicely formed if it allowed us to resolve the hydrodynamics and the onboard power and energy budgets into a relationship such as shown in Figure 8 or otherwise similar.

FIGURE 8. MICROAUV NOTIONAL TRADE SPACE

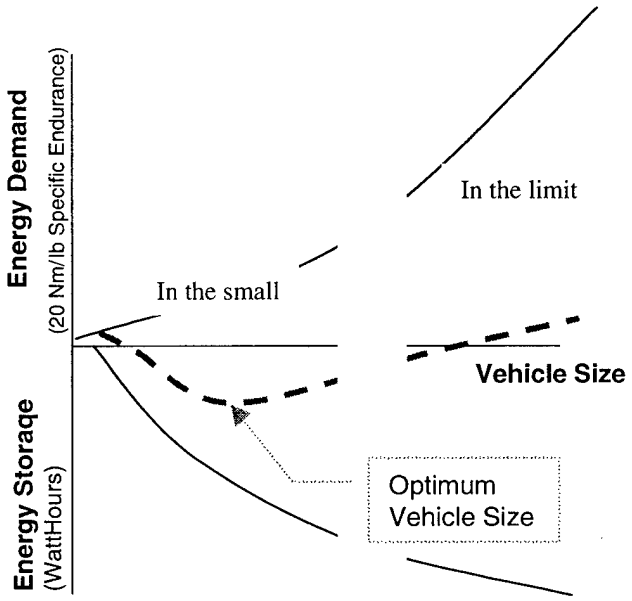

In Figure 8, as vehicle size (displacement) increases, energy storage increases, approaching a linear slope (shown increasing downward in the sketch). Similarly, if energy demand per unit size increases with size, then depending on the rates of increase, an optimum vehicle size might emerge from the design. Using conventional (non-nuclear) energy sources, the relationship is anticipated to become unachievable in the limit (ie for the storeable energy, the vehicle cannot achieve 20 Nm/lb).

The difficulty in this trade space goal is the various parametrics relative to size. Specifically:

> "two similarly sized vehicles can be grossly different in diameter, length, and hull taper and further that these differences in configuration can constrain the lay down of some components, affecting packing efficiency in 'hard-to-model' (and analyze) ways."

Additionally, transitions occur at certain size limits, such that mass allocated for certain areas as hull, structure, drive train, fault tolerant design modifications change substantially relative to total vehicle mass.

For tactical and cost reasons which drive, but are not otherwise integral to these design analyses, the loss of MicroAUV is envisioned as an expendable event wherein the loss of a larger vehicle is envisioned to be a costly and perhaps unacceptable event.

Outlay for infrastructure follows different rules across these design goal regimes. IE, redundant systems may be forgone in MicroAUV and mandated in more costly systems, thus increasing mass, power, and adding to endurance reduction for MicroAUV. Hence, in order to develop a trade space such as Figure 8, one must make some approximations, which include:

12% of vehicle for hull (plus the 134 g for integrated electronics),
13% of vehicle for motor and drive train,
5% for propeller
20% of vehicle for payload.

The remaining vehicle is allocable to energy and in considering three (3) separate budget values for design margins of 0%, 10%, and 20% in mass (volume displacement). These estimates are reasonable for 4 lbm and larger vehicles. Our system design effort has identified sufficient COTS motor and battery systems that support the above relationship and equivalent masses in our custom design of hull, propeller, electronics and other COTS electronics.

The actual sizes of onboard electronics sensors are tabulated, based on sensor components commercially available and custom designs within our team. A table at the end of this section presents the current sensor suite. Net overall mass is estimated at 134 grams, including ~ 100% margin for uncertainty.

In each of these design considerations, care must be taken to ensure error does not dominate in the final conclusion. Initially disregarding the above budgets, we first assembled (modeled in Matlab™) 1188 separate vehicle configurations by defining a three-section hull of nominal diameter from 1" to 5" in ½ inch increments (9 variations). The forward and after hull sections are ½ of an ellipsoid volume, formed by rotating an ellipse around the longer axis, which is coincident with the hull axis. The formula for volume and surface area of these bodies of rotation is established[12]. The center section is a right circular cylinder, for which volume and surface area are easily calculable. For each body diameter, each hull section is varied from a min to a max in 11 increments. The length variations were "built" in the following manner:

1. summing each i^{th} length of forward and after hull section to create 11 length sums
2. adding each of these 11 forward and aft hull sums to each of the 11 hull midsection lengths for a total of 121 configurations
3. including the 11 hull midsections lengths (without elliptical ends) for a total of 132 length configurations for each of 9 diameters {9 x 132 = 1188 configurations}

RESULTS

HYDRODYNAMICS

As configurations were defined and analyses completed, data were sorted by length. Actual length is plotted against configuration number in figure 9. Henceforth, other parameters are compared to configuration number or length, interchangeably.

FIGURE 9. LENGTH TO CONFIGURATION NUMBER

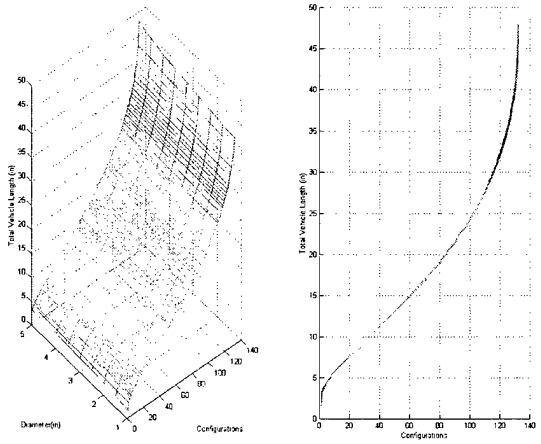

For each configuration, Length (L) to Diameter (D) ratio is calculated to show variation in bluntness over the configuration set of data examined. L/D and D/L are shown in figure 10.

FIGURE 10. LENGTH TO DIAMETER VS CONFIGURATION

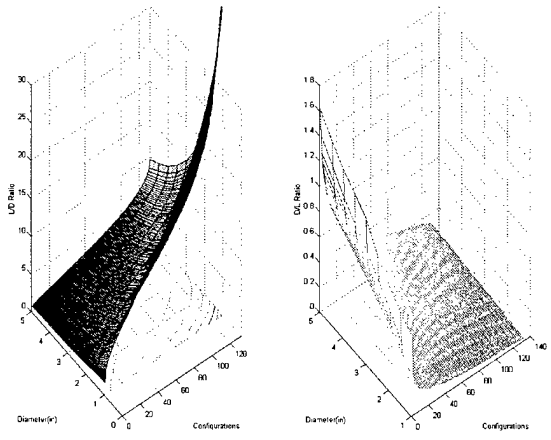

Further, the prismatic coefficient is readily definable in the manner in which we "assembled" our body configurations. Figure 11 shows that each configuration included a middle section whose prismatic coefficient is 1 and a front and aft ellipsoid body of rotation whose Prismatic coefficient is 0.667.

FIGURE 11. BODY SECTIONS

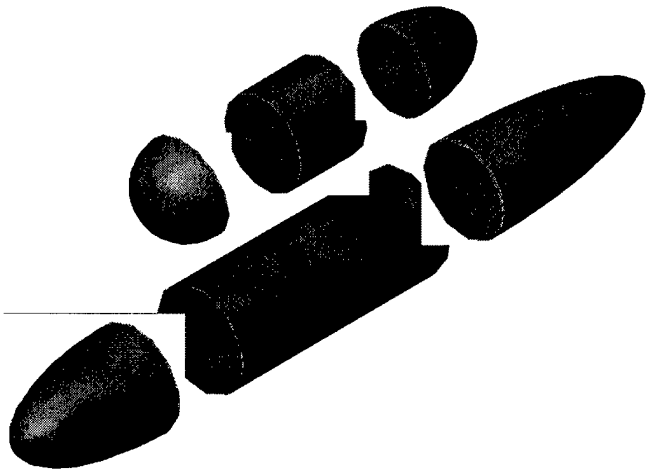

In assembling each configuration and then sorting the data according to increasing length reveals Prismatic Coefficients oscillating between 0.667 and 1 per figure 12.

FIGURE 12. PRISMATIC COEFFICIENT

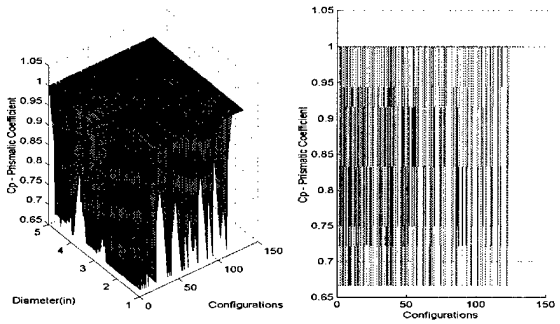

Again, we use Jackson's equations for Drag to examine the hydrodynamics of these bodies across all lengths and diameters, from blunt to elongated tapers (L/D's from ~2 to ~30) and from 1 to 15 fps through water speed.

$$C_f = \frac{0.075}{[\log_{10} N_R - 2]^2} \qquad C_r = C_f[1.5(D/L)^{3/2} + 7(D/L)^3 + 0.002(C_P - .6)]$$

$$C_D = C_r + C_f$$

$$F = \tfrac{1}{2}\rho \cdot C_D \cdot A \cdot V^2$$

Length remains a contributor in calculating N_R and subsequently C_f. Figure 13 shows C_f vary as a parametric of vehicle configuration (length to 48 inches) and velocity, which we varied in our analyses from 1 fps to 15 fps in 1-fps increments.

FIGURE 13. COEFFICIENT OF SKIN FRICTION DRAG

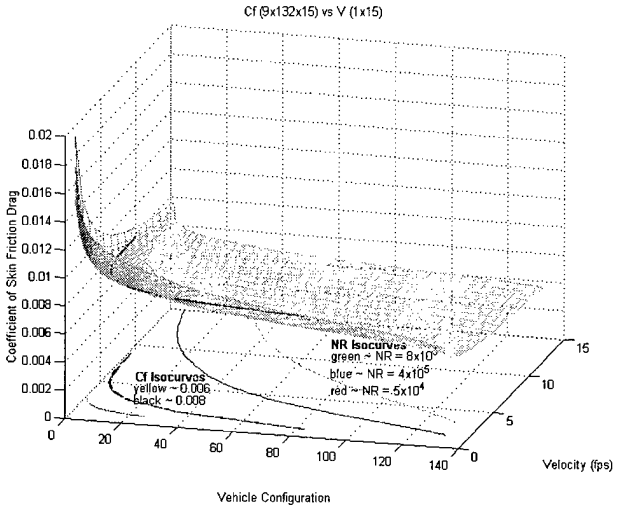

Note that the figure is actually 9 plots for 9 different diameters. However, diameter in and of itself does not grossly affect the data and the 9 separate plots for the 9 diameters emerge as a near single surface. This is consistent with the manner in which we developed the configurations as linear multiples of diameter, forcing the L/D variations to be nearly identical for each set of diameter configurations.

Figure 14 shows C_r as a function of length and velocity, derived from its dependence on C_f, L/D and Prismatic Coefficient.

FIGURE 14. COEFFICIENT OF PRESSURE DRAG

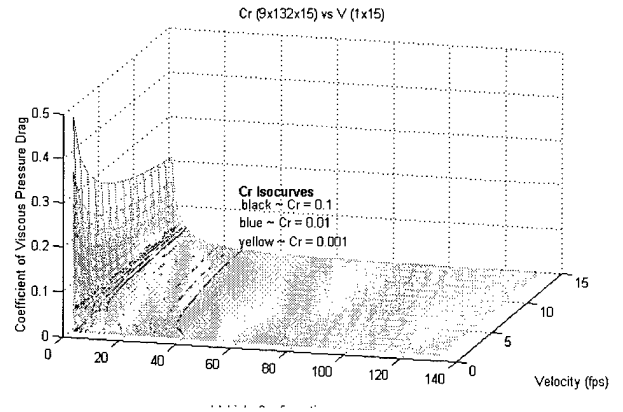

Note that both drag coefficients approach asymptotic increases towards positive values as configuration (length) tends toward very small numbers and that C_r is several magnitudes larger than C_f in areas of lower length, but both approach similar orders of magnitude at lengths > 20".

To calculate total drag,

- wetted surface area is calculated and used with C_f to get skin friction drag
- projected area is calculated and used with C_r to get pressure drag.

Figure 15 displays surface area is shown below and varies $\pm$ 50 in^2 for each length, as consequence of the varying diameter within each length.

FIGURE 15. WETTED SURFACE AREAS

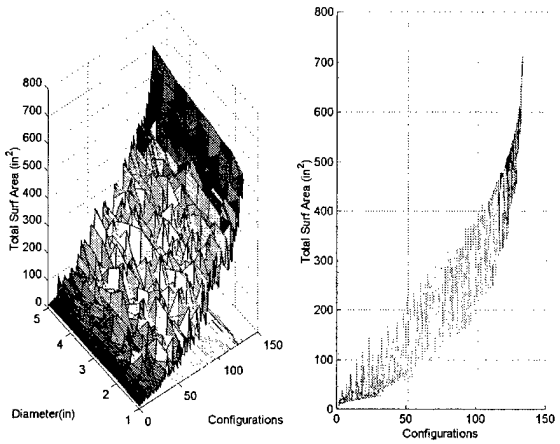

Again, 132 configurations represent lengths varying from ~2" to 48" and each length has several configurations of varying diameter.

Thus Drag is calculated, as shown in the Executive Summary and repeated in Figures 16-19 below. Note that these figures each represent 9 surface plots, replicated, one on top of the other for each of 9 diameters considered.

FIGURE 16. SKIN DRAG FORCE

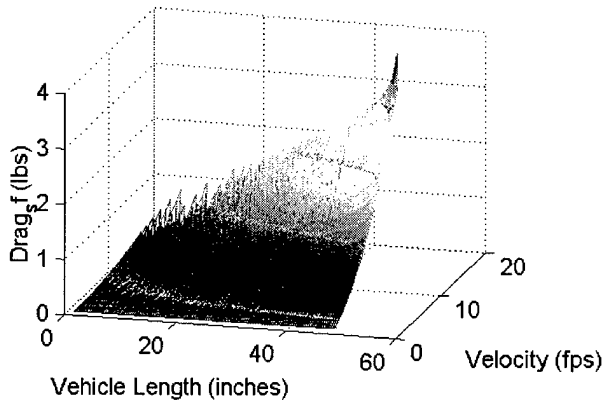

Note that surface area is increasing considerably with length and so the combination of length, velocity, and drag coefficient combine to make skin drag reach substantial values.

FIGURE 17. PRESSURE DRAG FORCE

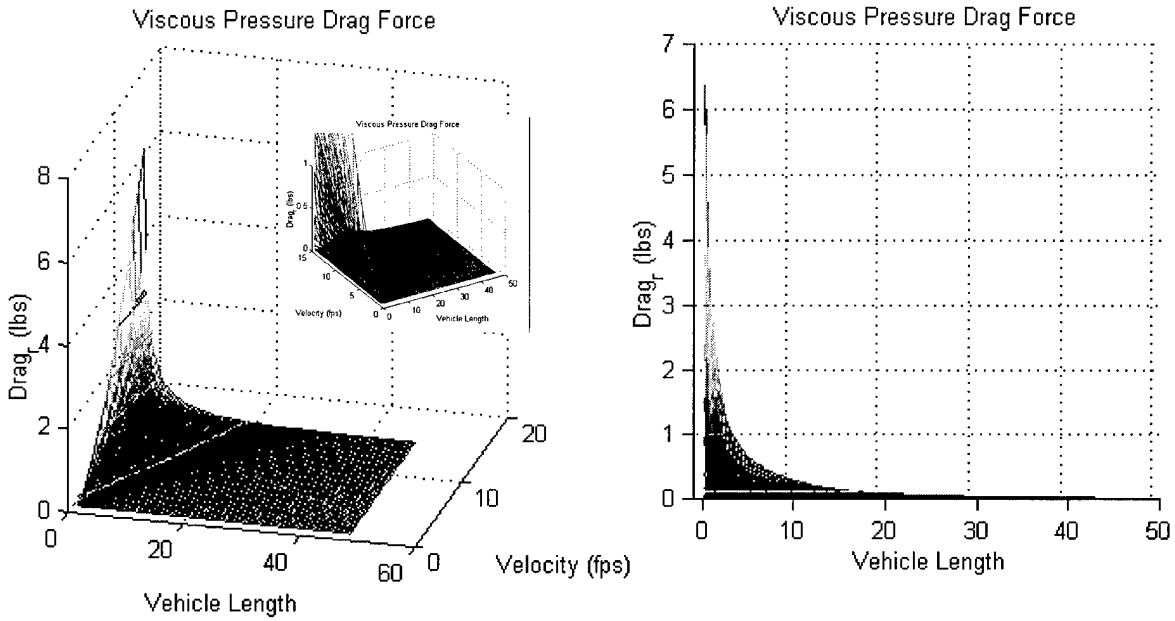

The velocity range does not go high enough yet to drive form drag high enough to be observable for the longer lengths shown. However, the D/L ratio dominates in the lower lengths, driving drag force to observable values above 2 fps. Note again, that the figure represents 9 surface plots of Drag for each of 9 diameters from 0.5" to 5.0" in ½" increments. Because of the sorting of the data on length and the smallness of the results, the influence of the diameter is not discernible.

Hence, combining these two forces renders total drag and defines a minimum saddle in the regime of 10-20 inches in length, regardless of diameter, although the lower diameters do not substantially contribute to the rise in drag at lower lengths as these surface plots are for the larger diameter vehicles.

FIGURE 18. TOTAL DRAG

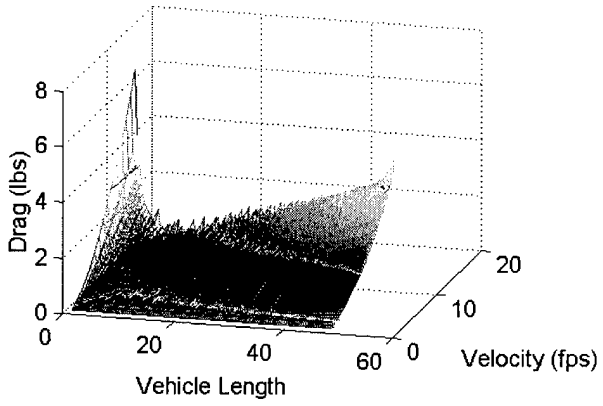

FIGURE 19. TOTAL DRAG (ISO-DRAG CONTOURS)

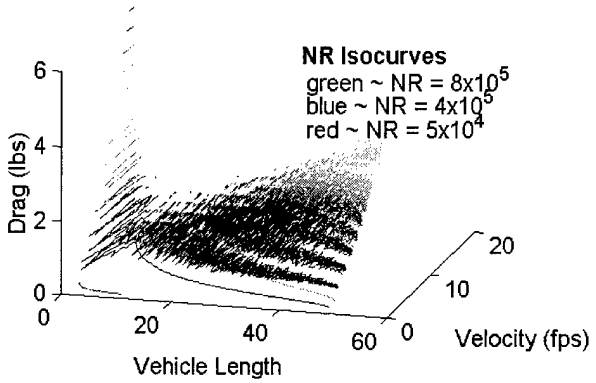

Observation

In the regime of 8-10 fps (5+ kts), the drag can be minimized to ~2 lbs drag, by using a vehicle in the 10 to 20 inch size, where N_R is between 1 x 10^5 and 4 x 10^5. Moreover, diameter does not substantially impact the results and a large diameter body may be more advantageous when it comes to energy packaging and endurance calculations.

Fundamental problem with the observations is:

The lack of diameter influence in the data is counterintuitive and the arbitrariness of the minima is not intuitive, except inasmuch as it is interestingly close to the size of small fish whose burst speeds are on the order of 5~6 kts.

The author is not certain the above data represent the physics with sufficient accuracy to be relied upon.

To validate these data and hopefully to select "the optimum" design(s) of a Microminiature AUV, we plan work as discussed in the recommendation section, including:

1. Continue and extend these analyses to intersect volume (onboard mass and energy budget) to operating profile and power to get endurance and range for all configurations.
2. Develop a couple point model designs and conduct hydro demonstration (see RECOMMENDATIONS)
3. Work with NRL FEFLO either in Option 1 of this effort or in our year 2 effort, to evaluate the drag using their methods and compare those results to the results developed above. Resolve disparities and feed corrected drag data into 1 above.
4. Develop conclusions from 1. and 2. above, hopefully defining one or more regimes of optimum (and viable) MicroAUV design size.

MEMS INSTRUMENTATION POWER BUDGET

The MicroAUV nominal instrumentation power budget, as currently defined, is inventoried in figure 20. This inventory represents a survey of over 100 candidate Micro Miniature and MEMS based components for the selected few shown.

FIGURE 20. MEMS SENSORS POWER BUDGET TABLE

Part Name	Model Number	Watts	SS Op Tempo	Hi-Mnvr Op Tempo	No. Units	Effective Total Power	Effective Total Power
STATE DETERMINATION							
Dual Axis Accelerometers	ADXL202	0.0180	1.00	**1.00**	2	**0.04**	**0.04**
+150 °/s Single Chip Rate Gyro	ADXRS150	0.0250	1.00	**1.00**	2	**0.05**	**0.05**
Tilt compensated Compass	EZ-Compass	0.0100	1.00	**1.00**	2	**0.02**	**0.02**
Velocity Sensor		1.0000	0.10	**0.10**	2	**0.20**	**0.20**
Depth (Sub Miniature Sil-Chip Pres	PB-CO-1-50/	0.0208	1.00	**1.00**	2	**0.04**	**0.04**
CONTROL I&C							
CPU	PIC16F87X	0.0018	0.50	**1.00**	22	**0.0198**	**0.0396**
CPU	PIC16F87X	3.00E-06	0.50	**1.00**	22	**0.0000**	**0.0001**
Power Control Sensors		0.0100	1.00	**1.00**	2	**0.02**	**0.02**
COMMUNICATION, IMAGING, & RANGING (CIR) System							
Clock?(GPS clock?)	tbd	0.0100	1.00	**1.00**	1	**0.01**	**0.01**
Acoustic Comms		0.1500	0.10	**0.10**	1	**0.02**	**0.02**
Comms DSP		0.0018	1.00	**1.00**	4	**0.01**	**0.01**
CMOS MEMS Acoustic (MA) Image Sensor		0.1500	0.10	**0.10**	1	**0.15**	**0.15**
CMOS MEMS Optical (MO) Image	PB0100	0.0990	0.50	**1.00**	1	**0.05**	**0.10**
CIR (MAMO DUSP) DSP *(Add'l 100 mW budgeted in*		0.1000	0.50	**1.00**	2	**0.10**	**0.20**
					SubTotal	**0.72**	**0.89**
				Design Margin (100%)		**0.72**	**0.89**
Payload (20%)			1.00	1.00	1	**0.30**	**0.30**
				Total Instrumentation		**1.74**	**2.08**
						watts	**watts**

Size of each COTS component, as generally available in industry, is around the size of a CERPAK dip chip. However, this is actually larger than necessary, as the actual sensor of these devices is much smaller, but the CERPAK provides necessary packaging to connect each device IO to interfacing PCBs.

The University of Washington has identified methods to reduce CPU throughput power and DSP power by developing custom designs. Also, UW (Massengill) has identified a 16-bit MicroChip controller, which consumes extremely low power. We are uncertain of the computational throughput demand for our MicroAUV application and are anticipating a distributed processing capability, using 22 MicroChip controllers to accommodate all computational needs. We have also allocated an additional 100 mW for the CIR MAMO DUSP. Moreover, we have increased instrumentation power design margin to 100%. Power is summarized below and is approximately 75% of our initial estimate (which was 2.14 and 3.41 watts).

Power of the acoustic pulse in our initial report to achieve acoustic illumination is reviewed and described in the System Description section of this report.

MEMS Mass Budget

Figure 21 itemizes mass of Instrumentation components, which is only slightly modified from our initial estimate and still includes 100% design margin.

FIGURE 21. MEMS SENSORS MASS BUDGET TABLE

Part Name	Model Number	No. Units	Total Size (cm^3)	Total Mass
STATE DETERMINATION				
Dual Axis Accelerometers	ADXL202	2	8.00	4.00
+150 °/s Single Chip Rate Gyro	ADXRS150	2	8.00	4.00
Tilt compensated Compass	EZ-Compass	2	4.00	4.00
Velocity Sensor		2	2.00	2.00
Depth (Sub Miniature Sil-Chip Pres	PB-CO-1-50/	2	0.12	2.00
CONTROL I&C				
CPU	PIC16F87X	22	22.00	33.00
CPU	PIC16F87X	22	0.00	0.00
Power Control Sensors		2	0.12	2.00
COMMUNICATION, IMAGING, & RANGING (CIR) System				
Clock?(GPS clock?)	tbd	1	2.00	1.60
Acoustic Comms		1	2.00	1.60
Comms DSP		4	8.00	6.40
Acoustic Image Sensor		1	2.00	1.60
CMOS Image Sensor	PB0100	1	2.00	1.60
CIR (MAMO DUSP) DSP *(Add'l 100 mW budgeted in*		2	4.00	3.20
		SubTotal	**64.24**	**67.00**
		Design Margin (100%)	**64.24**	**67.00**
Payload (20%)		1	**25.70**	**26.80**
		Total Instrumentation	**128.48** cm^3	**134.00** g

Gross Mass Budget

These mass data are incorporated into the overall vehicle budget, which has been modified per figure 22. An example displacement of 8 lbm is shown, but the table applies for all examined configurations, wherein percentages of displacement are allocated for each of 4 areas to define the mass of those components.

FIGURE 22. GROSS MASS BUDGET OF MICROAUV

		Unassigned Material Design Margins 0%	10%	20%
Instrumentation		134	134	134
Motor & Drive Train	13.0%	481	481	481
Hull (including CPCB)	12.0%	444	444	444
Propeller	5.0%	185	185	185
Payload	**20.0%**	**740**	**740**	**740**
Design Margin		**0**	**370**	**740**
Battery		1716	1346	976
Total (8 lbs)		**3700**	**3700**	**3700**

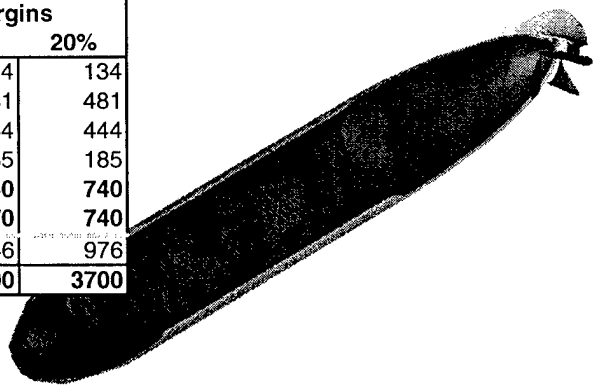

Hence, as the vehicle mass varies, battery mass and stored energy will vary. These data are incorporated into the MATLAB trade space analysis to resolve endurance as consequence of hull size, configuration, stored energy and gross power demand over each operating profile.

GROSS POWER BUDGET

The gross power budget for the vehicle has been simplified to the format shown in figure 23, wherein data for each configuration needs to be included. Instrumentation Power (IP) is carried over from Figure 20. Hydrodynamic Drag Power would be as derived in the MATLAB™ calculations and the Drive Train Efficiency applied to that theoretical number to Effective Propulsion Power, which is then summed to the IP to get Total Power in watts.

FIGURE 23. GROSS POWER BUDGET FOR MICROAUV

		Operating Profiles FSL-SS	Hi-Mnvrs	50/50
Instrumentation Power {IP}		1.74	2.08	1.91
Payload	*(embedded in Instr Power)*	-	-	-
Hydro Drag Power {HDP}	*f {hull, speed}* **	**	**	**
Drive Train Efficiency {DTE}	*f {prop design, speed, sterng & diving} ~ estimates*	60.0%	52.5%	56.3%
** *this is captured in the MatLab Drag Analyses, shown here from spreadsheet data*				
	Total Power (watts) *{IP + HDP/DTE}*	**1.74**	**2.08** *=+ HDP/DTE*	**1.91**
	Speed Through Water (kts)	5	5	5
	Speed of Advance (kts)	5	3.5	4.25

ENDURANCE ANALYSIS

MicroAUV Hydro Drag Power (HDP) has been calculated in MATLAB™ for each of the three operating profiles and for each of the 132 hull configurations, across the velocity range of 1~15 fps. The energy per each hull configuration is also calculated, each with 3 mass budget "design margins".

However, two single-point analyses of similar length are presented in figure 24, and are analyzed in the following discussion at a nominal 5 kts speed.

FIGURE 24. TWO HULL DESIGNS @ L/D 5.25 & 8

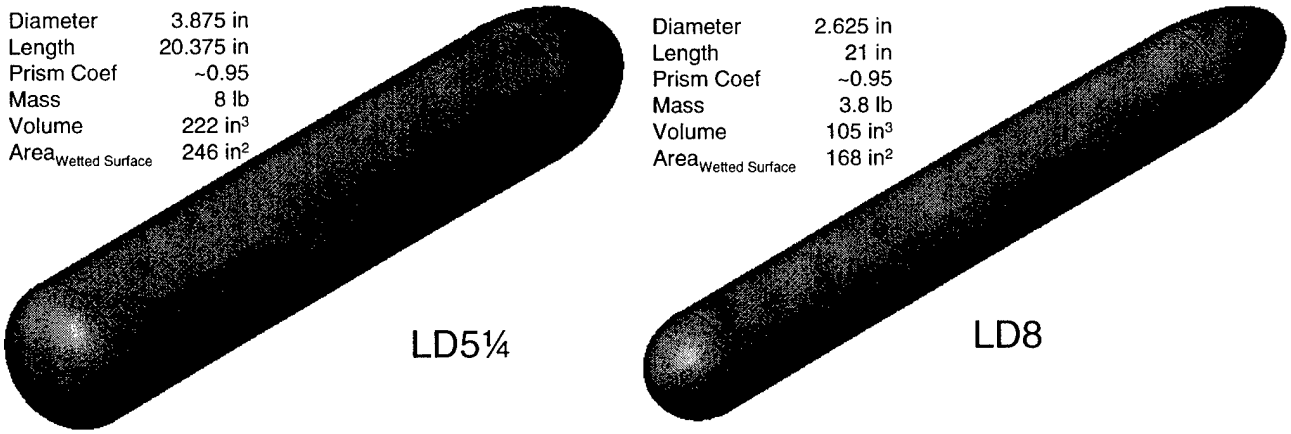

The summary results are shown in figure 25. Although these two point designs do not reach 20 Nm/lbm, they do show a 10x increase in endurance over other conventional platforms (see figure 1). As shown, without a payload the LD5.25 configuration can reach 14 Nm/lbm specific endurance.

FIGURE 25. SPECIFIC ENDURANCE: TWO DESIGNS @ 5 KTS THROUGH WATER SPEED

Payload = 20%

FSL-SS (60% efficiency)		LD5.25 (Nm/lbm)	LD8 (Nm/lbm)
Mass Design Margins	0%	10.11	6.47
	10%	7.93	4.94
	20%	5.74	3.41

50/50 (56.3% efficiency)			
Mass Design Margins	0%	8.03	5.13
	10%	6.29	3.92
	20%	4.56	2.70

High Maneuvering (52.5% efficiency)			
Mass Design Margins	0%	6.16	3.93
	10%	4.83	3.00
	20%	3.50	2.07

Payload = 0%

FSL-SS (60% efficiency)		LD5.25 (Nm/lbm)	LD8 (Nm/lbm)
Mass Design Margins	0%	14.47	9.54
	10%	12.29	8.01
	20%	10.11	6.47

50/50 (56.3% efficiency)			
Mass Design Margins	0%	11.49	7.56
	10%	9.76	6.35
	20%	8.03	5.13

High Maneuvering (52.5% efficiency)			
Mass Design Margins	0%	8.82	5.80
	10%	7.49	4.87
	20%	6.16	3.93

"LD5¼" (Stub Nose Vehicle)

This configuration is a stub-nose, right-circular-cylinder hull configuration as described in figure 24. Mass distribution and stored energy is shown in figure 26.

FIGURE 26. LD5¼ MASS & ENERGY BUDGET

		Unassigned Material 0%	10%	20%
Instrumentation		134	134	134
Motor & Drive Train	13.0%	473	473	473
Hull (including CPCB)	12.0%	437	437	437
Propeller	5.0%	182	182	182
Payload	**20.0%**	**728**	**728**	**728**
Design Margin		**0**	**364**	**728**
Battery		1685	1321	957
Total (8.02 lbs)		**3638**	**3638**	**3638**

Energy Mass %age (of platform mass)	46.3%	36.3%	26.3%
Stored Energy (watt-hrs)	232.0	181.9	131.8

The Drag Force is calculated using

$$F_D = 1.4264 * \rho(T) * C_D * A_{WS} * V^2_{(kts)}$$

The total drag coefficient (C_D) is developed from our initial analysis and for seawater viscosity at 50° F temperature. The subsequent Hydrodynamic Drag Force and Power are shown in figure 27.

FIGURE 27. LD5¼ DRAG FORCE AND POWER

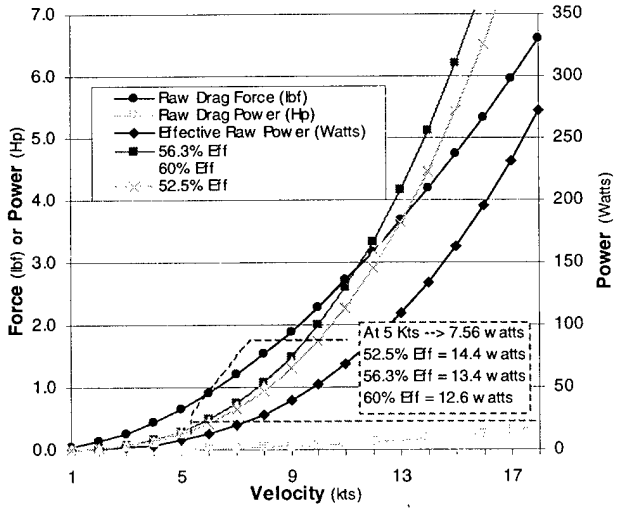

The gross power budget is calculated using the table of figure 23, explicitly applied, as shown in figure 28.

FIGURE 28. LD5¼ GROSS POWER BUDGET @ 5 KTS

		Operating Profiles FSL-SS	Hi-Mnvrs	50/50
Instrumentation Power {IP}		1.74	2.08	1.91
Payload	*(embedded in Instr Power)*	-	-	-
Hydro Drag Power {HD}	*f {hull, speed} ***	7.56	7.56	7.56
Drive Train Efficiency {DTE}	*f {prop design, speed, sterng & diving} ~ estimates*	60.0%	52.5%	56.3%
*** this is captured in the MatLab Drag Analyses, shown here from spreadsheet data*				
	Total Power (watts) {IP + HD/DTE}	**14.34**	**16.48**	**15.35**
	Speed Through Water (kts)	5	5	5
	Speed of Advance (kts)	5	3.5	4.25

We then calculate endurance at a specific through-water velocity as the intersection of power budget, speed of advance, and onboard energy, figure 29.

FIGURE 29. LD 5¼ ENDURANCE CALCULATION @ 5 KTS

NA Design Margin	MicroAUV Stored Energy (watt-hrs)	Forward Speed (kts)	Total Power Demand (watts)	Endurance (hrs)	Range (Nm)	Specific Range (Nm/lbm)
Steady State Forward SOA (60% efficiency)						
0%	232.0	5	14.3	16.2	81	**10.1**
10%	181.9	5	14.3	12.7	63	**7.9**
20%	131.8	5	14.3	9.2	46	**5.7**
50/50 (56.3% efficiency)						
0%	232.0	4.25	15.4	15.1	64	**8.0**
20%	181.9	4.25	15.4	11.8	50	**6.3**
40%	131.8	4.25	15.4	8.6	36	**4.6**
High Maneuvering (52.5% efficiency)						
0%	232.0	3.5	16.5	14.1	49	**6.2**
20%	181.9	3.5	16.5	11.0	39	**4.8**
40%	131.8	3.5	16.5	8.0	28	**3.5**

"LD8" (Stub Nose, Length to Diameter ratio = 8)

This configuration is a stub-nose, right-circular-cylinder hull configuration as described above. For this vehicle the mass distribution and stored energy is shown in Figure 30.

FIGURE 30. LD8 MASS & ENERGY BUDGET

		Unassigned Material 0%	10%	20%
Instrumentation		134	134	134
Motor & Drive Train	13.0%	224	224	224
Hull (including CPCB)	12.0%	206	206	206
Propeller	5.0%	86	86	86
Payload	**20.0%**	**344**	**344**	**344**
Design Margin		**0**	**172**	**344**
Battery		726	554	382
Total (3.8 lbs)		**1720**	**1720**	**1720**
		---------- grams ----------		
Energy Mass %age (of platform mass)		42.2%	32.2%	22.2%
Stored Energy (watt-hrs)		99.9	76.3	52.6

The Drag Force is calculated as above. The total drag coefficient (C_D) is developed from our initial analysis and for seawater viscosity at 50° F temperature. The subsequent Hydrodynamic Drag Force and Power are shown in figure 31 below.

FIGURE 31. LD 8 DRAG FORCE AND POWER

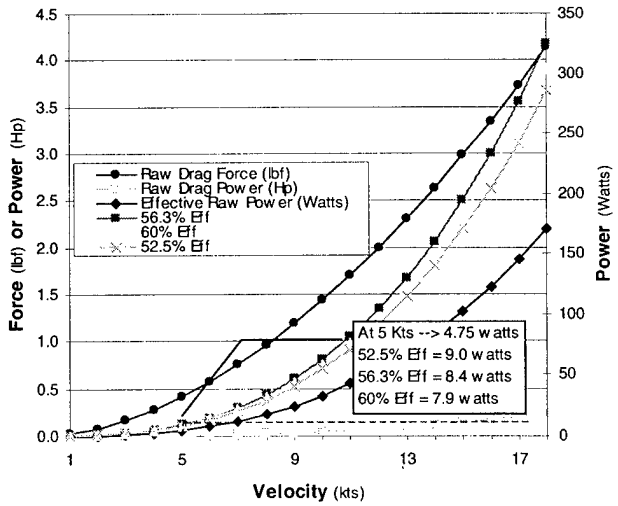

And the gross power budget is calculated as figure 32.

FIGURE 32. LD 8 GROSS POWER BUDGET @ 5 KTS

		Operating Profiles FSL-SS	Hi-Mnvrs	50/50
Instrumentation Power {IP}		1.74	2.08	1.91
Payload	*(embedded in Instr Power)*	-	-	-
Hydro Drag {HD}	*f {hull, speed} ***	5	5	5
Drive Train Efficiency {DTE}	*f {prop design, speed, sterng & diving} ~ estimates*	60.0%	52.5%	56.3%
*** this is captured in the MatLab Drag Analyses, shown here from spreadsheet data*				
	Total Power (watts) {IP + HD/DTE}	**9.65**	**11.12**	**10.34**
	Speed Through Water (kts)	5	5	5
	Speed of Advance (kts)	5	3.5	4.25

We then calculate the endurance as the intersection of power budget, speed of advance, and onboard energy.

FIGURE 33. LD 8 ENDURANCE CALCULATION @ 5 KTS

Design Margin	MicroAUV Stored Energy (watt-hrs)	Forward Speed (kts)	Total Power Demand (watts)	Endurance (hrs)	Range (Nm)	Specific Range (Nm/lbm)
Steady State Forward SOA (60% efficiency)						
0%	99.9	5	9.6	10.4	52	**6.5**
10%	76.3	5	9.6	7.9	40	**4.9**
20%	52.6	5	9.6	5.5	27	**3.4**
50/50 (56.3% efficiency)						
0%	99.9	4.25	10.3	9.7	41	**5.1**
20%	76.3	4.25	10.3	7.4	31	**3.9**
40%	52.6	4.25	10.3	5.1	22	**2.7**
High Maneuvering (52.5% efficiency)						
0%	99.9	3.5	11.1	9.0	31	**3.9**
20%	76.3	3.5	11.1	6.9	24	**3.0**
40%	52.6	3.5	11.1	4.7	17	**2.1**

CONCLUSIONS

Our requirement has been to develop MicroAUV design capable of 20 Nautical Miles range per lbm. The two point designs above demonstrate a system that achieves 10 Nm/lbm, which is ~10x current capability, but does not yet reach the requirement.

A revision to this report, submitted with our System Design Milestone 4 deliverable, will finally select the optimum size, and configuration (diameter, hull shape, Prismatic Coefficient) for MicroAUV. Further that analysis will define maximum anticipated endurance of the design.

RECOMMENDATIONS

We recommend continuing our team's MicroAUV design effort, according to the performance specifications currently defined. It may become appropriate to reduce the performance specification, but we are not ready to do that yet.

Specifically, we plan to

1. Finish our rough hydrodynamic analyses
2. Finish the vehicle preliminary design, due within just a few weeks
3. Conduct demonstrations:
   - Hull hydrodynamics – build and test two or more vehicles as defined in the analysis above at WSU Pullman water tunnel late this summer or early fall. We are still resolving scope of these tests, which will include two or more candidate models (full scale of ~12"–40" length). The tests may be un-powered hydrodynamic drag tests to validate the drag minimum shown in Figure 4, or self-propelled endurance trials.

We anticipate Year two work to finish the efforts listed above and to

4. start design of the onboard intelligence
5. resolve issues
6. resolve final MEMS – Hull design
7. fabricate an integrated MicroAUV prototype, complete with marginal intelligence and test in endurance trials

We would like to initiate the optional task funding to pursue one of the following options:

1. NRL FEFLO (Finite Element Fluid Flow) analytical routines to repeat our rough analyses above and validate compare our findings
2. Examine SMATE active propeller initial design attributes

SUPPORTING DATA - SYSTEM DESIGN ISSUES

This section of this report provides preliminary system design of vehicle components and constitutes the draft input to our milestone 4 deliverable, "Preliminary System Design". These data are developed herein in order to provide salient estimates in developing the Power analyses and to discuss the ability to fabricate MicroAUV as we have discussed in the previous section of the a minimum hull displacement.

The components discussed in this section include

COTS MEMS Components to provide environmental sensing
MEMS Communication, Imaging and Ranging (CIR) System
OTHER Components Page

MICROAUV TOP LEVEL ARCHITECTURE

As described in the Executive Summary section titled New Work – MEMS, the top-level functional architecture of MicroAUV is shown in Figure 34.

FIGURE 34. TOP LEVEL FUNCTIONAL ARCHITECTURE

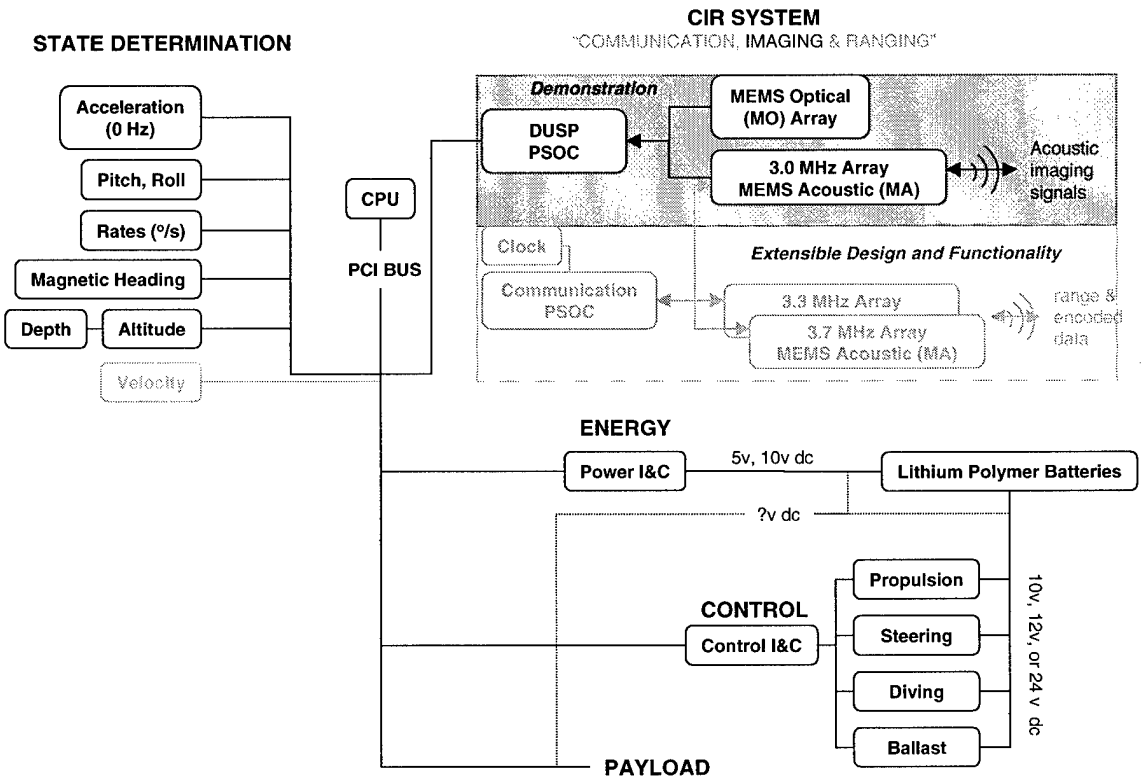

COTS MEMS COMPONENTS

Because of the substantial in-house role in developing the CIR system, those components were discussed in the Executive Summary. Additional electronic components are shown in the following sketch and discussed in the subsections below.

FIGURE 35. COTS MEMS COMPONENTS

State Sensors, Internal Bus and CPU

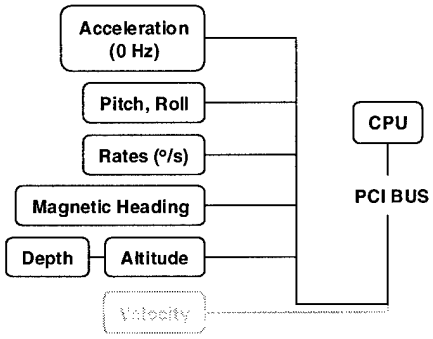

Pitch, Roll, and Heading

We currently intend to use a EZ Compass-3 version 3-axis tilt compensated magnetometer[13] to sense pitch, roll and heading at ~10 milli-Watts power. This device compensates sensed magnetic heading with off-axis pitch and roll tilt. Accuracy is shown in the spec sheet.

FIGURE 36. AN EZ COMPASS™ EXAMPLE

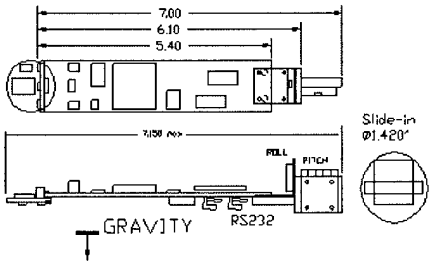

Nominally, this device would consume a substantial volume of MicroAUV. But by working with the vendor to specify the various internal bus, interfaces, and other components into our flexible PCB hull, we can virtually eliminate the volume of this component, by accommodating for it in the hull thickness. Specifications are shown in Figure 37

FIGURE 37. EZ COMPASS™ SPECIFICATIONS

Parameter	Specification	Units/description
Azimuth Range	0--360	deg, continuous
Azimuth Resolution	12 (0.08)	bit (deg)
Azimuth Repeatability	< 0.25	deg, typical
Azimuth Accuracy	< 1	deg, typical
Magnetic Field	+-2	Gauss typical
Magnetic Resolution	< 1	mGauss typical
Pitch Range	+70 to -70	arcdeg linear
Roll Range	+70 to -70	arcdeg linear
Pitch Range	+80 to -80	arcdeg near-linear
Roll Range	+80 to -80	arcdeg near-linear
Tilt Resolution	12	bit full scale, both axis
Tilt Repeatability	<2;	bits
Temperature	-30 to +85	deg C
Communication	300--38400 baud,8,N,1	RS-232 and RS-422 standards
Supply	5 +-10%	Vdc regulated
Size	1.15"diam x 7.15"L	assembly
NMEA-0183 mode	5 select modes	1999 Revision

Acceleration

It is not clear that MicroAUV will need to sense acceleration in order to achieve adequate flight control. Surges at shallow depths (because of wave action) may need to be damped out in the control system or we may resolve that MicroAUV moves through those regimes robustly by passive design (just ignores the surging and keeps on going). If acceleration is sensed, it would be used for flight control and perhaps augmenting position estimator (relative to other units). However, at 5~6 kts forward speed these dynamics may be benign and the acceleration sensor may be eliminated.

If acceleration sensing is installed, we will most likely use something like the Analog Devices ADXL $\pm$2 g Dual Axis Accelerometer[14] at 0.18 milliWatts power. We have acquired 4 samples of these and some other devices for testing in our current concepts.

Rate Gyro,

Given the performance of the EZ Compass, and the pitch and roll data from it, as well as the dynamic period of MicroAUV, we may also be able to eliminate any Rate Gyros and control MicroAUV only on linear feedback of the difference between commanded heading and actual. Further we may be able to control inclination with only pitch and/or depth data and also eliminate rate measurements in the vertical plane. We will finally resolve rate sensors needed, if any, we more thoroughly examine the dynamics of the MicroAUV and define sufficient flight control in year two.

For now, we schedule the use of a MEMS based rate gyro for controlling yaw rate only (again, ignoring the vertical plane). First estimates of heading slew rates on MicroAUV are expected to be 0 to 10 degrees per second in steady state, while we conservatively estimate providing for measurement and control of up to $\pm$150 degrees per second in turning. Current rate gyro selected is an Analog Devices $\pm$150 degree per second, Single Chip Rate Gyro, model No. ADXRS 150 at

~25 milliWatts power[15]. This device is in the beta testing stage and although it is not currently commercially available, we also have 4 confidential samples from Analog Device on hand.

Pressure Sensor (Depth)

Pressure sensor has not been finally selected. We are still comparing some commercial "off-the-shelf" components and custom design components that can be embedded into the hull. At the MEMS size of the hull embedded MEMS systems we are expecting less than 1 milliwatt power demand. Current COTS products include entran EPI subminiature pressure probes[16] (<2 mm) or ICS Sensors PCB mountable sensors at <10 milliwatts power.

However, we are also examining utilizing the bias load (bias signal) on the MEMS Acoustic (MA) Imaging sensor as a method and additional function of that system to detect absolute pressure, hence eliminating the need for a dedicated single purpose COTS sensor.

Velocity Sensor

Non-impacting velocity sensors have been a continual challenge for large application marine applications. Laser technology has been explored, but in large applications the laser technology to reach far enough into the water stream (off hull) to ensure the measurement is not contaminated by laminar flow around the hull has not been demonstrated in the public domain and at reasonable power levels.

However, Caltech developed a micro Laser Doppler Velocimeter that reaches up to 8 cm into the water column (is now licensed to Viosense, Inc.[17]) under Dr. Tang's MEMS program at DARPA.

FIGURE 38. VIOSENSE LDV SKETCH

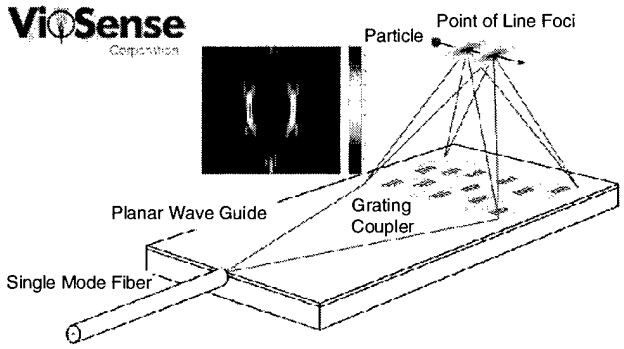

When mounted on MicroAUV, this could equate to 0.5-1.5 body diameters into the water column and could sufficiently achieve a ~0.2 % of velocity measurement accuracy. Integrated with heading and ranging information, the LDV could enable a relative position estimator to enable multiple MicroAUVs to operate in close proximity with a high level of controllability. For continuous operations, the laser requires approximately 100 milliwatts and the supporting electronics also about 100 milliwatts. But we intend to operate the LDV at approximately 10% duty cycle, sampling somewhere between "100 milliseconds duration every 10 seconds" and "10 milliseconds duration every 1 second". Hence, average power demand is ~20 milliwatts.

Altitude Sensor

We are still examining altitude sensing. Operationally, it is not clear that this is necessary. In submerged, terrain following scenarios, we may be able to use the Imaging Subsystem to accomplish terrain following. In other scenarios, we anticipate altitude sensing would be unnecessary. The established best way of accomplishing altitude sensing is by acoustic bounce off the bottom. For shallow water applications, existing COTS systems are generally bulky relative

to MicroAUV design. Some acoustic ranging devices may be viable, but MEMS miniaturization of systems does not yet support MicroAUV goals. We intend to examine shallow water bottom interference of our CIR signal and other acoustic devices to accomplish altitude sensing. Nominal physics of a single transducer of 1.5 square inch area would be ~40 kHz frequency and the energy to get a return from 150 to 200 meter altitude would be ~8 milliwatts-seconds at a 0.01 Hz Sampling rate (1 sample every 100 seconds).

MEMS COMMUNICATION, IMAGING, AND RANGING SYSTEM

Figure 39 shows the current MicroAUV design and the extensible design, anticipated for later implementation.

FIGURE 39. CIR SYSTEM

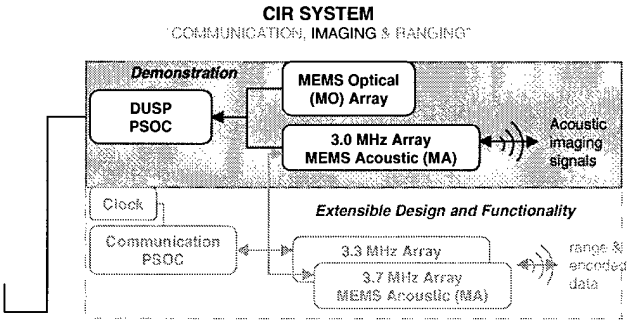

Acoustic Imaging Power Budget

As presented in our initial report, the estimated raw power to transmit and receive over 30 meters is on the order of 1~2 milliwatts. The acoustic power of the CIR System is based:

- on theoretical analysis provided in our initial report and revised as attachment 4 to this report. This power is required to transmit a signal out to a certain distance with a return.
- operational power of the other onboard electronics to accomplish signal process needs.

Figure 40 shows the theoretical output associated with a continuous wave acoustic energy transmission at 3 ~ 4 MHz versus range. Attachment 4 provides analyses that defend the curve. The range shown is the distance this signal would transmit to, reflect off an obstacle, and return from and still be observable at a signal strength of ~4.2 decibels re 1 micro-Pascal @ 1 meter (10 millivolts). This is conservative, as we have experience with detection sensor capabilities able to discern signal presence down to considerably lower levels in a variety of applications. The key to ensuring detectability will be in our array gains and detection sensitivity aspects of our sensor design.

FIGURE 40. ACOUSTIC PULSE POWER

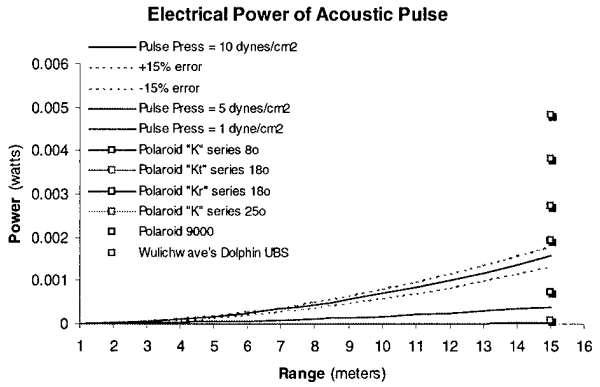

Figure 20 tabulates our current estimate of the subcomponent power levels for the CIR. Our current allocation for acoustic devices is 450 milliwatts and is this high to allocate for losses we are not yet certain of and to provide for margin to increase output power based on possible operating scenarios of the vehicle.

System and is consistent with current understanding of "in house" and University of Washington design efforts, as further explained in Attachment 4, plus it includes reasonable estimates for communications transmit and processing power as they may emerge in implementing the communication capability of the CIR system. These data are living data and will be revised as the design matures

MEMS Acoustic(MA) Sensor Description

The MEMS Acoustic (MA) sensor will consist of an array of piezoelectric-capacitive spring mesh membranes coated with a piezoelectric material. The MA will be a subsystem to the Communication, Imaging, and Ranging (CIR) System. Ultimately the MA array will be a 32 X 32 array to be consistent with the MEMS Optical (MO) array which will also be 32 X 32. Due to fabrication limitations in the prototyping process, the initial prototype MA will be a 4 X 4 array on a 2.5 mm X 2.5 mm chip. We will lay out the chip with bond pads and circuitry along two edges of the chip and the 4 X 4 acoustic array biased towards the other two edges. This design will facilitate assembling four basic chips together to form a larger array (see Figure 41). To better understand Post Fabrication assembly limitations, we may test this configuration this fall.

FIGURE 41. 8 X 8 MEMS ACOUSTIC SENSOR

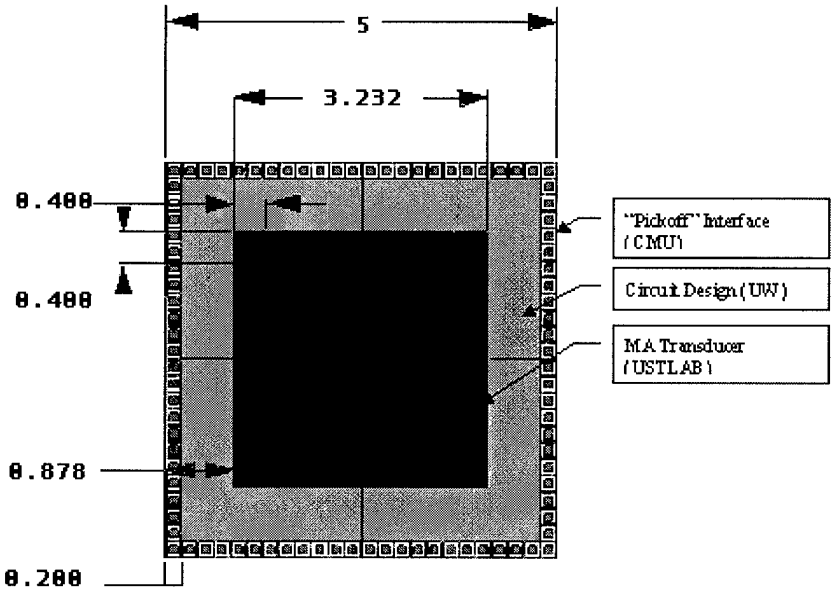

MEMS Acoustic (MA) Sensor Fabrication

The MA device will be fabricated through the Carnegie Mellon University and DARPA MTO sponsored Carbon Metal Oxide Semiconductor (CMOS) Micro Electro-Mechanical Machine Systems (MEMS) Application-Specific Integrated MEMS Process Service (ASIMPS) program described below. The CMOS-MEMS ASIMPS process will allow the MA sensor device to have an acoustic MEMS transducer array and associated circuitry integrated on the same chip. A baseline array element (pixel) will nominally be a 400 μm X 400 μm square membrane. This dimension represents one wavelength at the tuned frequency of 3.75 MHz. Each pixel in the acoustic array will be a trampoline-like membrane with a capacitive, piezoelectric material coating (see Figures 42 & 43).

FIGURE 42. PIXEL CROSS SECTION SIDE VIEW

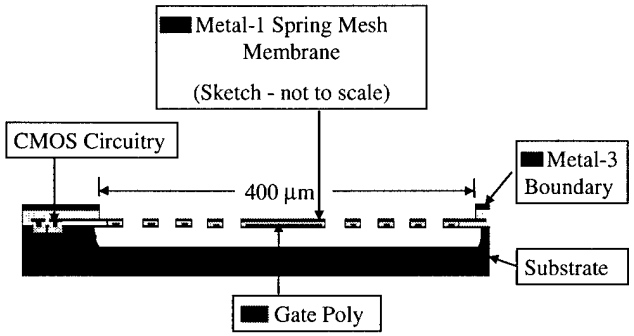

The trampoline-like membrane will be made up of an etched serpentine spring mesh in the metal-1/polysilicon layers, which will then be coated by gaseous deposition of a piezoelectric film.

FIGURE 43. PIXEL TOP VIEW

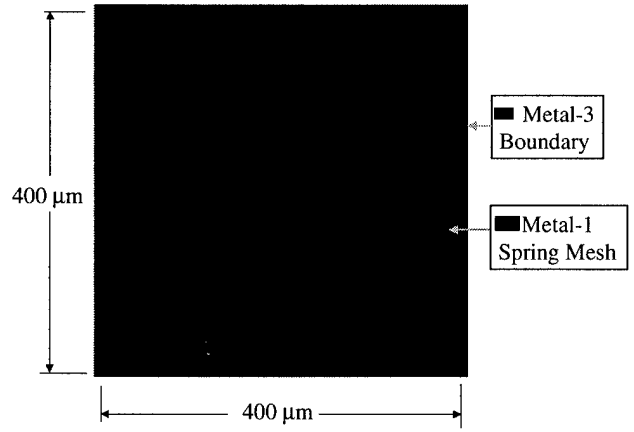

The black areas in the top view will be etched away and the blue metal-1 spring will be under etched to release the mesh membrane from the substrate. The metal-3 boundary will act as a mask and prevent etching in that region. The metal-3 layer also protects the underlying CMOS circuitry. The mesh membrane will then be coated with a piezoelectric material using a gaseous deposition. The coating will fill in the gaps between the spring mesh and complete the membrane film.

The spring mesh elements will be 1.5 μm wide with a 1.5 μm spacing between elements. This spacing will allow sufficient space for etch release of the membrane, and will be close enough to

allow fill in by the gaseous deposition of the piezoelectric coating. The spring mesh will give the membrane flexibility, while also providing the electrical connectivity through the metal-1 CMOS layer to the surrounding circuitry. The ground plane will be the underlying substrate.

MA IMAGING

Transmit

Each MA piezoelectric pixel element in the array will be excited by a 3 MHz sinusoidal electrical excitation energy, which will cause the membrane to vibrate at the resonant frequency. The acoustic signal will travel outward. The membrane vibration will cause a velocity change in the surrounding fluid and the membrane vibration will be transformed into an acoustic wave. The acoustic wave will travel out from the device at the speed of sound, which is nominally 1500 m/sec in seawater.

Receipt

The returning echo acoustic wave from an obstacle will induce vibration in the membrane, which will then cause a change in the capacitance of the plate and will induce a voltage signal on the membrane. To illuminate a "screen" in the field of view (15 meters out) ~19 milliseconds later, processor electronics will start acquiring energy from each pixel as it is excited. Beam forming will be used to detect the field of view without cross contamination of pixel data. The excitation signal will be the source signal reverberated off obstacles in the "field of view". Energy acquisition will continue for another 30~40 milliseconds to achieve a 1 meter or better resolution and illuminate a total area of 10~15 meters at ~15 meters range. Energy acquisition will stop to ensure each pixel is not contaminated by incoming energy from obstacles in other locations on the gross area being illuminated. The illuminated volume will be about 1 cm thick.

The Dual Use Signal Processor will sample each pixel membrane element, form an image and provide the data to the Vehicle Control Computer for to support obstacle avoidance and navigation decisions.

The 8x8 array will result in a beam width of 31 degrees, corresponding to an image 10 to 15 meters across at ~15 meters out. Each pixel will represent ~1 meter square. A series of 8 X 8 images will be taken to represent slices in space ranging from a range of 15 to 30 meters from the vehicle.

The device design provides extensibility towards additional components and functionality, sufficient to support the communication and/or ranging of the CIR notional concept, as discussed below.

MA Communications and Identification

The MA design can be extended to include three arrays, each with pixels as above and each array's pixel design tuned to a separate frequency. Three prototypes will be made with different size array element membranes representing the wavelength of the three frequencies 3.0, 3.3, and 3.75 MHz. A communication and ranging system design similar to that used on Large Scale Vehicles, KOKANEE and CUTTHROAT[18] will be used. The three separate frequency arrays will encode outgoing data and decode incoming data using a Frequency Shift Key protocol. At the base frequency a bit width will be 10^{-5} sec (30+ cycles in each bit). A 1 ms transmit pulse will contain 100 bits of information, and a 10 ms transmit pulse could be used to pass 1000 bits of information. Using seven bits for identification will allow up to 128 units to operate collaboratively with unique identifiers. The remaining bits will be used for communication and the design of the data word would be developed in year three.

We will need to complete analysis of number of units, clocking synchronization, ranging distances and data bandwidth to finalize actual transmission and signal architecture. However, in multiple

operations, each Micro could transmit a 10ms data word every 1-10 sec and could be used by other units to net hop data. Stepping the transmit clock for successive units "down the line" could be implemented so that every 10th MicroAUV in the swarm transmitted at the same time and these units would be far enough apart to not be heard by (and not confuse) other peer units. Ultimately, the Transmit Protocol will depend on the mission, range between units, and the number of collaborative units operating together.

MA Ranging Transmit/Receive

Ranging will be determined by synchronizing clocks on each MicroAUV. When the first bit of a specific transmit signal from one unit is received, the system clock counter stops and converts the time from ping to receipt into a range. After extracting the unit number id from the data word of the transmit signal, the receiving unit now has unit id and relative range data, to be used for relative navigation.

MEMS Optical (MO) Sensor Description

The MEMS Optical (MO) sensor is still being evaluated. UW is pursuing the development of a custom CMOS-MEMS "Camera on a Chip". The USTLAB/UW team has also identified several commercially available "Camera on a Chip" devices. Details on these two options are described in the UW report on the Integrated Sensing and Dual-Use Signal Processing[2].

Dual Use Signal Processing

The Dual Use Signal Processor[19] will take data from either the MA or the MO. The processing steps applied will be smoothing, segmentation, detection, and avoidance. The smoothing algorithm will help minimize noise, and will extract signal from the image data by difference processing a baseline and current image. This information will then be processed through a threshold detector that will generate output data to the memory map where values exceed the threshold. Segmentation will break the image up into segments that will be used to identify areas to avoid or maneuver towards depending on signal in that segment of the image. The segmentation algorithm will generate a matrix of probabilities that an object exists in that segment. By evaluating these probabilities the location of the object can be detected and a navigation decision made to avoid the region with the obstacle. This processing would be the same for both MA and MO sensors.

System Interconnect

The objective of μAUV will be to design the MEMS packaging as a flexible circuit that will have the MEMS die bonded directly to the flex circuitry and then rolled up and built up into a composite structure which will be the hull of the μAUV. The acoustic and other sensors will be on the external surface of the hull with a compliant urethane coating that will allow access to the sensed environment. The interconnect between the MEMS devices will be the flex circuitry, and will be integral to the hull. This is described in more detail in the μAUV – Imaging System MAMO DUSP ICD.

MEMS Fabrication Issues

Workshops

The direction of MEMS design is towards more complex electro-mechanical sensor and actuator devices at sub micron, and micron to millimeter scale. The current trend is towards "smart" devices with integrated circuit and MEMS devices on the same chip. To establish an understanding of

MEMS fabrication issues, our team attended several workshops and conferences. Some of these included:

Sandia Introductory MEMS **November, 2000**

Sandia National Laboratory introduced potential industry partners to their MEMS SUMMiT process (Sandia's Ultra-planer Multi-level MEMS Technology). This is a five layer planerized poly-silicon surface micromachining process. Prototype designs are realized through the SAMPLES Program (Sandia's Agile MEMS Prototyping, Layout Tools, Education and Service), that culminates in the design and production run, testing and delivery of prototype devices in a multi-organization process run. Includes introduction to SUMMiT Design Rules, Rule checking and reliability analysis capabilities.

Sandia MEMS Reliability **November, 2000**

Sandia provided in depth exposure to the current state of MEMS reliability characterization, including:

- Taxonomy for characterization and testing
- assessment of the reliability of MEMS products in varying environmental exposures
- practical examples of MEMS failure characterization.

Sandia Advanced MEMS **March, 2001**

Sandia provided in depth exposure to design in the Sandia Fabrication Process SUMMiT V.

Carnegie Mellon University ASIMPS **March, 2001**

CMU introduced potential industry partners and other Alpha users to the CMOS-MEMS Design for the Application-Specific MEMS Process Service (ASIMPS). This is a Carnegie Mellon University initiative sponsored by DARPA MTO.

MEMS Fabrication Technologies

There is a broad spectrum of MEMS fabrication technologies available. The three most commonly used are:

- Bulk Micromachining – 3D micro structures formed by bulk etching of silicon substrate using wet and/or dry chemical etch
- LIGA Lithographie, Galvanoformung (electroforming), Abformung (injection molding) – 3D structures formed by mold fabrication followed by injection molding
- Surface Micromachining – low profile 2D+ structures formed by alternate polysilicon deposition, patterning, and etching of sacrificial structural and thin films.

The Sandia National Lab has facilities for all of the above fabrication technologies, but the process being used for technology transfer and cooperative prototyping is a five layer surface micromachining process described below.

SANDIA National Labs SUMMiT Five Process

The Sandia National Lab (SNL) has developed a joint user prototype program called the Sandia's Agile MEMS Prototyping, Layout Tools, Education, and Services (SAMPLES)[20]. This program is intended as a "springboard" opportunity for potential partners interested in MEMS to demonstrate prototypes in a cooperative setting to reduce costs.

The Sandia Ultra-Planer Multi-level MEMS Technology (SUMMiT) Five (for five poly-silicon layers) process. Poly-silicon nitride and silicon dioxide layers are applied by a combination of Low

Pressure Chemical-Vaper Deposition (LPCVD) and Plasma Enhanced CVD. After the layers are deposited they are coated with photo-resist, and photolithography is used to pattern the thin film layers. The photo-resist is pattern through a mask with ultra-violet light, which makes the exposed areas soluble in the developer. The non-developed area is resistant to etching. The developed areas are unprotected and are etched away during the etching process. Sandia uses both wet and dry etching processes. Wet etching is a chemical etch which has high selectivity and has the ability to remove contaminants. It has an isotropic etch profile. Dry etching uses an energetic plasma to create an anisotropic etch profile. The most common is a Reactive Ion Etch. Is a relatively low temperature process. The process is physically and chemically complex and requires a great deal of control.

Topography variation with multiple layers of conformal material deposition generally limits the number of levels of poly-silicon. Since the Sandia SUMMiT V process is a conformal five layer process, Chemical-Mechanical Polishing (CMP) is used to planerize the surface between major layers. This planerization limits stringers and interference between levels. It also allows Sandia to achieve the five layer process.

The process consists of five polysilicon layers and associated sacrificial oxide layers. The layers and their thickness are:

SUMMiT V MEMS Layer	**Thickness**
Mmpoly4	2.25 μm thick
Sacox4	2.0 μm thick (CMP)
Mmpoly3	2.25 μm thick
Sacox3	2.0 μm thick (CMP)
Mmpoly2	1.5 μm thick
Sacox2	0.3 μm thick
Mmpoly1	1.0 μm thick
Sacox1	2.0 μm thick
Mmpoly0	0.3 μm thick
Silicon Nitride	0.8 μm thick
Thermal SiO2	0.63 μm thick
Substrate	

With five layers of structural poly-silicon complex mechanical structures are possible. Examples are five layer rotary motors, comb drives, geared transmissions, pumps, steam engineers, and complex micro-actuators.

The SNL MEMS process uses 6 inch diameter silicon substrate n-type phosphorous doped wafer. Resistivity is 2-20 ohms-cm The industry is using 8 inch diameter wafers. The Sandia process is being upgraded to 8 inch wafers. Typical oxide deposition processes are done at 1050 degrees C, for 100 min to get 6300 Angstrom thick oxide. Typical Integrated Circuit (IC) oxide thickness' range from 50 Angstrom for the gate oxide to 6300 Angstrom for the field oxide. Typical MEMS oxide thickness range from 6300 Angstroms to 2 microns.

Polysilicon Surface Micromachining leverages the existing IC foundry infrastructure (40 years experience base). It is the front end process for CMOS circuits. It has the potential for integrated MEMS and electronics. However, there is no "definitive" micromachining technology. There are several independent organizations working to build a standard technology. Additionally, there is a difference in feature size between Integrated Circuits (IC) and MEMS. The following information comparing IC to MEMS feature sizes was extracted from SNL workshop notes[20].

Feature	IC's	MEMS
Film Thickness (μm)	<1	2-6
Critical Dimension (μm)	0.35	1
Aspect Ratio (μm)	2:1	10:1
Topography – Step Height (μm)	<1	4-10
Device Size (μm)	1	100

The material properties of silicon and silicon compounds make these materials useful for micro actuation. The table below compares the material properties of silicon, silicon dioxide and silicon nitride with steel.

MEMS Material Properties Table

Property	Polysilicon	Silicon Dioxide	Silicon Nitride	Steel
Primary use in MEMS	**Structural**	**Sacrificial Layer**	**Insulation, Mask, Lube**	**Comparison**
Molecular Weight	28.09	60.08	84.11	
Molecule Density (molecules/μm)	4.995×10^{10}	2.3×10^{10}		
Melting Point (°C)	1415	1700		1500
Mechanical Properties				
Young's Modulus (N/μm)	0.160	0.069	0.27	0.207
Modulus of Rigidity (N/μm)	0.0772		0.109	0.079
Ultimate Strength, Tension (N/μm)	0.00155	0.00069	0.0027	0.0004
Fracture Strength (Gpa)	1.6			
Coefficient of Thermal Expansion (/°C)	2.5×10^{-6}	0.5×10^{-6}	4×10^{-6}	10.8×10^{-6}
Poisson's Ratio	0.23		0.24	0.292
Knoop Hardness (kg/mm)	850		3486	1500
Density (g/μm)-solid	2.33×10^{-12}	2.27×10^{-12}	2.95×10^{-12}	7.9×10^{-12}
Electrical Properties				
Resistivity (Ω-μm)	23	5×10^{11}	1×10^{11}	0.093
Dielectric Constant	Conductor	3.9	6.5	Conductor
Poly 0 Resistivity (Ω/square μ)	40			
Poly 1 or 2 Resistivitance	20			

(Ω/square μ)				
Poly 1+2 Resistivitance (Ω/square μ)	10			
Poly 3 Resistivitnace (Ω/square μ)	10			

SUMMiT Process Advantages: The successful development of MEMS requires significant resources. People interested in developing MEMS, whether they be university researchers or companies desiring to market a product, need to invest their resources wisely in the current world of fast-paced technology development.

Sandia National Laboratories has aggressively developed the infrastructure needed for advanced MEMS development.

SNL has become a world leader in MEMS-related innovations.

SNL provides technology transfer to companies, and institutions.

SNL has developed a five layer planarized polysilicon surface micromachining process conducive to complex mechanical structures

Relatively low cost of $10,000/fab run compared to full infrastructure development.

SNL provides prototype design and analysis, and testing services.

SUMMiT Process Disadvantages:

An integrated CMOS after MEMS process has been demonstrated, but has not been put into SAMPLES program and a prototype run would be stand alone and expensive.

Tools are focused on complex gearing and micro engines, and do not provide basic sensor building blocks.

Carnegie Mellon University CMOS-MEMS Application-Specific MEMS Process Service (ASIMPS)

Under a DARPA MTO sponsored process development initiative, The Department of Electrical and Computer Engineering and the Robotics Institute of Carnegie Mellon University, Pittsburgh PA have initiated development of an integrated CMOS-MEMS fabrication process. This fabrication process is called the CMOS-MEMS Application-Specific MEMS Process Service (ASIMPS)[21]. CMU is working jointly with MEMSCAP and Austria Mikro Systeme International AG (AMS) to demonstrate an integrated CMOS-MEMS process. CMU is working with MEMScaP to customize commercially available Microelectronic CAD frameworks (CADENCE, MEMSPro, HSPICE, and Design tools) to streamline and facilitate technology transfer of circuit level design methodology to an integrated circuit-MEMS design environment.

For circuit-level design tools to be truly useful to an integrated CMOS-MEMS process, it is necessary to identify a set of components, characterize the process, establish design rules, and integrate the devices into the tools. The ASIMPS program at CMU is springboarding from existing tools and adapting them to this process. The ASIMPS program is using a co-op Alpha-user approach to demonstrate and qualify this process.

ASIMPS goals - The goals of the DARPA-MEMS (Dr.Bill Tang) sponsored CMU ASIMPS project is to:

- enable a path to application-specific integrated MEMS with low production volumes (<100,000) and low cost (<$100/part).

- Reduce the problem of integrated MEMS to a problem of design process and end application know-how rather than one of process development.

As a result the CMU CMOS-MEMS ASIMPS program is providing design, fabrication, and characterization of CMOS MEMS components through a low risk, low cost path to prototype fabrication. This service is being provided as a multi-project process service to a group of Alpha-Users. The first Alpha-User group submitted designs in September 2000 with cmos wafers back in March 2001 and micromachining steps in April 2001. The second Alpha-User group will submit designs in June 2001 and wafers from fab in September 2001.

ASIMPS Process Description

The ASIMPS process is based on the Austria Mikro Systeme International AG (AMS) in Berlin Germany cmos process. The process will be the AMS 0.6 μm 3-metal, 2-poly standard cmos process, with CRONOS runs post-cmos micromachining steps. Traditionally the problem with MEMS micromachining after cmos has been damage to the cmos circuitry by the high temperature MEMS process. This problem is alleviated in the ASIMPS process by using the metal 3 layer to protect the underlying cmos circuitry. There has been one Alpha-user run we will be in the second Alpha-user run. The plan is to have tape out end of June 2001. CMU has requested designs by 5 Jun 2001. Expect wafers back from fab nominally Sept 2001. The metal-3 layer will protect the underlying cmos circuitry. Metal-3 will be etched away in way of the MEMS device and the whole die will have an overglass coating. Post cmos reactive-ion etch will remove the dielectric layers where the metal three has been removed. The top metal layer (metal-3) acts as a mask and protects the CMOS circuits. There will also be a post-CMOS etch of the silicon substrate that will undercut and release the MEMS structure. Chemical Mechanical Polishing is done before metal-2 and metal-3 layers.

ASIMPS Process Advantages:

- Integrated CMOS and MEMS technology.
- Low Cost - $300/process run.
- Using CMOS metal layers as part of the MEMS structure provides flexibility in wiring devices to circuits on chip.
- Building on existing commercially available circuit layout and MEMS cad packages. Tanner L-edit™ and MEMSCap™ MEMSPro™ software.
- Building on existing commercially available circuit analysis and simulation packages. Tanner Tools S-edit™, T-edit™ W-edit™.

ASIMPS Process Disadvantages:

- New process, all development tools not yet in place
- Limited prototype development area – process yields a 2.5 μm X 2.5 μm die set of four dies per Alpha-user.

MEMS Reliability

MEMS Reliability Issues – understanding failure mechanisms is key

Understanding MEMS failure mechanisms is key to designing for reliability. This understanding is hampered by the fact that there are no industry standard technologies. Additionally, numerous institutions are independently developing MEMS fabrication technologies, and most are application specific. The development of design protocols typically lags the industry. Finally, packaging

issues are not generally addressed up-front in the design. This results in MEMS devices, which do not meet the full potential of micro-miniaturization, and may in fact impact the reliability.

While the MEMS fabrication technology is generally based on the IC industry, the MEMS failure mechanisms are more varied than the IC. There has been little work on characterizing MEMS failure mechanisms. Also, a standard Taxonomy for characterizing MEMS failure mechanisms is lacking.

Summary of Failure Mechanisms Requiring Concern

MEMS Failure Mechanisms	
Mechanical Wear	Thermal Cycling
Fatigue	Thermal Degradation
Fracture	Humidity
Stiction	Stress Corrosion Cracking
Shock	Creep
Vibration	Environmental Degradation
Charging	Radiation
Particles	Change in Friction
Optical Degradation	

MEMS Reliability Approach

SANDIA National Lab[22] recommends a Reliability Qualification Triad which balances Design, Materials/Fabrication, and Packaging/Operation Reliability. A standard industry wide taxonomy is needed to characterize failure mechanisms. The Standard MEMS Failure Mechanism Taxonomy recommended by SNL is the McWhorter's Taxonomy for MEMS Devices[3]. McWhorter's Taxonomy proposes a four-class system

Class I – No moving parts

Class II – Moving Parts, no rubbing or impacting surfaces

Class III – Moving Parts, impacting surfaces

Class IV – Moving Parts, rubbing and impacting surfaces

The SNL approach recommends the development of a product/reliability characterization matrix with classes of products on one-dimension and failure mechanisms on the other. The elements of the matrix would then be filled in as the mechanisms are characterized as to risk to reliability.

Packaging reliability

Packaging reliability is a major concern, and usually the last area of the design addressed. Packaging should be addressed up-front in the design process. Typically packaging limits the MEMS device from achieving it's full micro-miniaturization potential. In the IC industry packaging typically accounts for one third of the cost of a device.

Packaging of IC devices provides the functions of signal distribution, power distribution, heat dissipation, and protection. MEMS devices have additional packaging requirements, which often will be application specific. Packaging must be reduced in size to achieve the full micro-

miniaturization potential of MEMS technology. MEMS packaging may require direct interaction with the environment in the case of sensors and actuators.

OTHER COMPONENTS

Battery

Currently, we have selected Lithium Polymer battery technology as the battery of choice. Final battery selection will be developed as current battery capabilities are reviewed in detail design stage, wherein we will also specify the battery fabrication to optimally utilize all of the vehicle volume and Reserve Buoyancy in considering the mass, dimensions and configuration of the battery cells. Several battery vendors have been examined, including Valence[23] and Telcordia, which offers the Plion™[24] flexible battery system. A custom fabrication is expected in the final analysis, although a Plion-like flexible battery may be used for prototype demonstrations in year two.

These Lithium battery products can achieve 2 to 5 times Nickel Cadmium power densities in a water equivalent packaging arrangement. Even though power density may be up for certain chemistries, mass density can mitigate the value of increased power density. Higher mass dense batteries must be compensated for in submerged underwater applications by adding empty volume to achieve a neutrally buoyant condition.

For purposes of completing endurance calculations, we have selected a **VALENCE Inc.** lithium polymer battery, **Model 25 Series (IMP0X/25/110)™**. These batteries are commercially available, "current, off-the-shelf (COTS)" technology. We use battery cell mass shown on the specification sheet and calculate an average specific energy as 0.138 watt-hrs/gram. WE use this specific energy in our Matlab™ calculations to convert the vehicle energy mass into energy and then to apply the operations scenario to calculate endurance.

FIGURE 44. VALENCE LITHIUM POLYMER

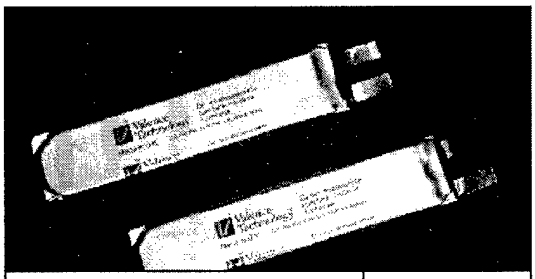

Nominal Voltage	3.8 V
Standard Charge: Constant Current to 4.2 V followed by Constant Voltage to C/20	C/2 to 4.2 V

Dimensions		
Width	25 mm (Max)	
Height	110 mm (Max)	
Nominal Thickness	Nominal Capacity	Nominal Weight
3.3 mm	620 mAh	18 g
4.3 mm	830 mAh	23 g
5.4 mm	1030 mAh	28 g
6.4 mm	1235 mAh	34 g
8.4 mm	1650 mAh	44 g

Propeller

As stated in our first report[1], it is uncertain as to whether an undulating propulsion methodology will gain sufficient efficiency over rotary propellers for sustained operation. In summary of that observation, Fish[6] noted that fish can sustain velocities of 1 to 2 body lengths per second for long periods and that velocities of 3+ body lengths per second equate to "sprinting", which fish cannot sustained for very long.

Uncertain as to the hydrodynamic significance of this observation for fixed bodies, it appears to make sense to veer away from undulatory propulsion methods if MicroAUV size and operating speed regimes tend to be above 3+ body lengths per second.

We anticipate the optimum design of MicroAUV to be between 1 to 3 feet in length. Hence, 5 kts (8.5 fps) represents 2+ body lengths per second up to ~ 8 body lengths per second. Undulatory motion may ultimately be more efficient. For now, this design effort is focusing on rotary propulsion, along with implementing some potentially interesting applications made possible by vehicle diameters of 2 to 4 inches and the current state of electro-active polymers (EAP) and thermoelectrically controlled shape memory actuation (SMATE).

MicroAUV's Propeller design is conceived to be a forward raked, skewed, propeller of certain pitch. The forward rake provides for a soft trailing edge that tapers to a point at the after end. This mitigates "blade pumping" in the water flow and is expected to increase efficiency. In the limit, the propeller would be a screw drive. However, "in the limit" the growth of drag as consequence of increased skin friction drives performance to be no better and likely worse than a conventional propeller. In year two, we will conduct analysis to define a regime of optimum forward rake, which provides maximum efficiency and minimum self-drag at nominal forward velocities.

FIGURE 45. PROPELLER CONCEPTS

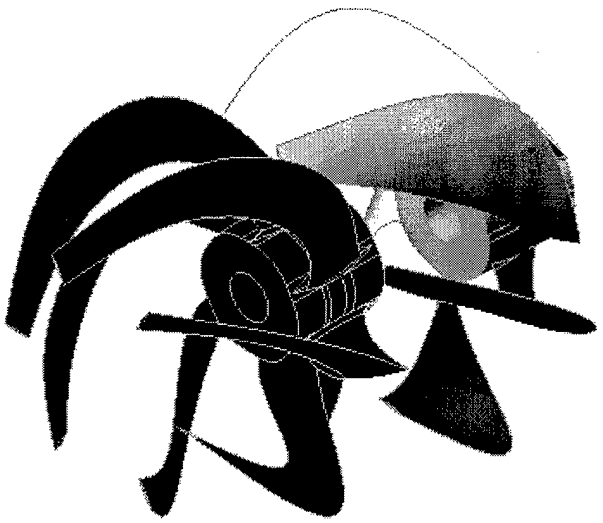

As one option to support steering and diving controllability, we are pursuing "morphable" MicroAUV propeller designs. By "morphable" we mean that pitch, skew, rake, camber are all dimensional attributes that can be varied, according to the need of the platform, to affect variable speed, thrust and/or steering and diving control. Large dimensional or high slew rate changes are not anticipated. However, small changes (~20% of nominal dimensions) multiplied throughout all

blades are both possible and are likely to be effective in achieving the variable control desired. Two actuator technologies are viable to accomplish propeller morphing:

Electro Active Polymer (EAP) technology has advanced considerably[25]. Shape Memory Actuators have historically consumed considerable heating power and were previously inefficient. Today, integrated and actively controlled with Thermal Electric material, SMATE actuators are also a viable technology. EAP or SMATE material can be examined to develop a "morphable" propeller.

Oak Ridge National Laboratory and ITN Energy Systems have been working on a SMATE material concept, which when developed, could potentially provide a substantive solution to a morphable propeller.

FIGURE 46. SMATE MORPHABILITY

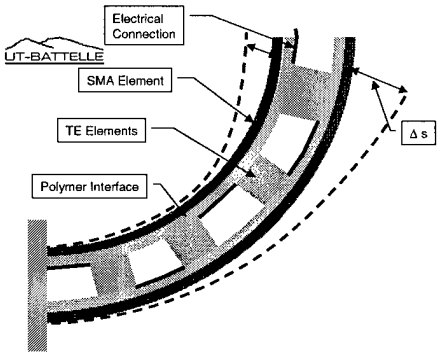

We submitted a proposal with ORNL and ITN to pursue development of this morphable system to the DARPA Compact Hybrid Actuator Program (CHAP – Dr. Garcia - which was not awarded). We have also spoken with Dr. Pramode BandyoBaphyay[26] at ONR, who has requested an SBIR task for biologically inspired propulsion systems and to which this concept may find some funding support.

Properly selecting the pitch and camber to the speed and thrust requirement in conventional propeller designs enables achieving up to 89% open water propulsive efficiency at some nominal operating speed. However, we are conservatively using 85% propeller efficiency and allocating an additional 10% reduction in efficiency (to ~75%) to accommodate losses in using the propulsion system to steer MicroAUV (see below).

Steering and Diving

The default Steering and Diving system design will be the "morphable" propeller. We would attempt to design "morphability" so as to enable operations as described in the executive summary, which would vary the thrust vector off-axis from the body longitudinal to achieve steering and diving control. Examinations into a "morphable" propeller may render propeller designs which are not viable for propulsion.

FIGURE 47. SMATE CONTROL SURFACE

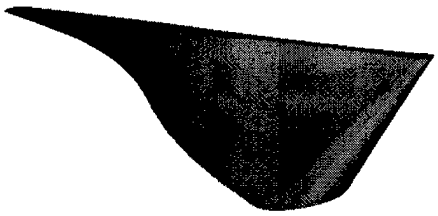

However, these efforts may develop solutions viable for steering and depth control when implemented in morphable control surfaces. For instance, we could energize an SMATE material control surface to an off-nominal configuration to affect steering or diving. Subsequently, naturally occurring cooling could return the device to nominal configuration.

Propulsion Motor

MicroAUV motor is a rare earth magnet (neodymium) motors, such as:

- Koford's 36D-416A type brushless motor with a 308:1 gear reducer[27], or
- MicroMo's Coreless DC Motor[28] or Prototype 175 watt motor (scheduled for 2nd qrtr 01 release)

These motors provide for variable speed control with a cumulative system electro mechanical efficiency of between 70% to 80%. Such design is appropriate for Micro AUV to transit at a steady state nominal velocity, selected to be ~5 kts. Hence, the assembled Drive Train Efficiency would be somewhere between 52.5% to 60%, which we will allocate to "hi-maneuvering" and "Fly Straight & Level – Steady State" modes respectively. The final motor and gearing design will be developed to be integral to the power and rpm desired. We are allocating 18% of vehicle mass to propulsion drive train (including propeller & steering and diving).

Payload

In accordance with our specification, we have allocated 0.3 watts continuous duty power to a payload of undetermined function. Accommodating for 5 watts peak power to the payload is not used in estimating endurance, but would be necessary in developing the final configuration of the battery to ensure the proper alignment of voltage "busing" and current rating of cells to get the peak power requirement.

References

1 "USTLAB TR-01.001 MicroAUV – Scope of Possibility" dtd January 2001

2 S. Goldstein, ***Modern Developments in Fluid Dynamics***, Oxford, Clarendon Press, 1938

3 Taylor, G. I., "Analysis of the Swimming of MicroScopic Organisms", Proceeding of the Royal Society, vol 209, 1950, pp447-4612

4 Lighthill, M.J., "Aquatic Animal Propulsion of High Hydro-Mechanical Efficiency", J. Fluid Mechanics, 1970, Vol 44 part2 pp 265-301,

5 Jackson, H., ***"Submarine Design Notes"***, MIT Press, 1981

6 Fish, F.E. "Review of Natural Underwater Modes of Propulsion", pg 51, Dept of Biology, West Chester University, West Chester PA1983

7 Discussion /w William Sandberg, Naval Research Laboratory, Washington DC, 3/28/2001 regards finite element hydrodynamic drag calculations on submerged bodies. Facility description at http://www.lcp.nrl.navy.mil/cfd-cta/CFD3

8 USTLAB TR – 01.002, "μ-AUV Performance Specification" (Microminiature Autonomous Underwater Vehicle), Revision "0", February 2001

9 ONR SBA STTR (Small Business Technology Transfer Research Initiative) Topic N01-T001, "Autonomous Distributed Systems"

10 Curtin, T, email dtd 2/23/01 regards STTR topic N01-T001, Autonomous Distributed Systems, (survey accuracies for fixed objects)

11 cranney, j., "Unmanned Underwater Vehicle Survey Market Survey", SAIC Contract PO 8200010646, Jan 2000

12 Volume formula for an ellipsoid body of rotation volume, http://www.sisweb.com/math/geometry/areasvols.htm and surface area of ellipsoid body of rotation volume, http://www.math.ucla.edu/~ronmiech/Calculus_Problems/32A/chap9/section3/564d27/564_27.html

13 Advanced Orientation Systems Inc. EZ Compass system, http://www.aositilt.com/#COMPASS

14 Analog Devices ADXL202E Dual Axis ±2 g Accelerometer, http://products.analog.com/products/info.asp?product=ADXL202

15 Analog Devices ADXRS150 +150 deg/sec Single Chip Yaw Rate Gyro, with Signal Conditioning, Preliminary Analog Devices Confidential data sheet (available upon request from Analog Devices).

16 Entran Subminiature Probes, http://www.entran.com/ptoc.htm

17 "MEMS Velocimeter", DARPA MTO MEMS PI Meeting, 8,9 Feb 2001, Berkeley CA, PI Dr. Mory Gharib, Co-Is: Darius, Modarress, Dan Wilson, Frederic Taugwalder, Dominique Fourquette; in cooperation with JPL, Viosense Corporation. http://www.viosense.com

18 T. McTrusty, W. Divine, "Large Scale Vehicle (LSV) Acoustic Tracking and Communication System (ATACS)", Naval Coastal Systems Center, 1988

19 Dual-Use Signal Processor and Integrated Sensor Computing for μAUV, Todd M. Massengill, and Denise M. Wilson, University of Washington, dated 19 April 2001

20 Sandia National Lab MEMS Introductory Short Course Notes dated Nov 9, 2000

21 CMOS-MEMS Design for the Application-Specific MEMS Process Service (ASIMPS) Course Notes dated March 26-27, 2001

22 Sandia National Lab MEMS Reliability Short Course Notes dated Nov 16 2000

23 Valence Technology, Inc., Lithium Ion Battery Products, http://www.valence.com/products/Series25/25MDL_1.htm

24 Telcordia Plion flexible battery system, http://www.telcordia.com/research/whatwedo/products/plion.html

25 Nasa Electro Active Polymer technology links page, http://ndeaa.jpl.nasa.gov/nasa-nde/lommas/eap/EAP-web.htm

26 Phoncon with Dr. Pramode Bandyobaphyay, 5/11/2001, ONR, 703, 696-3163

27 Koford Planetary Gearheads, 308:1, http://www.koford.com/encoders.pdf

28 MicroMo's Coreless DC Motor Model 3042, http://209.207.212.142/detail.asp?Pk_product_id=139

Bibliography

Abbott, Ira H., and Von Doenhoff, Albert E., *Theory of Wing Sections, Including a Summary of Airfoil Data*, Cover Publications Inc, NY NY, 1959
Discussions on Drag Coefficients and Shape Implications to Coefficients. Prolific tabulated coefficient data on various shapes.

ANSI/NISO Z39.18-1995, "Scientific and Technical Reports – Elements, Organization, and Design", 1995,
Provides guidance on developing Technical report, including defines elements of report, organization and format.

Bechert, D.W., Bruse, M., Hage, W., Meyer, R. "Fluid Mechanics of Biological Surfaces and their Technological Application", 1st International Symposium on Aqua Bio-Mechanisms, ISABMEC 2000, Sponsored by Tokai University & U.S. Office of Naval Research, NSF, Discussion on Aquatic Fluid Flow on Biological Surfaces and also on the multi-functionality of components of organisms in biology

Curtin, Thomas B., Bellingham, James G., Catipovic, Josko, and Webb, Doug, "Autonomous Ocean Sampling Networks", Oceanography, Vol 6, No. 3 1993
Provides overall system concept for multiple networks of multiple ocean vehicles operating collaboratively to prosecute a survey mission in the undersea environment.

Jones, K.D., Lai, J.C.S., Tuncer, I.H., and Platzer, M.F. "Computational And Experimental Investigation of Flapping Foil Propulsion" 1st International Symposium on Aqua Bio-Mechanisms, ISABMEC 2000, Sponsored by Tokai University & U.S. Office of Naval Research, NSF.
Discussion on flapping foils in fluid medium and thrust and drag and power efficiencies. Predominantly 2D problem prosecution.

Purcell, E. M. Life at Low Reynolds Number, Lyman Laboratory, Harvard University, Cambridge Mass June 1976, http://brodylab.eng.uci.edu/~jpbrody/reynolds/lowpurcell.html
A nice discussion on low reynolds number flow (in the regime of 10-1 and smaller). Not really relevant to this effort at the scale that MicroAUV is approaching. Would be relevant if we could design a MicroAUV all in one MEMS Microchip.

White, Frank M. *Fluid Mechanics*, McGraw-Hill, 1979,
Graduate Level text on Fluid Mechanics at gross scale, including considerable discussion on Coefficient of skin friction and form drag for bodies in a fluid.

AUSI, Minutes of 10th International Symposium on Unmanned Untethered Submersible Technology, 1997
Various papers on underwater vehicles and underwater vehicle technologies. Relevant to developing general understanding of current UUV systems and control methodologies for UUVs

Bureau of Naval Personnel, *Principles of Naval Engineering*, revised, 1970,
Introduction to theory and design of Naval Engineering machinery and systems, provided some background to hull design.

Harmouth, Henning F. *Acoustic Imaging with Electronic Circuits.* New York: Academic Press, 1979.
A discussion of the formation of acoustic images by the utilization of electronic spatial filter arrays.

Malvino, Albert Paul, Phd. *Digital Computer Electronics.* New York: McGraw-Hill, 1977.
An introduction to computers and microprocessors with emphasis on logic design, digital devices, bus structure, computer architecture, and microprogramming.

Paul, Phillip H., Arnold, Don W., and Rakestraw, David J., Electrokinetic Generation of High Pressures using Porous MicroStructures. Sandia National Laboratory
Discusses MEMS based micropore pump, operating at 1000 to 7000 vdc to pump liquids through porous microtubes at very high rates. Examined applicability to MicroAUV, which failed due to high voltage requirement.

Passafiume, John F. and Douglas, Michael. *Digital Logic Design.* New York: John Wiley and Sons, 1985.
An introduction to the fundamentals of digital logic design and circuitry with exercises in logic gates, truth tables, expression reduction, multiplexers, decoders, adders, flip-flops, counters, and registers.

Sandberg, W.C., Ramamurti, R. Westneat, M.M. and Walker, J.A. "3-D Unsteady Computations on Flapping Aquatic Flight" 1st International Symposium on Aqua Bio-Mechanisms, ISABMEC 2000, Sponsored by Tokai University & U.S. Office of Naval Research, NSF
Sandberg, W.C., Ramamurti, R. Westneat, M.M. and Walker, J.A. "3-D Computations of Flapping Aquatic Flight", Naval Research Laboratory, April 2001
The above two documents discuss analytical approach to using NRL's FEFLO facility to model unsteady flapping of bird wrasse (a small reef fish) and establishes for the reader an understanding of the FEFLO capability.

Sedra, Adel S., and Smith, Kenneth C. *Microelectronic Circuits Fourth Edition.* New York: Oxford University Press, 1998.
A core textbook in electronic circuits. The objective is to develop an ability to analyze and design electronic circuits, both analog and digital, discrete and integrated. Emphasis is placed on transister circuit design, IC design, and VLSI.

Urick, Robert J. *Principles of Underwater Sound, 3rd Edition.* New York, McGraw-Hill,1983.
An introduction to basic sonar physics, transmission loss, transducer arrays-directivity index, noise background, scattering, reflection, sound generation, the sonar equations, and their practical application to sonar problems

Unmanned Systems Technology Laboratory, Inc.
510 Clearwater Loop #2
Post Falls, ID 83854

USTLAB – 0502-001 MAMO DUSP ICD MAY 2001

μAUV – MEMS Acoustic, MEMS Optical, Dual Use Signal Processor Imaging Subsystem Interface Control Document (MAMO DUSP ICD)

DRAFT

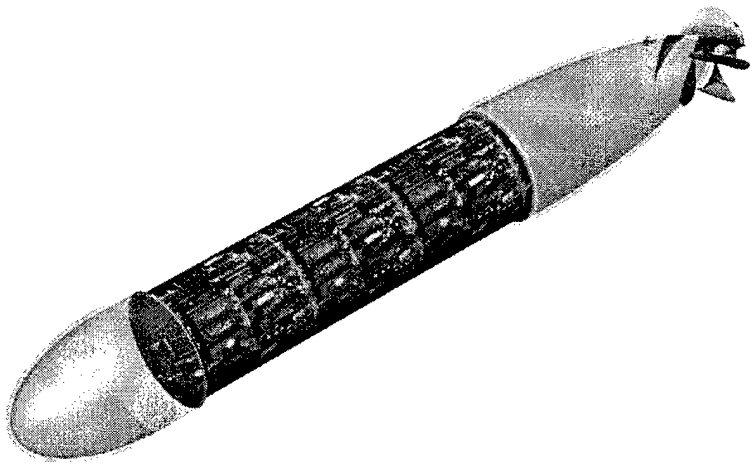

Sponsored by:

Defense Advanced Research Projects Agency
(Micro AUV)
ARPA Order No. K017/19
Issued by DARPA/CMD under contract
#MDA972-01-C-0011

RECORD OF REVISIONS

REV	DATE	PAGE	PARAGRAPH	DESCRIPTION

TABLE OF CONTENTS

1. INTRODUCTION

1.1. PURPOSE

The purpose of this Interface Control Document (ICD) is to define the interface between the sub components of the MicroAUV (μ AUV - Microminiature Autonomous Underwater Vehicle) local environment imaging subsystem. This subsystem includes a MEMS Acoustic (MA) Imaging Sensor, a MEMS Optical (MO) Imaging Sensor and a Dual Use Signal Processor (DUSP). All components are installed onboard the MicroAUV.
This ICD defines functional performances and interfaces to develop the software and hardware to assure compatibility between sub components and full operational capability within the MicroAUV assembly.

1.2. RESPONSIBILITY

Unmanned Systems Technology Lab (USTLAB) and University of Washington (UW) are responsible for the technical design, the implementation, and the demonstration of the hardware and software described herein.

1.3. REFERENCES

1. UW Dual Microcontroller System PowerPoint presentation dated Dec 2000
2. CMOS-MEMS Membrane for Audio-Frequency Acoustic Actuation, John J. Neumann, Jr. and Kaigham J. Gabriel, MEMS Laboratory, Electrical and computer Engineering Department, Carnegie Melon University, Draft Paper not dated.
3. Acoustic Imaging with Electronic Circuits, Henning F. Harmuth, Academic Press, New York, 1979
4. Principles of Underwater Sound, Robert J. Urick, McGraw Hill, New York, 1983
5. Digital Logic Design, John F. Passafiume, Michael Douglas, John Wiley & Sons, New York, 2000
6. Microelectronic Circuits, Fourth Edition, Adel S. Sedra/Kenneth C. Smith, Oxford University Press, New York, 1998
7. CMOS-MEMS Design Course Notes for Application-Specific MEMS Process Service (ASIMPS), dated 26 March 2001
8. Sandia National Lab, Short Course Notes, Introductory, Reliability, Advanced, Nov 2000 – Feb 2001

1.4. FUNCTIONAL SUMMARY OF THE DUAL USE SIGNAL PROCESSING (DUSP) PROGRAMMABLE SYSTEM ON A CHIP (PSOC) INTERFACE

The MicroAUV obstacle avoidance system is a combination of one MEMS (Micro Electrical Mechanical System) Acoustic and one MEMS Optical (MAMO) imaging sensor, and a Dual Use Signal Processing (DUSP) Programmable System On a Chip (PSOC). The MA transducer array and the MO sensor array are MEMS designs and each have similar array dimensions to facilitate processing by a single low power, "simplified operation set", DUSP.
Ultimately, the acoustic and optic transducers will be 32X32 arrays. Initial prototyping of the acoustic sensor will be done as an 8X8 array to use an existing Carnegie Melon University and Darpa sponsored Application Specific Integrated MEMS Process Service (ASIMPS) to fabricate the prototype MA sensor. USTLAB is designing the acoustic array transducer

portion of the sensor, with UW doing the circuit design to read signals off the sensor. The acoustic array sensor will be prototyped in the June-Sept ASIMPS Alpha-User fabrication run at AMS (Austria Mikro Systeme International AG) in Berlin Germany.

The optical array will be a custom design 32 X 32 pixell array or a commercially available equivalent device. Final device will be proposed by UW.

The microcontroller is being developed by UW and will employ the same image processing regardless of the source of the preprocessed image. The preprocessed image (on the memory map) can be transduced from either the optical or acoustic transducer arrays.

1.5. Functional Summary of the CMOS-MEMS Acoustic Array Sensor

The CMOS-MEMS ASIMPS Accoustic Array Sensor prototype chip is being design to have an 8 X 8 pixel array. Limited availability of space in the ASIMPS Alpha-User group process run and project schedule prevent a larger design. Later fabrication runs will expand the chip size and enlarge the number of elements in the array. Each pixel will be a 400μm X 400 μm capacitive diaphram coated with a piezoelectric layer. The 400μm dimension represents one wavelength at a tuned frequency of 3.75 MHz.

Figure 1: Acoustic CMOS-MEMS Sensor Dimensions

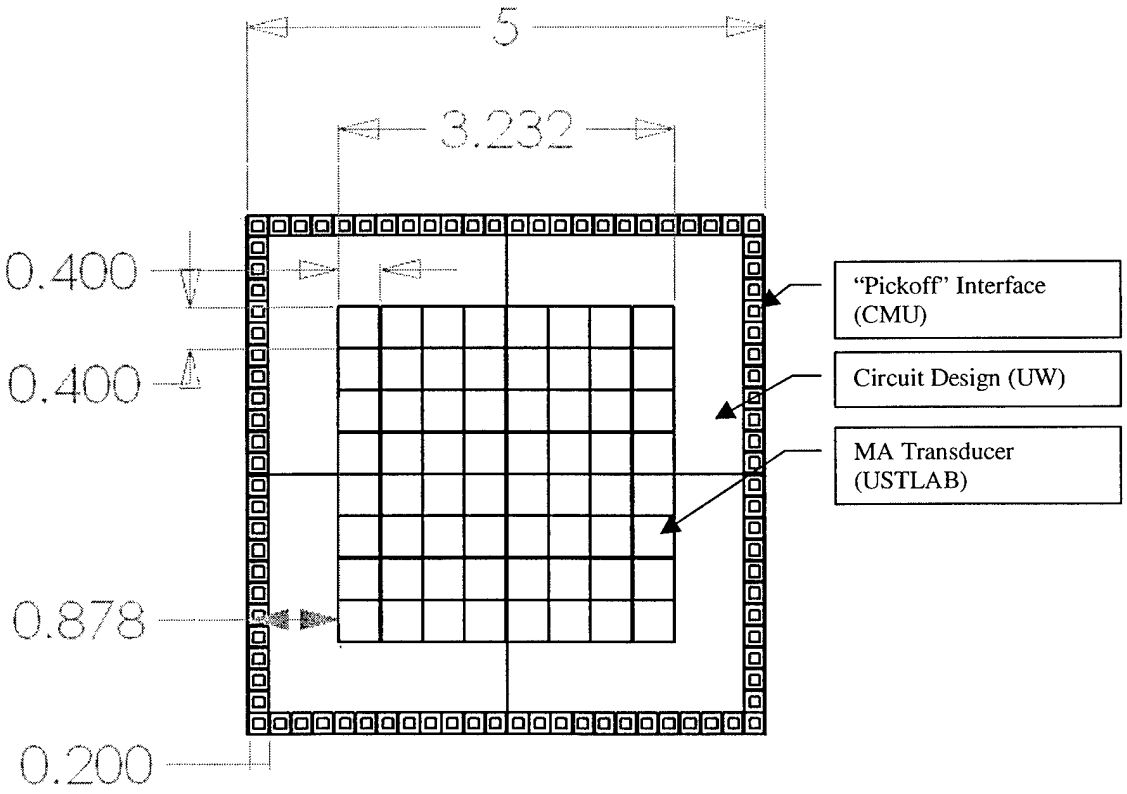

The dimensions of the prototype chip are shown in figrue 1. The chip will be 5mm square with the acoustic array in the center and the surrounding area reserved for on chip A/D conversion and preprocessing circuitry. In the ASIMPS design process, the MEMS device is laid out as an integrated part of the cmos circuitry design. The cmos circuitry is protected by

the metal "3 layer" over that region of the chip when the MEMS device is etched released. The Metal layers are removed over the areas which are to be etched. The diaphram will be composed of a series of metal 1 and 2 springs with the space in between and under etched away. A post process gaseous deposition of either a polymer or a piezoelectric material will fill in the gaps and complete the diaphram. A similar process was demonstrated by CMU for a much larger hearing aid speaker. The metal layers which form the basis for the diaphram will also be the wiring connection to the surrounding circuitry.

1.6. Functional Summary of the CMOS-MEMS Optic Array Sensor

The optical array will be a 32 X 32 pixel array of cmos active pixel photodiodes. Each pixel will be in the range 7-9μ m X 7-9 μm. The chip will include on-chip A/D conversion, 8 bit color or monochrome output, on-chip timing and control (24MHz clock), and microprogram selectable window size, signal gain, exposure parameters, and frame rate selection.

Figure 2: Optical Array Sensor Schematic

TBD

2. BLOCK DIAGRAM DESCRIPTION

2.1. DESCRIPTION OF DUAL USE SIGNAL PROCESSING (DUSP) PROGRAMMABLE SYSTEM ON A CHIP (PSOC) INTERFACE BLOCK DIAGRAM.

Under contract supporting this effort, the University of Washington is developing a Dual Use Signal Processor (DUSP) PSOC that will acquire and process both acoustic and optical data from MEMS sensors. Figure 3, from UW (Dr. Wilson), shows the functional architecture.

Figure 3: UW Low Power Dual Microcontroller DPS System

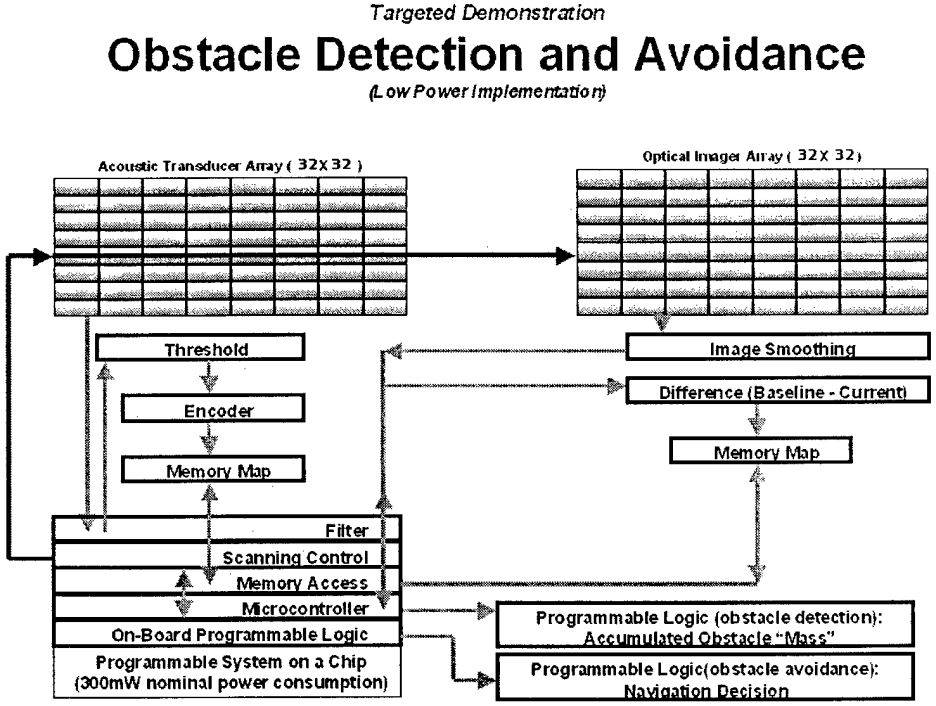

Scanning Control

Scanning control algorithm accumulates sums and differences of image blocks. Controls addressing of both transducer array blocks

Memory Access Microcontroller

Microcontroller controls memory access, and transducer chip processing. All processing from this point forward is independent of the source of the image data (acoustic or optic transducer). Image blocks are accumulated to determine the location of obstacles.

On-Board Programmable Logic

Programmable Logic – obstacle detection

Determine location of obstacles by accumulating obstacle "mass" image.

Programmable Logic – obstacle avoidance

Avoid obstacles by making a navigation decision based on simplified programmed logic algorithm.

~~*Figure 1: Dual Acoustic-Optic Dual Processing System Block Diagram*~~

2.2. Description of Acoustic Image Processing Blocks

Filter: band-pass switched capacitor filters on board Programmable System on a Chip (PSOC). Extract information on acoustic transducer frequency.

Threshold/Comparator: thresholds filtered sonar signal captured in each window in time to binary value.

Encoder: Converts "gated window" sonar information to 8 bit digital word.

Transfer to Memory Map: Transfers 32 X 32 array of 8 bit words indicating time of receipt for sonar signal to RAM for subsequent MicroController processing.

2.3. Description of Optic Image Processing Blocks

Image Smoothing: Spatial low-pass filter that reduces "spot" noise in the optical image.

Difference Logic: Programmable logic or MicroController on-board PSOC extracts difference between current image and baseline image.

Transfer to Memory Map: Transfers 32 X 32 array of 8-bit words indicating monochrome (biased toward "blue" signals), grayscale image values to RAM for subsequent MicroController processing.

2.4. SYSTEM INTERCONNECT

The individual chips will have interface control, A/D, driver circuitry on the chips. The chips will be mounted on flex circuitry for packaging and interconnect with Guidance, Navigation, and Control and other systems. Once mounted directly on the flex circuit and connected to the copper or gold traces by bond wire to bond pad, the whole assembly will be rolled up and coated in urethane or other suitable polymer to provide the rigidity, and packaging (encasement of bond wires and chips). The flex circuit will be formed as part of the hull with the acoustic and optic sensors on the external surface of the bow and encased in polyamide.

MicroSound of Snoqualamie Washington is an example of a commercial vendor producing the foundation technology for this approach. Their niche is prototype flex circuits featuring thin line and multi-layer polyimide film circuits. They are working with industry to provide 1-2 mil polyimide flexible circuits such as Gould®Flex. Their Pyralux® coverlay composite technology can be used to bond layers, encapsulate circuits, in flexible and rigid, or semi rigid multi-layer constructions for both electrical and environmental protection. We propose to take this to the next step of integrated structural/embedded circuit technology.

Figure 4: Eight Layer Flex Circuit (24X24 BGA Array-300μm pitch)

Flex production capabilities

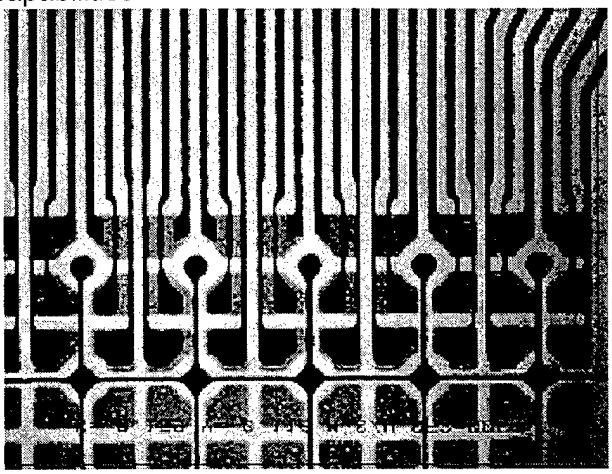

- 50 μm trace/50 μm spacing (with tighter tolerances available for prototypes).
- Multi-layer composite construction
- Copper, gold, immersion tin, and nickel metalization
- Three-four week turn around
- Laminate structures – thin, lightweight, and highly reliable.
- Excellent dimensional stability
- Advanced metallurgy for superior fatigue resistance in dynamic flex applications.
- Chip scale packaging.

3. INTERFACE SPECIFICATIONS

Acoustic Array

Pixel size: 400μm X 400 μm (phase II additional pixel size 362 X 362 and 328 X 328)
Membrane thickness 2 μm
Center Frequency: 3.0 Mhz
Transmit Sound Pressure: 160 dB re 1 μPa
Receive Sensitivity: -44 dB
Beam Angle: 30 degrees

Analog Inputs

Analog Input Channels 1-32
Input Impedance 100 kohms typical
Full Scale Differential Input (Ch+)-(Ch-) 4 Vpp (+/-2V)
Input Signal Range on any Ch+ Ch- 4Vpp max

Analog Dynamic Performance

Amplifier Gain Programmable, 0 to 20 dB typical
Dynamic Range -90 dB typical

A/D Converters

8 bit per channel
Differential amplifier input for low cross talk and noise pickup
Sampling Rate per Channel (fs) - TBD
Full Scale 4Vpp = full scale in 2's complement
Sigma-Delta A/D Oversampling ratio 32 x fs
Digital Filter -3dB Lowpass Frequency 0.478 x fs
Digital Filter -90 dB Bandstop Frequency 0.617 x fs

Environment

Operating Temperature Range 0°C to +40°C.

Optic Array

Pixel size: 7-9 μm X 7-9 μm
Responsivity: 3.0V/Lux-sec
Minimum Light: <5 Lux at 30 fps
Readout Rate: TBD
Frame Rate: 0 – 30 Frames/sec
System Dynamic Range: 50 dB
Programmable gain: 0 – 20 dB
Digital SNR @ 1 Lux: >20 dB
Output: 8 bit color, blue filter
ADC – on-chip
Timing and control – on-chip
Programmable control: TBD

4. TIMING AND CONTROL

4.1. TIMING

The timing clocks provide for A/D timing signals. The timing clk signals include the A/D sample clock, the A/D oversample clock, a pulse per second (pps) clock.

- Fos: A/D Oversample clock. 50% duty cycle. Fos = 32 x sample rate.
- Fs: A/D Sample Rate clock pulse. Logic high pulse during rising edge of Fos. 10 ns minimum set-up time before Fos clock edge and 10 ns minimum hold time. Pulse width is equal to 1 clock period of Fos. Fs must be synchronous to Fos.
- PPS: One pulse per second for optional sync to GPS. The PPS pulse width is equal to 1 clock period of Fos. The PPS pulse must be logic high for the one Fos cycle immediately prior to the Fs rising edge. The PPS pulse provides a method to synchronize sample buffers and time stamp registers through use of GPS, and provides a method to correlate A/D sample times to universal GPS time. 1PPS pulse must be synchonous with Fos and Fs.

4.2. 4.2 TIME STAMP REGISTER

The chip will have a 4-byte time stamp register that increments by one each time a sample for a given channel is transmitted. The processor reads the time tag register and appends the time tag count to the end of the data word payload. The time tag count provides a method to correlate data from different channels. A/D samples from channel 1 with a time tag count=N were sampled at the same time as A/D samples from channel x with the same time tag count=N. The time stamp register is cleared to zero upon power-up, processer reset, a synchronous pulse on the timing PPS clock line, or counter rollover.

4.3. SERIAL CHANNEL CONTROL

A serial channel on each chip is provided for scanning A/D control.

5. FSK ACOUSTIC COMMUNICATIONS

Not within the scope of the initial effort, but planned for phase II will be the expansion of the system into a three acoustic sensor FSK Communication scheme similar to that used on the Large Scale Vehicles (KOKANEE and CUTTHROAT). This design approach is described here as it sets a foundation for the extensibility of the MA transducer array and the DUSP to support growth into this technology area in follow on efforts.
Two additional acoustic sensors tuned to 3.3 MHz and 3.7 MHz will act as FSK filters, and the three acoustic sensors at 3.0 MHz, 3.3 MHz and 3.7 MHz will represent bits in a data word depending on what frequency is transmitted and received. The transmit scheme will consist of 13 pulses representing 13 bits of data. The FSK scheme will be as follows:

FSK pings are synchronized to GPS time and transmit every eight to ten seconds.
FSK signals are processed in with software-based receivers which incorporate leading-edge detection.

FSK signals have 48.6ms duration and are composed of 13 consecutive pulses, each conveying one bit of information. Each pulse is a 3.7ms tone burst having one of three frequencies (3.0, 3.3, and 3.7 MHz).

The first 4 bits will contain a 4-bit ID field and the remaining bits will contain either a data word or command field.

6. POWER REQUIREMENTS

6.1. DUAL MICROCONTROLLER DPS SYSTEM ON A CHIP POWER REQUIREMENTS.

The power requirements for the low power DMS will be 300 mW. This low power will be accomplished by utilization of highly simplified operation set to detect obstacles and make avoidance decisions. Further contributions to power reduction will be realized through the following power management features:

- Full processing power only occurs if the values scanned, filtered, and thresholded from the optical and acoustic transducers have changed from the last scan cycle.
- If no change is detected, the current baseline image is updated for evaluation against future changes.
- Simplified detection/avoidance algorithms are derived from existing successful algorithms in the literature.

Power Requirements

Supply Voltage	+3.3 V
Supply Current	91 mA
Power	300 mW

6.2. ACOUSTIC TRANSDUCER ARRAY POWER REQUIREMENTS

As much circuitry as possible will be integrated on the chip to minimize power consumption.

Power Requirements	
Supply Voltage	+3.3 V
Supply Current	30 mA
Power	99 mW
Bias Voltage	TBD V

6.3. OPTICAL IMAGE TRANSDUCER ARRAY POWER REQUIREMENTS

Power Requirements	
Supply Voltage	+3.3 V
Supply Current	30 mA
Power	99 mW

7. SIGNAL INTERFACES

7.1. ACOUSTIC ARRAY INTERFACE

The acoustic array will be activated by the application of power (Voc),and the

application of the Initiate(INIT) input. After application of power (Voc), a minimum of 5 ms is required before taking the INIT input high. This will allow time for the internal circuitry to be set and the internal oscilator to stabilize.

When INIT is taken high, drive to the transducer array is enabled resulting in thirteen 3.7 ms pulses at 3.0 MHz. The signal will be 4 Vpp (+/-2V) which will excite the elements of the acoustic transducer array. A TBD DC bias voltage will remain on the array elements in between pulses. This bias will be established by a capacitive circuit.

To prevent ringing in the receive circuitry during transmit, a Blanking Inhibit (BINH) will be applied for the 48.1 ms pulse train duration. Following BINH, until a scanned output threshold occurs on any of the array outputs gives the range to an object by the time from INIT going high until the echo is received at a timing rate of 1.3 ms/meter out and back. The ECHO output is an open collector transister latch circuit for each element or multiplexed group of elements. The time between INIT going high and ECHO going high is proportional to the distance to the target. Multiple range slices can be handled by taking a blanking (BLNK) signal high and then back low to reset the latched ECHO output for the next return slice. The array must be scanned at each slice time step.

Figure 4: Acoustic Timing Diagram

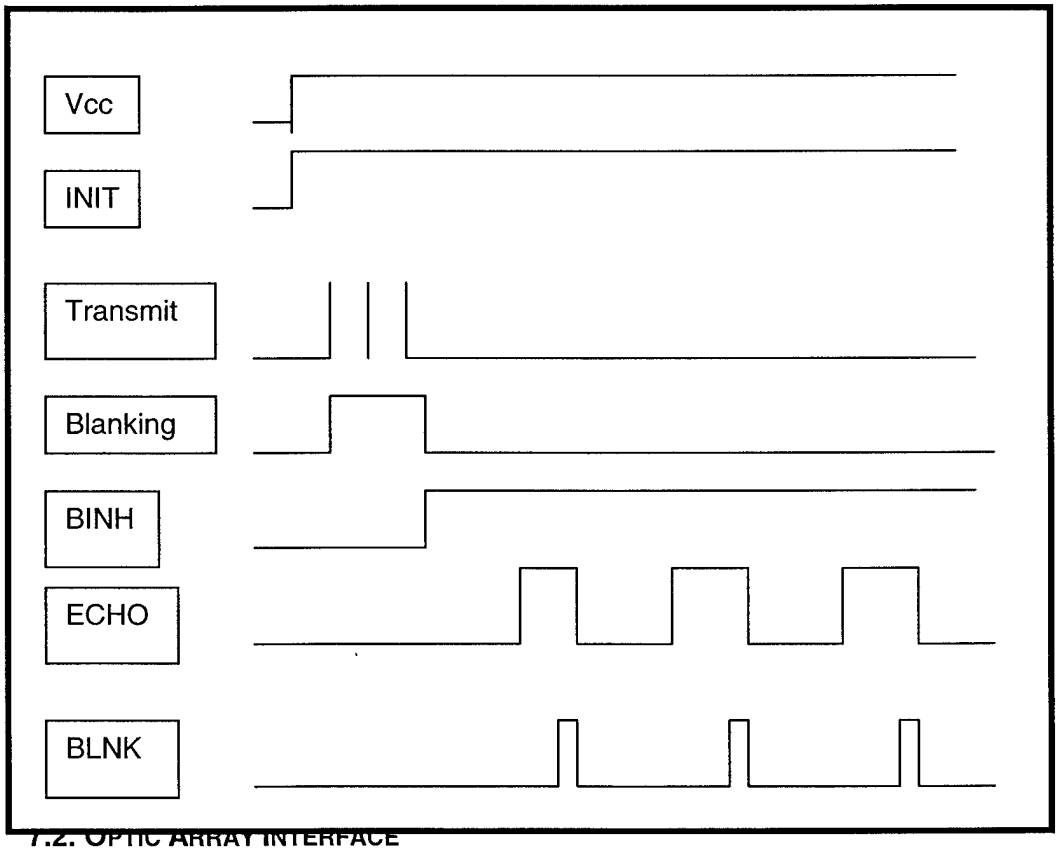

7.2. Optic Array Interface

The application of power (Voc), and the Initiate (INIT) input will activate the optic array. After application of power (Voc), a minimum of 5 ms is required before taking the INIT input high. This will allow time for the internal circuitry to be set. Timing diagram not available yet.

External Signals:	INIT, SYNC, External Clock Input
Output:	8 bit A/D per Channel, Differential Digital Output, TTL compatible
Serial Interface:	Serial Data, Sample Clock, and Scanning Control

USTLABS REPORT FOR APRIL 19, 2001

DUAL-USE SIGNAL PROCESSOR AND INTEGRATED SENSOR COMPUTING FOR MAUV

Todd M. Massengill and Denise M. Wilson
Department of Electrical Engineering
University of Washington
Seattle, Washington 98195-2500 USA
e-mail: toddmass@u.washington.edu; wilson@ee.washington.edu

INTRODUCTION

This report addresses Task One of the subcontract with Unmanned Systems Technology Laboratory: concept design of a dual-use signal processing architecture and integrated sensor computing. The dual-use signal processing architecture is a hardware implementation that serves as object avoidance support for the vehicle guidance system using optical and sonar input arrays interchangeably. Integrated sensor computing uses information from pressure, temperature, and ambient light sensors to adjust gain and clock speeds for optical and sonar image extraction respectively. We address first the construction of the sensor arrays for the acquisition of optical and sonar information. The four-step dual computing architecture that seamlessly processes sonar or optical data, in a fully interchangeable manner, is then described in detail using smooth, segment, detect and avoid algorithms implemented in both analog and digital VLSI architectures. Finally, a description of the integration of pressure, temperature, and ambient light sensors into computing and signal conditioning circuitry is presented.

In this report, we have not addressed explicitly the acquisition of a sonar image in terms of the signal processing that must occur between acquisition of a return pulse and the construction of a useful image for obstacle detection and avoidance. Beamforming, the process used to translate the raw signal data into a sonar image, is a complex process and is currently outside of the scope of our resources and expertise.

EXTRACTION OF SONAR DATA

The CMUT array specified by USTLab consists of 4 chips each with a 4x4 array of transducers combined to create an 8x8 micro scale array operating at 3 MHz. The total targeted beamwidth is 31 degrees. The pulse length will be approximately 16 microseconds resulting in a pulse length of 24 mm (based on the speed of sound at 1,530 m/s). The signals at the 64 elements will be beamformed so that a two dimensional representation of the sonar image is generated. Each 8x8 image represents a slice in space ranging from 10 to 15 meters across (corresponding to the 31 degree beamwidth and a range of 15 to 30 meters from the vehicle). A transformation from the inherently polar nature of the collected data to a cartesian representation takes place. This transformation is often corrected in software to give a correct graphical representation to the user. However, if recognition is not required, such a transformation is not necessarily required.

Another challenge presented by sonar signals is the prevalence of noise. Assuming the system is designed properly, the dominant noise is speckle. A common technique for suppressing noise is Kalman filtering. Kalman filtering is a statistically based recursive algorithm that uses correlation between subsequent images in time (image flow) to filter out random noise (as well as predict obstacle heading or for navigation near the ocean floor).[2][7][8] Kalman filtering is a technique that requires great processing power. It may be sufficient to integrate adjacent images in depth and time to reduce noise so that objects that truly exist remain and scattering effects are minimized. The effectiveness of a particular method is heavily dependent on the spatial frequency (in depth) of the sonar images.

At this stage of the project, we are assuming we have an array corresponding to a beamformed image. The beamforming method remains to be chosen. It is important to note the current state of beamforming has not reached the point where a fully 2-D array can be processed in real-time applications. Fully 2-D is a term that describes a two dimensional array of transducers in which each transducer is controlled and sampled independently. Typically, physically two dimensional arrays are connected along the columns so each row can be controlled independently or relative to one another. These quasi-2D approaches make up the gray area between strictly linear and fully 2-D array beamforming.[9]

Two directions that hold promise for low power obstacle avoidance using forward-looking sonar are low bit-rate image formation from a series of beamformed inputs and use of an acoustic lens to focus incident acoustic reflections onto the sonar transducer array. The process of low bit-rate image formation thresholds amplitude information from a beamformed sonar signal above a certain noise floor then checks for persistence. Thus, beams that contain multiple bits in sequence represent a detected object while beams that have bits interspersed with missing bits represent noise. A similar technique has been proposed by Robert Pietsch of Sonatech Inc.[10] An acoustic lens focuses sound onto the transmit/receive array (much as an optical lens does) performing the function of beamforming.[11] This saves power but adds volume in front of the transducer array.

EXTRACTION OF OPTICAL DATA

Extracting an optical image is the second method used to detect obstacles in the near field of the MAUV's immediate field of view (5 meters or less). The ability to extract an image is highly dependent on the amount of available ambient light. In this application, the major challenges to obtaining a reasonable image data set are visibility and presence or lack of ambient light. Visibility is a function of particulates, depth and time of day and without an active light source, can range from 0 to 5 meters.[1][2] Particulates or noise in the image can be extracted in the first stage of the dual signal processing (smooth), but must be clearly extracted to ensure success in this initial filtering process. For the MAUV application, optical image sensors will receive low to moderate ambient light, rarely approaching an ambient light level that would saturate the sensors. For this reason, we choose two possible options for extracting optical image data in the underwater environment: (a) a commercial imager such as those shown in Table 1 that offers moderate resolution and the lowest possible detection limit (e.g. 0.5 lux for the OV5116 imager from OmniVision) and (b) custom imagers made using the MOSIS integrated circuit fabrication service that again use CMOS for low power but also include larger photosensor areas with higher sensitivity than commercially available imagers. Low detection limits in the sensor itself[3] as well as embedded amplification in photodiode or phototransistor structures enhances visibility using optical and electrical enhancements respectively. Estimates of power and size consumed by these imagers are as follows (includes initial photosensor integration and image extraction/scanning but no signal processing):

- Commercial imager: CMOS 320 X 240 array from OmniVision uses 0.07 W at continuous use and consumes 46.1 mm X 5.4 mm die area, not including required external components.
- Custom imager: CMOS 32 X 32 array uses a maximum of 0.15W at continuous use and consumes no more than 1 cm X 1 cm die area, not including external components

Table 1

Manufacturer	Model	Color/Monochrome	Digital/Analog	Resolution	Power	SNR
OmniVision	OV5116	Monochrome	Analog	320 x 240	70 mW	46 dB
National Semiconductor	LM9617	Monochrome	Digital	648 x 488	90 mW	45 dB
STMicroelectronics	VV5430	Monochrome	Analog	384 x 287	125 mW	46 dB
Photobit	PB-0111	RGB Color	Digital	352 x 288	55 mW	45 dB

The MAUV application is complicated by the fact that visible light in an underwater environment consists mainly of the band between and including blue and green (430 and 560 nm). Most CMOS imagers constructed in silicon are optimally sensitive to wavelengths in the red to infrared region. In order to enhance sensitivity, while maintaining low cost and low power consumption of the silicon-based CMOS imager implementation, we propose to (a) enhance the photosensitive area to increase overall sensitivity (possible because of low required imager resolution) or (b) alter the photosensor structure so that the generation of photocurrent from impinging light occurs at a depth into the photosensitive structure optimally matched to the blue and green wavelengths. This technique, embedded color sensing, has been demonstrated in preliminary form by research efforts at Oak Ridge National Laboratories and still presents several formidable obstacles in signal extraction. In the interests of optimizing the possibility of successful demonstration at a later milestone in this project, we suggest pursuing the construction of the following imagers:

- Commercial imager (2): construct two CMOS arrays capable of random access scanning of the imager to "electronically" alter the image size to user needs and specifications. Both imagers (OmniVision OV5116 and STMicroelectronics VV5430) are chosen for their low power consumption and low dark current (detection limit). These two imagers will be constructed on separate printed circuit boards and tested individually to compare performance. Estimated prototyping cost including testing supplies: $1000.
- Customer imager (1): construct a single CMOS 32X32 array in silicon, lowering the detection limit by increasing photosensor area and embedded amplification. Estimated prototyping cost including testing supplies: $1400.
- Customer imager (2): construct a single CMOS 32X32 array in silicon, enhancing the sensitivity to blue/green wavelengths by adjusting photojunction depth in the semiconductor. Estimated prototyping cost including testing supplies: $1400.

Customer imagers have a minimum of 3 months lead time, not including design, layout, and simulation time. We request sponsor approval of any or all of the above options before proceeding with up to four possible options for extracting optical imager data.

DUAL-USE PROCESSOR

The goal of the processor design is to take inputs from the two systems discussed above: optical and sonar, and use them to make maneuvering decisions. According to the specification for the processor, optical and sonar data should be treated equally by the processor. Optical inputs are acquired using the CMOS imager described in the section Extraction of Optical Data. Sonar inputs are beamformed images described in the section Extraction of Sonar Data. Thus, both types of input are an array of pixels whose values correspond to reflected light in the case of optical arrays and reflected sound in the case of sonar arrays. The proposed processing steps can be summarized as: smooth, segment, detect, and avoid.

Smooth. The reasons for smoothing the optical and sonar arrays are different. In the case of sonar data, the speckle noise can be suppressed by smoothing. The smoothing of optical images is motivated by a problem that arises from the nature of ambient light in an underwater environment and the constraint to the use of ambient light (as opposed to an active light source) for image acquisition. While ambient light is necessary for an image capture device without an active light source, it also produces undesirable effects especially near the water surface. Figure 1 shows an image of a shark and school of fish with an ambient light gradient near the surface. This picture illustrates the problem created by ambient light as objects appear either light, dark or a combination of the two depending on whether they are blocking the ambient light source or reflecting it.

There are many image processing techniques available to deal with the ambient light problem, but most require the use of a power hungry digital signal processor (DSP) with complex algorithms such as digital high pass filters

and fourier transforms for edge detection. One less complex alternative technique is to obtain a baseline image when no objects are in the field of view and subtract the baseline from the image with objects present. This technique is frequently used in underwater applications where the background tends to be relatively simple and consistent.[4] Since this baseline image changes based on the same factors that affect visibility, it would have to be reset periodically. However, if we assume an object does not take up a majority of the field of view in the image, a baseline can be derived from the original image using a low pass filter. To the best of our knowledge, this technique is not currently used. Other methods of dealing with this light gradient near the surface attempt to operate outside the blue/green band but require an active source such as a laser.[6]

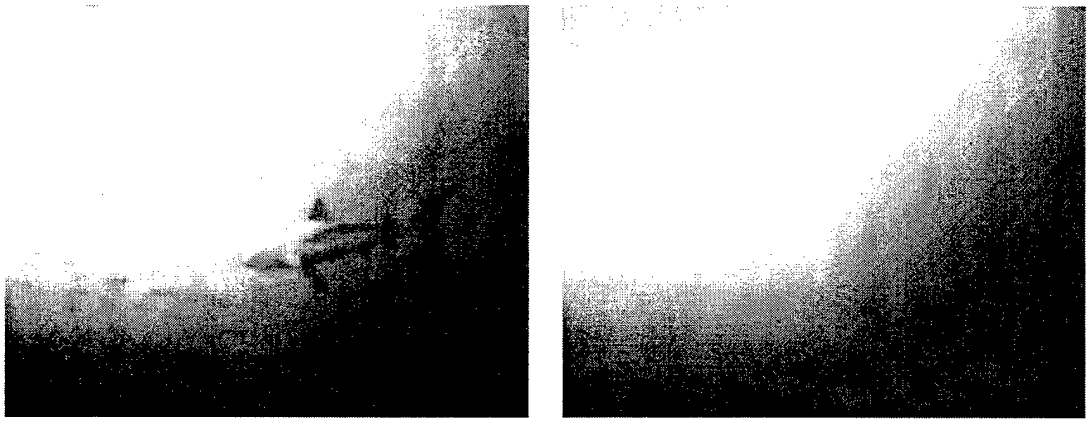

Figure 1

8 bit image of a shark and a school of fish near the surface showing ambient light gradient (left). Same image with an ideal low pass filter applied to approximate the baseline image without objects present (right). The images shown are 330 by 500 pixels and are used for visualization. Actual resolution is anticipated to be 32 by 32 in constructed images.

Smoothing can be achieved with a resistor network implemented using analog circuits and is a model of the human vision system.[5] The resistive network is a passive network that consumes under 25 mW and saves processing time by processing the image in parallel as opposed to a two-dimensional digital filter implemented with a DSP, which uses serial processing. The network is a mathematically complex structure and requires Spice simulation to accurately calculate the power consumption.

In the case of sonar images, the smoothing step involves use of the resistor network discussed above plus thresholding. Figure 2 illustrates each stage of the smoothing step for optical images in the dual-use processor scheme. The first image is the original followed by the baseline image. The baseline image was acquired by simulating the effects of the resistive network. The objects in the image are not completely obscured as they were by using an ideal filter as in the filtered image of Figure 1. Nonetheless, the desired effect is achieved as seen in the next two images. The image generated by subtracting the baseline from the original image is shown in the bottom left of Figure 2 and the bottom right shows the result of thresholding this adjusted image.

Segment. Through the smoothing and thresholding process above, optical and sonar inputs are preprocessed using analog hardware. At this stage, both types of data are in the same form and ready for input into the microcontroller. Depending on the amount of detail desired, it may not be necessary to store the entire array in the microcontroller. The array is thus broken up into segments for each area of interest corresponding to a possible

maneuver. As the values in the array are scanned, they can be summed into bins stored in memory. Figure 3 illustrates a simple case in which the thresholded optical image example is segmented into nine regions of equal size.

Detect. The nine values obtained from the segmentation step are stored in memory on the microcontroller. These values can be considered to be a measure of how substantial an obstacle exists in each region or of the probability that an obstacle exists in each region. The results from the simulation shark image are summarized in Table 2 beside Figure 3. It is clear in this example, that a maneuver to the left or up will provide a clear path. In other images tested, some regions contained misdetected pixels but were at least an order of magnitude lower than the values of sections containing valid objects.

Avoid. The values from the detection step above can be output directly to the central processing unit of the vehicle or an ordered list of suggested maneuvers. If additional details are required by the vehicle's navigation system, it may be necessary to store each pixel into memory in addition to the regional bins as part of the segment step.

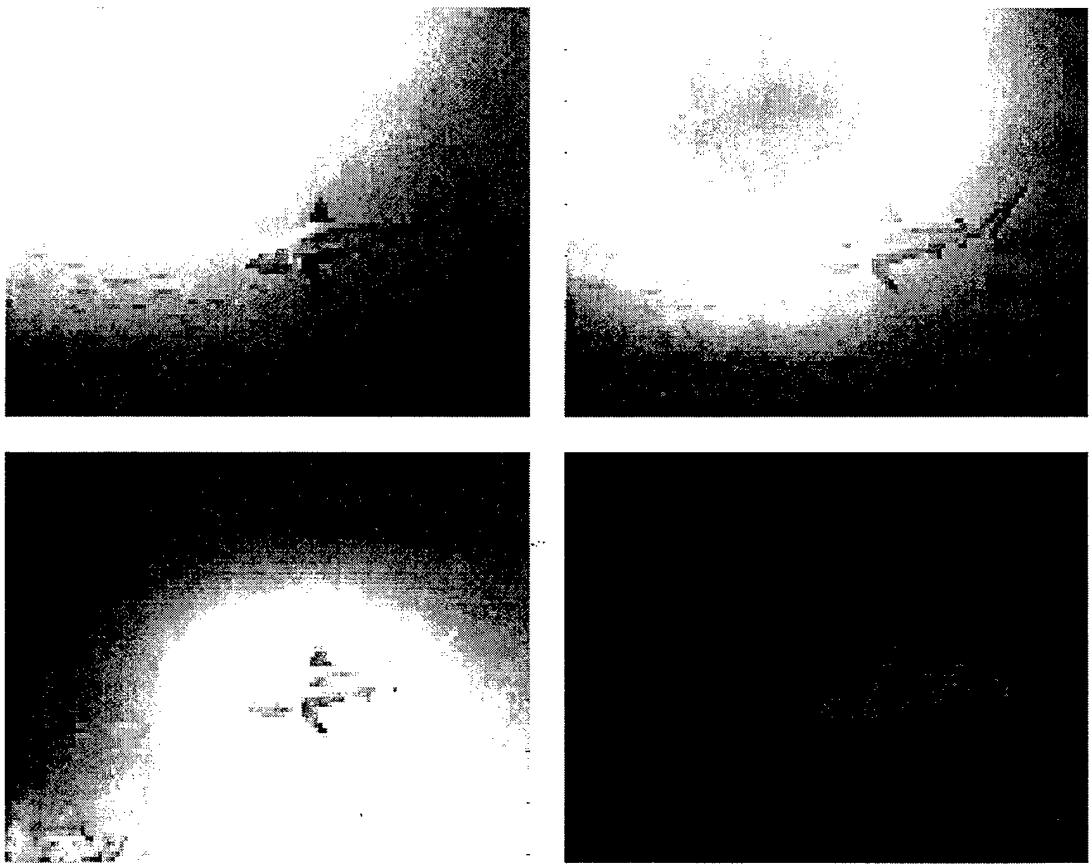

Figure 2

Original image 83 by 125 pixels (top left). Same image smoothed with simulated resistor network resulting in baseline image (top right). Original with baseline subtracted (bottom left). Final thresholded image showing obstacle (bottom right).

The Microchip PIC16F87X microcontroller family is sufficient for this smooth, segment, detect and avoid processing. Various memory and input configurations are available to expand its capabilities if desired. These microcontrollers can be operated at 3 V and 0.6 mA at 4 MHz. Thus, their operating power is 1.8 mW and standby power 3 μW.

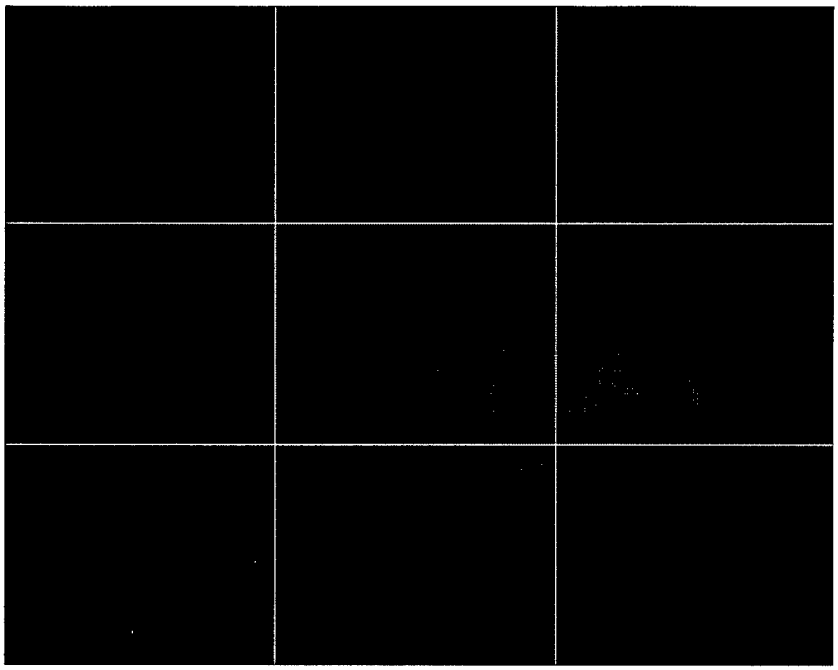

Figure 3

Segmentation of thresholded image to obtain values corresponding to probability an obstacle exists in each region. For this image, the value for each segment are listed in Table 2 below.

Table 2

0	0	0
0	149	42
0	15	0

INTEGRATED SENSOR COMPUTING

The second of two primary goals of this project is to use sensors embedded in the computing of data. Typically, use of sensors follow the following traditional template:

- Sense
- Condition
- Amplify
- Transfer
- Analog to digital convert (ADC)
- System computer

Thus, every sensor in a system is transduced to an electrical signal, conditioned, amplified and transferred to a processing unit as a digital signal. Finally, the system computer performs math on the digital signal to relate it back to the magnitude of the original measurand and this value is used to adjust the relevant system parameters. The very first step in the traditional template is the process of sensing: transducing a changing measurand into a varying circuit parameter such as resistance, capacitance, current or voltage. The integrated sensor computing proposed here seeks to incorporate sensors as circuit elements such that changes in the measurand result in a meaningful response. The traditional sensor template can be replaced by the following two steps:

- Sense

- System computer

In the case of the image preprocessing discussed in the previous section, automatic gain control is desirable given the variance in visibility. Thus, a light sensor can be used to adjust the integration time of the gain circuitry for the CMOS imager. When this sensor is operating in black current, the imager can be disabled since the ambient light is insufficient to provide good data.

Pressure is an important parameter in underwater applications. At shallow depths, depth can be estimated as a linear function of pressure increasing by roughly 1 atm every 10 meters. Depending on the accuracy desired, depth is a polynomial function of pressure and of latitude due to changes in the gravitational field.[12]. Micromachined pressure transducers are most frequently piezoresistive. A pressure sensor must have an appropriate dynamic range for a shallow water application (0 to 600 feet) where pressure ranges from 15 to 300 psi. The smallest commercial sensor found that has this range and can be sealed for underwater use is the Entran EPI-41 subminiature pressure transducer. Temperature is another important measurement and the two most likely micromachined temperature sensor candidates are a thermistor which transduces temperature into resistance and a PTAT which transduces temperature into voltage. The PTAT style temperature sensor is usually preferable as it has a linear response to temperature. Finally, salinity is a desired quantity to complete the set of CTD measurements used to calculate the speed of sound in water. Many existing salinity sensors are made for environmental survey and are thus not small. The most likely candidate for sensor type is inductive. Because of the inductive measurement, this sensor is not easily miniaturized. The smallest system incorporating the set of three sensors (pressure, temperature, conductivity) we found commercially available that combines these measurements is made by Falmouth Scientific, Inc.[13]

CONCLUSION

The obstacle avoidance algorithm for the MAUV using optical and sonar data interchangeably, relies on a series of signal processing steps to normalize the data: smooth, segment, detect and avoid. The feasibility of this signal processing and avoidance algorithm has been shown using mathematical simulation illustrated in Figures 1 through 3. Primary quantities of interest for integrated computing in an underwater environment are depth and speed of sound. The two most important measurands that affect depth and speed of sound are pressure and temperature. The next step toward development of the integrated sensor computing will involve specifying the resolution requirements of the MAUV's central navigation system. An industry survey of existing sensor and microcontroller technologies was performed with respect to power, size and weight requirements and is summarized in Table 3.

Task Two of the subcontract with Unmanned Systems Technology Laboratory is to develop a demonstrable milestone toward simulation of the concept design for the dual-use processing and integrated sensor computing. This will involve device testing of the CMOS image sensors discussed in the section Extraction of Optical Data and simulation of the resistor network for image smoothing.

Table 3

Responsibility	System Component	Implementation*	Power	Size**	Weight**
UWEE	Pressure Sensor	Piezoresistive Semiconductor	20 mW	2.03 mm dia. x 6.4mm len.	1 g
UWEE	Temperature Sensor	PTAT	10 mW	trivial	trivial
UWEE	Dual Use Signal Processor	Microchip PIC16F87X family (3 volt)	10 mW	28 Pin DIP 40 Pin DIP	2.15 g 3 g
UWEE	Optical Imager	320x240 CMOS imager	150 mW	28 pin LCC	15 g
USTLAB	Sonar Imager	CMUT	4.8 mW***	(2x) 40 pin DIP	6 g
UWEE	Optical Infrastructure (Scanning, Integration)	Integrated Mixed-Signal Circuits	190 mW	28 pin DIP	2.15 g
USTLAB	Sonar Infrastructure (Scanning, Beamforming)	Discrete analog circuits	unknown	unknown	unknown

* Continuous Use Does not include less than 100% duty cycle

** Size and weight quantities are listed for the discrete parts listed here. The bulk of size and weight requirements will be in PCB and cabling.

*** Calculation based on 5 cm range. Receiving power should remain constant regardless of range.

REFERENCES

[1] Zhang Rubo, Gu Guochang, Zhang Guoyin, "AUV Obstacle-avoidance Based on Information Fusion of Multi-Sensors", 1997 IEEE Conference on Intelligent Processing Systems, pp. 1381-1384

[2] I. Ruiz, Y. Petillot, D. Lane, J. Bell, "Tracking Objects in Underwater Multibeam Sonar Images", IEE Colloquium on Motion Analysis and Tracking, 1999, pp. 11/1-11/7

[3] L. Calmes, J. Murray, W. Austin, R. Powell, "Marine Raman Image Amplification", Conference on Airborne and In-Water Underwater Imaging, 1999, SPIE vol. 3761, pp. 20-28

[4] Tsung Nan Chou, Catherine Wykes, "An Integrated Vision/Ultrasonic Sensor for 3D Target Recognition And Measurement", IPA '97, pp. 189-193

[5] Carver Mead, Analog VLSI and Neural Systems, Addison-Wesley Publishing Co., 1989, pp. 112-116

[6] P. Ridao, J. Salvi, J. Batlle, "Behaviours Implemented Using a Vision System Based on Coded Light Projection", IEE Colloquium on Motion Analysis and Tracking, 1998, pp. 7/1-7/6

[7] Raymond Suorsa, Banavar Sridhar, "A Parallel Implementation of a Multisensor Feature-Based Range-Estimation Method", Transactions on Robotics and Automation, 1994, vol. 10, no. 6, pp. 755-768

[8] D. Barnett, S. McClaran, E. Nelson, M. McDermott, G. Williams, "Architecture of the Texas A&M Autonomous Underwater Vehicle Controller", Proceedings of the 1996 Symposium on Autonomous Underwater Vehicle Technology, pp. 231-237

[9] Kai Thomenius, "Evolution of Ultrasound Beamformers", IEEE Ultrasonics Symposium, 1996, vol. 2, pp. 1615-1622

[10] Robert Pietsch, "Autonomous Vehicle Obstacle Detection and Tracking", Proceedings of the 1998 International Symposium on Underwater Technology, 1998, pp. 198-202

[11] Edward O. Belcher, "Beamforming and Imaging with Acoustic Lenses in Small, High-Frequency Sonars", Oceans '99, vol. 3, pp. 1495-1499

[12] C. C. Leroy and F Parthiot, "Depth-pressure relationship in the oceans and seas", (1998) J. Acoust. Soc. Am. 103(3) pp 1346-1352

[13] http://www.falmouth.com/products/micro_ctd2/MCTD2.htm

CMOS IMAGE SENSOR

BLACK AND WHITE CMOS IMAGE SENSOR M64285FP

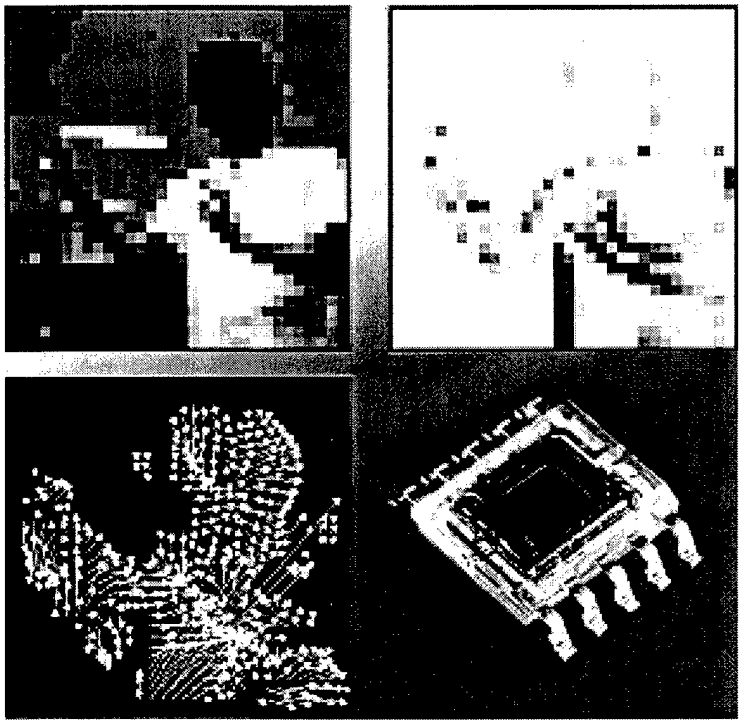

Different component images of a motion estimation algorithm are captured when using a Mitsubishi M64285FP CMOS image sensor.

Introducing the Only 32 x 32 Black and White CMOS Image Sensor with Focal Plane Processing Available Today

The M64285FP is a 32 x 32 pixel CMOS image sensor that is ideal for applications requiring image capture and processing, such as PC interface and motor-detection image-capture systems. Its advanced image information input system is highly functional, small in size, fast in speed, and low in power consumption.

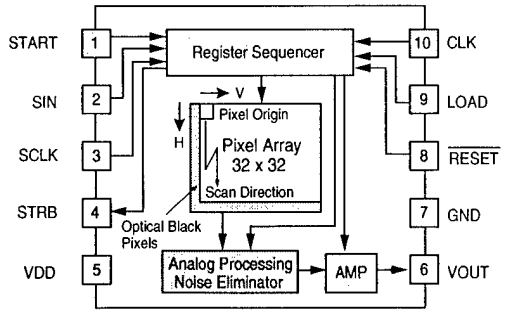

M64285FP Highlights

- Single 5V power supply
- Low power dissipation (15 mW)
- Projection processing of two dimensional (2D) images to one dimensional (1D) images (column and row projection)
- Outputs the average data of the overall image area or the central part
- Edge-extracted image output available
- Adjustable gain, output level, and data offset
- Variable data rate (4 phi to 64 phi per pixel)
- 8-bit microcomputer can be used for control purposes

Applications

- Image Capture System
- Gaming
- PC Interface Systems

Device Structure

- Number of active pixels: 32 x 32
- Image area: 1.79 mm x 1.79 mm (1/6 inch, optical system)
- Pixel size: 56 µm x 56 µm
- High frame rate (maximum 5000 frames per second for projection data)

MITSUBISHI
ELECTRONIC DEVICE GROUP

MITSUBISHI ELECTRONICS AMERICA, INC.
ELECTRONIC DEVICE GROUP

U.S.A. Headquarters

Mitsubishi Electronics America, Inc.
Electronic Device Group
1050 East Arques Avenue
Sunnyvale, CA 94086
Phone: 408-730-5900
FAX: 408-732-9382

DIRECT SALES OFFICES - U.S.A.

Northwest

Mitsubishi Electronics America, Inc.
Electronic Device Group
1050 East Arques Avenue
Sunnyvale, CA 94086
Phone: 408-730-5900
FAX: 408-737-1129

Southwest

Mitsubishi Electronics America, Inc.
Electronic Device Group
20 Fairbanks, Suite 181
Irvine, CA 92618
Phone: 949-859-9457
FAX: 949-859-9450

Rocky Mountain

Mitsubishi Electronics America, Inc.
Electronic Device Group
1113 Spruce Street, Suite 503
Boulder, CO 80302
Phone: 303-546-6300
FAX: 303-546-6242

North Central

Mitsubishi Electronics America, Inc.
Electronic Device Group
9800 Bren Road East, Suite 243
Minneapolis, MN 55343
Phone: 612-938-7779
FAX: 612-938-5125

South Central

Mitsubishi Electronics America, Inc.
Electronic Device Group
1430 Valwood Parkway, Suite 100
Carrollton, TX 75006
Phone: 972-888-2230
FAX: 972-620-6025

Mitsubishi Electronics America, Inc.
Electronic Device Group
8310 Capital of Texas Hwy. N., Suite 260
Austin, TX 78731
Phone: 512-346-4200
FAX: 512-346-4434

Mitsubishi Electronics America, Inc.
Electronic Device Group
20405 SH249, Suite 170
Houston, TX 77070
Phone: 281-320-5959
FAX: 281-320-5960

Northeast

Mitsubishi Electronics America, Inc.
Electronic Device Group
200 Unicorn Park Drive
Woburn, MA 01801
Phone: 781-937-4300
FAX: 781-938-1075

Mitsubishi Electronics America, Inc.
Electronic Device Group
300 Westage Business Center, Suite 355
Fishkill, NY 12524
Phone: 914-896-0896
FAX: 914-896-8639

Mid-Atlantic

Mitsubishi Electronics America, Inc.
Electronic Device Group
374 Millburn Ave., Suite 300E
Millburn, NJ 07041
Phone: 973-921-1300
FAX: 973-921-1314

South Atlantic

Mitsubishi Electronics America, Inc.
Electronic Device Group
2500 Gateway Center Blvd., Suite 500
Morrisville, NC 27560
Phone: 919-460-0404
FAX: 919-460-6205

Southeast

Mitsubishi Electronics America, Inc.
Electronic Device Group
3100 Avalon Ridge Place, Suite 200
Norcross, GA 30071
Phone: 770-613-5852
FAX: 770-662-5208

MEXICO INQUIRIES

Western Mexico

Mitsubishi Electronics America, Inc.
Electronic Device Group
1430 Valwood Parkway, Suite 100
Carrollton, TX 75006
Phone: 972-888-2230
FAX: 972-620-6025

Eastern Mexico

Mitsubishi Electronics America, Inc.
Electronic Device Group
20 Fairbanks, Suite181
Irvine, CA 92618
Phone: 949-859-9457
FAX: 949-859-9450

MITSUBISHI ELECTRIC SALES CANADA, INC.

DIRECT SALES OFFICES - CANADA

Western Canada

Mitsubishi Electric Sales Canada, Inc.
Airway Park Towers
2431 37th Avenue North East, Suite 230
Calgary, Alberta, Canada T2E 6Y7
Phone: 403-291-2100
FAX: 403-291-1563

Central Canada

Mitsubishi Electric Sales Canada, Inc.
4299 14th Avenue
Markham, Ontario, Canada L3R 0J2
Phone: 905-475-7728
FAX: 905-475-1918

Eastern Canada

Mitsubishi Electric Sales Canada, Inc.
340 March Road, Suite 300
Kanata, Ontario, Canada K2K 2E4
Phone: 613-591-3348
FAX: 613-591-3948

Printed in U.S.A.
MPB-ASSP-02-9/99-2K

www.mitsubishichips.com

MITSUBISHI
ELECTRONIC DEVICE GROUP

BIOMIMETIC CONCEPTS TECHNICAL REPORT

Task 1 Deliverable prepared by

Stanley Ross
Marine Physics Corporation
Newton MA 02468

under the terms of a Research Agreement
sponsored by

Unmanned Systems Technology Laboratory, Inc.
510 Clearwater Loop #2
Post Falls ID 83854

under contract to

Defense Advanced Research Projects Agency
Advanced Technology Office

per

ARPA Order No. K017/19
issued by DARPA / CMD under Contract # MDA972-01-C-0011

4 APRIL 2001

1. INTRODUCTION. Marine Physics Corporation (MPC) is pleased to submit this document in support of the MicroAUV platform concept[1], proposed by Unmanned Systems Technology Laboratory as both an approach and a methodology for achieving an order of magnitude improvement in AUV performance through the miniaturization of its onboard electronics. It is believed that such miniaturization will enable an underwater vehicle to be constructed which can demonstrate order-of-magnitude improvement in specific endurance over current state-of-the-art, as expressed in range per pound mass of vehicle. By incorporating MEMS microminiaturization techniques and multifunctional materials into the AUV design, USTL intends both to open up additional space for onboard energy sources, and to reduce overall power budgets

In the present context MPC strives to complement the MicroAUV approach by improving mission endurance still further, here specifically through the microminiaturization of onboard sensors employed for platform navigation. Our approach invokes newly emergent techniques in biomimetics, *viz.* artificially imitating the performance of the natural organs of invertebrate animals and especially in the current regard those which normally live in marine environments. Most natural sensing organs are virtually massless and of insignificant size. Most are also passive in operation, *i.e.* they make use of natural stimuli and cues available in their surroundings. We strive to build all of these characteristics into the designs of the navigation sensors described below. The first step in this process is to understand the principles of operation of natural sensors most relevant to the MicroAUV design, the second step is to tailor the appropriate design principles to the MicroAUV operating environment, and the third step is to implement and test those principles using modern materials and advanced construction techniques, first in the laboratory and then in the field.

Anticipating possible future attempts at implementing by artificial means the sensory organs discussed below, we have included throughout the following sections of this report brief discussions of relevant mechanical, electrical and optical analogs of the natural organs and their components that are cited in the text.

One other important point should be mentioned. By their very nature the navigation systems of underwater organisms operate most effectively when they are completely submerged, often down to considerable depths. Self-contained biological sensors can detect and interpret underwater cues of natural origin. These cues may include information inherent to sunlight that penetrates the water's surface, or contained in the earth's steady-state biomagnetic field, or acoustic signals or various natural and artificial origin, or even chemical odors. Arising within the underwater environment itself these signals are generally free from interference, nor can they easily be jammed by hostile agents. And the sensing organism itself defies detection by aircraft or satellites. Therefore, besides advantages concerned with size, mass and energy economy, the biomimetic approach also carries elements of vehicle safety and stealth, some of which may be applied usefully to a variety of military purposes.

---

[1] DARPA Contract MDA972-01-C-0011

2. SCOPE OF WORK. MPC's overall effort under the present Research Agreement has been organized into three Tasks, the first of which is reported on in this document. Specifically devoted to reviewing documented studies of the functional behavior of underwater animals and their sensing organs, our Task 1 effort has concentrated on conducting analyses and developing sensor concepts for underwater navigation methods that can achieve USTL's Requirement Specification on Heading and/or Position Determination / Tracking Sensor Performance for the Micro AUV concept. The particular concepts we investigated during our Task 1 research effort included methods based on aspects of natural geomagnetism, photooptics, acoustics and chemical detection.

Our investigations indicated that the first two methods are in principle capable of being implemented using current knowledge plus a combination of currently-existing and newly-emerging technologies. On the other hand, after serious consideration we disqualified the latter two approaches from further consideration. The acoustic approach was rejected not because current technology is inadequate to the task of receiving signals, but because a major effort would be required to develop pattern recognition concepts and associated software for identifying location-specific acoustic signatures which are unspecified *a priori*. The chemical detection option was also rejected, in this case because our survey revealed that current and projected state-of-the-art is not mature enough to allow the design -let alone the construction- of a **passive** chemical identifier. We recognize the existence of so-called "electronic noses" in research and commerce, but we found that they also are not well-enough developed for our purposes to support further investigation. Besides that, electronic noses are **active** electronic devices, having considerable size and weight, which would not be appropriate to support MicroAUV's primary goal of increased mission endurance at minimum expenditure of onboard energy.

The remainder of this report is dedicated to discussions of the two remaining topics, *viz.* geomagnetism and optics, both of which appear to be adaptable to our purposes, and also widely demonstrable in terms of the many animal species which have been employing them from time immemorial

3. GEOMAGNETIC SENSING. The earth is, among other things, an enormous magnet. Its magnetic field is essentially a dipole whose behavior is generally attributed to dynamo effects in its fluid outer core. The geomagnetic field, which is relatively static, measures about 0.5 Gauss[2] (50,000 gamma) in the northeastern United States. It is produced primarily within the earth's core, probably by a circulation of the earth's molten interior. The axis of this internal field is only roughly oriented with the planet's axis of rotation. Strictly speaking, the established conventions of physics would locate the geomagnetic north pole in the antarctic region south of Australia, but tradition dictates that the opposite pole, which is located in the

[2] Some time ago the Gauss was replaced by a new unit, the Tesla. The conversion is 1G = 100,000γ = 100,000 nT. As a consequence, 1T= 1V·s/m^2, where 1 nT = 10^{-9} T

Hudson's Bay region of North America, be identified as "north". The magnetic pole is not perfectly stable, but instead wanders slowly, and occasionally -every 10,000-100,000 years- the field reverses itself (the influence of a passing comet?) In the antarctic, magnetic field lines leave the ground going vertically upwards, then curve around to reenter the ground in the arctic going vertically downwards (Fig. 1). The zone where the field lines run parallel to the earth's surface is by common convention referred to as the magnetic equator; it runs north of the geographic equator in Africa and south of it in South America. Thus the magnetic vector points northward/upward in the magnetically southern hemisphere and northward/downward in the northern hemisphere. In contrast to the large and relatively static field generated inside the earth there are much smaller and more dynamic contributions from the ionosphere, whose flow of electrically charged particles, displaced northward and southward each day by solar heating and cooling, creates an inductive field. Solar flares and other disturbances created by sunspots occasionally produce magnetic storms that may distort or even obliterate the usual circadian patterns.

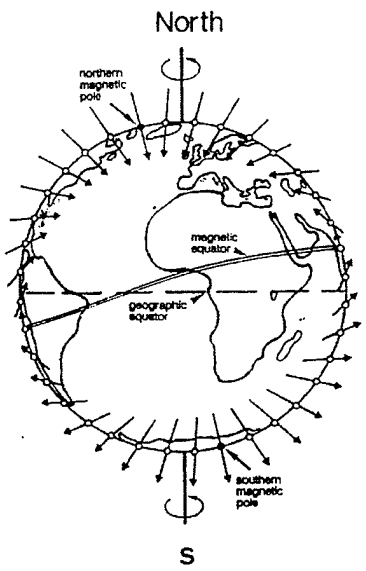

Fig.1 Schematic View of Geomagnetic Field

The magnetic field at a given location is described by its *total intensity* and its direction, which is expressed in terms of *declination* and *inclination.* The declination at any given point[3], indicates the direction in the horizontal by stating the deviation of magnetic north from true north at that particular point. Inclination, or "*dip*", indicates the direction in the vertical in terms of the angle between the magnetic vector and the horizontal plane, a downward dip in the northern hemisphere traditionally designated as positive. Lines of equal inclination form a system of roughly parallel lines comparable to lines of equal geographical latitude.

Another way of describing the magnetic field is in terms of Cartesian coordinates; indeed Figs. 2 and 3 illustrate the distribution of isolines in terms of x- , y- and z-coordinates. An important point to note from these Figures is that at sea the magnetic field tends to be much less irregular than on land. The process of seafloor spreading leads to series of extended, linear magnetic hills and valleys running parallel to the mid-oceanic ridges on both sides, thereby forming fairly regular, linear patterns of magnetic topography in large parts of the oceans. This regularity obviously facilitates underwater magnetic navigation in the world's oceans. Especially in the Atlantic, the linear contours tend to align themselves along a north-south axis.

Finally, we make mention of several temporal variations in the magnetic field which occur at three scales of time (1) daily variations and magnetic storms, (2) secular variations, and (3) variations in geologic time. The third effect may be ignored for present purposes. The second can probably be ignored as well, but if

[3] sometimes designated in aeronautical charts as the "variation"

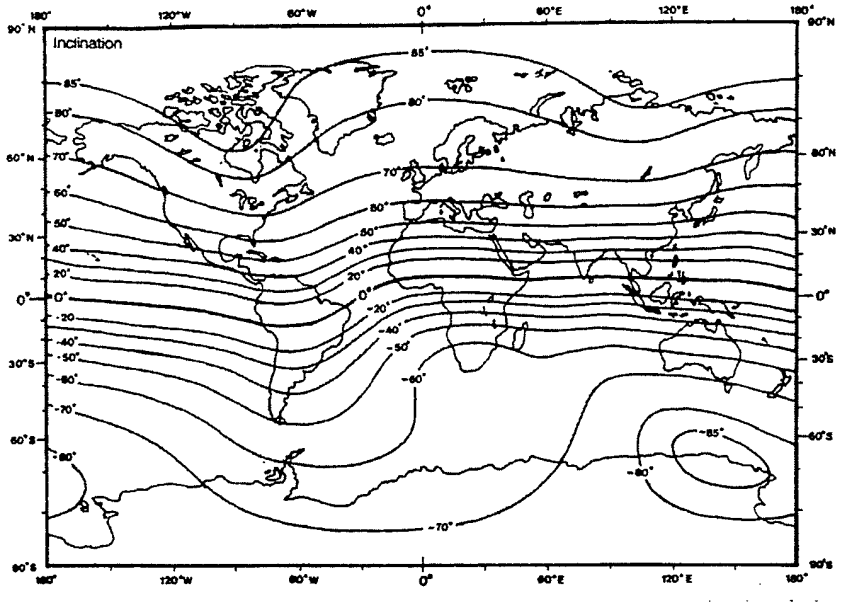

Fig. 2. "Dip" of the Earth's Magnetic Field in Cartesian Coordinates. Negative Signs Show Upward Inclination

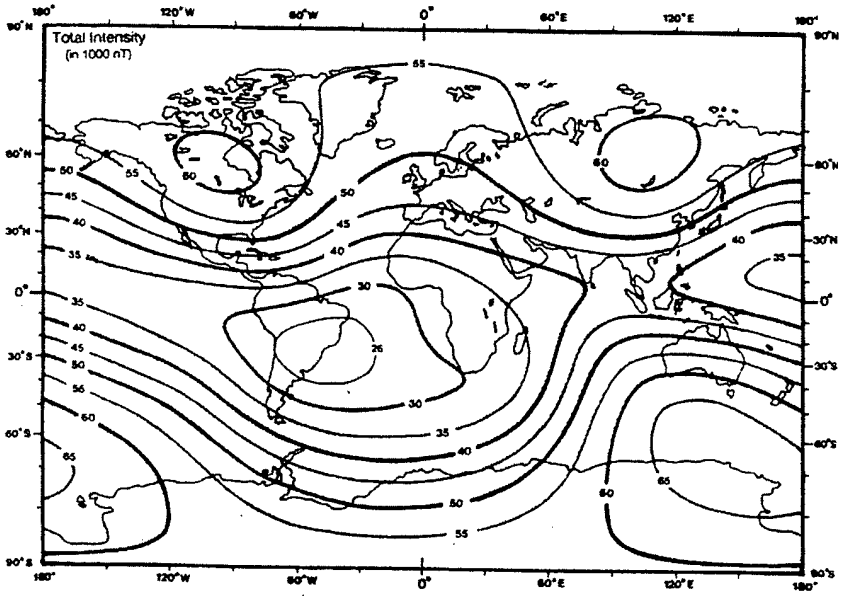

Fig. 3. Total Intensity of the Earth's Magnetic Field, in 1000s of nT.

necessary it can be summarized in tables stored on the onboard navigation computer...perhaps even downloaded as needed. Regular daily variations are caused by the solar electromagnetic variation acting on the sunlit side of the earth; they form complex patterns over the various continents which change with latitude, season and to a lesser extent with the lunar phase. Most of these effects can also be ignored for present purposes.

Electroreception and Electroreceptive Fish. Electroreception is now regarded as a primitive vertebrate trait, present already in some jawless fishes, the lampreys, which are among the few living representatives of the most ancient of all vertebrates, the Agnatha. The cartilagenous fishes (Chondrichthyes) such as sharks, skates, rays and chimæras (or ratfishes) are all electroreceptive. Their sister group, the huge class of bony fishes (Osteichthyes) also possess the ampullary type of receptor, very likely by common descent; except for one taxon, the neopterygians, whose ancestors lost the electroreceptive ability long ago Electroreception is present in all classes of lower aquatic vertebrates, including fishes and some amphibians, but not at all in terrestrial vertebrates or their aquatic descendants, *viz.* reptiles, birds and mammals. This would seem to reflect the more regular patterns of geomagnetic lines of force found in oceanic areas but not on continental masses. In other words, nature appears to give animals more to work with electrically in the sea than on land, which may have stimulated the evolution of electroreception in the sea but not on land. Electroreceptive lower vertebrates have in common the following physical characteristics: (1) specific sensory organs with electroreceptor cells of the common, i.e. ampullary, kind embedded in the skin; and (2) afferent nerve fibers connecting to (3) specialized brain ganglia, nuclei or laminæ, and specific fiber tracts to higher brain areas.

Some teleosts, specifically electrogenic Mormyroidei and Gymnotiformes, and perhaps also Siluriformes, -the latter based on a finding in a single species only- have a second kind of electroreceptor, the tuberous organ which is more commonly associated with the active generation of electrical signals, either for stunning prey or for communication. Since the present discussion concerns itself solely with geomagnetic navigation we shall ignore the tuberous organ and concentrate only on the ampullary.

Ampullary Organs as Signal Transduction Sites. Lorenzinian ampullæ are the sites for the transduction of geomagnetic signals into electrical (neuronal). These organs form a system of sensors, each of which consists of a jelly-filled canal that at one end opens to the skin surface through a pore, and at the other end terminates blindly in a cluster of small swellings lined by the sensory epithelium, *viz.* the ampullæ themselves (Figs. 4 and 5). A bundle of (usually 5-12) afferent nerve fibers innervates each ampulla. The ampullæ are mostly clustered into groups, with many of the groups enclosed in tight connective-tissue capsules. The lengths of the canals vary from one species to the next, and even within a single fish, but the pattern of distribution is more-or-less species specific. For instance, in a medium-sized ray

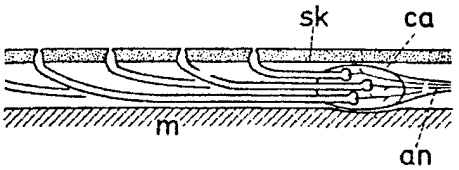

Fig. 4 Ampullary Canals

e.g. 400 mm span, the largest canal might be 160 m in length and 2 mm in diameter. The details of the ampullary swellings also vary among different species.

Accessory structures to the ampullary system include canals, jellies and capsules. The basic principle of operation is that the potential difference across the receptor epithelium depends on the steepness of the voltage gradient in the water, multiplied by the length of the canal in the direction of the gradient. So for panoramic coverage the fish needs to have canals that radiate in all directions, which indeed is the case. Figs. 6 and 7 offer some graphical insight into aspects of the ampullary anatomy which support this feature. They present dorsal and ventral views of the canal system in (respectively) the ray, *Raja clavata*, and in *Scyliorhynus canicula*. Canal openings are shown as dots, and capsules by open circles. As the canals cover most of the surface of the head, diverging in all directions from the encapsulated groups of ampullæ, the ensemble likely provides the fish with information about the strength and configuration of the surrounding electric field. Also, it is probably advantageous to have canals of several lengths, the longer canals responding to slowly-changing stimuli of low intensity and the shorter canals best able to detect brief transient stimuli.

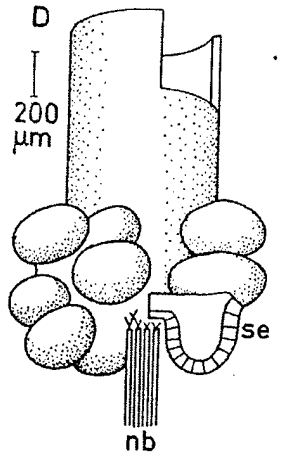

Fig. 5. Ampullary Cluster

Ampullary receptors achieve microvolt levels of electrical sensitivity, which is truly astonishing, when compared with the relatively crude hundred-millivolt-level sensitivity of other well-known synapses such as the second- to-third order giant synapse in squid. Besides extremely high levels of sensitivity, another way in

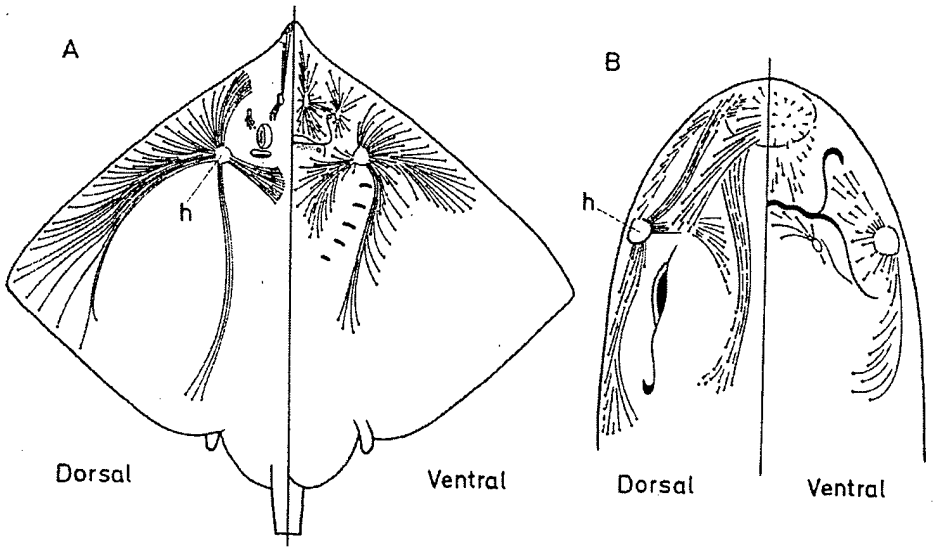

Figs. 6 and 7. Distributions of Ampullary Canals in Rays and Fishes

which the ampullæ are unusual is that the polarity of the responses is opposite to that of other electroreceptors. Only in the ampullæ does a cathode above the receptor mechanism excite, and this is the polarity, which would by itself result in hyperpolarization of the membrane at the base of the receptor cells. So whatever mechanism accounts for the greater sensitivity should also account for this unusual reversal. The existence of such an amplifying and phase-reversing system in the receptor cell provides an apparently satisfactory explanation for the observed phenomenon of "overstimulation". Stimuli one hundred or more times greater than that threshold applied to a canal opening result in *decreased* or even reversed responses, which can now be seen to be the result of the stimulus affecting the basal membrane directly, overriding the electrotonic spread from the completely depolarized or hyperpolarized distal face.

Finally, the receptor mechanisms in fish incorporate considerable smoothing and adaptation, so that very brief pulses and maintained potentials are both relatively ineffective. This behavior appears to be well-suited to underwater navigation by exploiting the geomagnetic field, which changes quite gradually as the fish cuts through the lines of force. However the level of precision -and therefore usefulness- of electroreception as a means of navigation still remains to be established.

Does Downward Flow of Magfield Lines cause transit Flux Field in horiz travel

Principles of Underwater Geomagnetic Navigation. There are three general categories of information provided by the earth's magnetic field which an animal or a robot might put to use in underwater navigation. The first and most obvious is direction (heading). For example, the field lines in the northern hemisphere point roughly northward and downward, important navigational information especially when more obvious optical cues such as the sun, the stars and familiar landmarks are obscured. The precision of such a compass is limited by two factors, viz. the declination -discrepancy between true north and magnetic north- and the sensitivity of the compass sense. The declination is regularly on the order of 5-15°in the northeastern United States and it can be much larger elsewhere. For roughly the same 5°accuracy from a biological magnetic compass, a sensitivity of about 1500 gamma would be required, *viz.* about 3% of the total field.

The second kind of information the earth's field offers is magnetic latitude. Animals and robots both need to know where they are. Magnetic latitude could be determined from total intensity, vertical intensity, horizontal intensity or dip angle, but it would most likely be useful only for determining latitude relative to some well-known reference point. Even then, any determination would have to depend on measuring local gradients at the reference point and extrapolating them to the world at large. Systematic errors would be expected, reflecting the degree to which the gradients near the reference point differ from the regional pattern. Determining magnetic latitude with an accuracy of, say, 10 km would require a sensitivity of 30-100 gamma, or 0.06-0.2% of the total field., depending on which component is used for the measurement. Obviously, accurate determination of latitude during a severe magnetic storm would be all but impossible.

will do you sure

The third kind of information is time. Although animals do not have accurate internal clocks, this is no problem at all for a robotic platform.

Consider now a fish, *e.g.* a shark, swimming in a stationary ocean , as in Fig. 8. As it cruises with velocity **V** through the earth's magnetic field **B**, then a voltage gradient $\mathbf{V} \times \mathbf{B}$ is induced in the fish. As a result, electric loop currents circulate through the fish and the water surrounding it, causing ohmic voltage gradients $-\rho\mathbf{J}$ to develop along their paths. Accordingly, the motional electric field of the shark measured

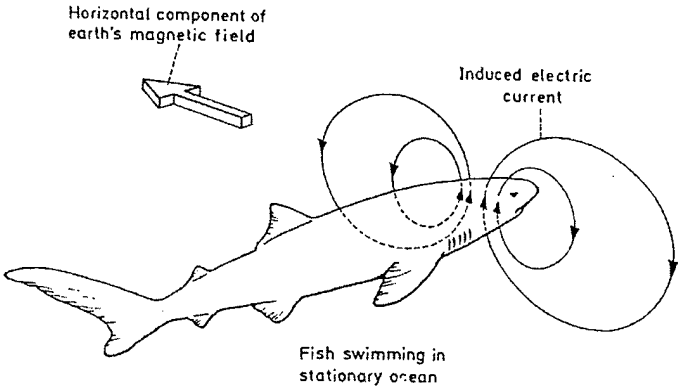

Fig. 8. Geomagnetic Loop Currents Induced within the Body of a Swimming Shark.

with reference to a stationary observer, is given by $\nabla\varphi = \mathbf{V} \times \mathbf{B} - \rho\mathbf{J}$. The seawater, having large volume and low resistivity, practically short-circuits the shark's motional electric field. In the shark's skin and body tissues, the *average* ohmic voltage gradient $-\rho\mathbf{J}$ largely counteracts the induced voltage gradient $\mathbf{V} \times \mathbf{B}$, and so the motional electric field $\nabla\varphi$ is insignificantly weak. However, the high-resistance electroreceptors moving with the shark do not measure the motional electric field $\nabla\varphi$; rather they detect the *average ohmic voltage gradient* $-\rho\mathbf{J}$, which approximates $-\mathbf{V} \times \mathbf{B}$ in the heavily loaded animal.

Fig. 9 illustrates the interaction between a shark swimming in a horizontal circle and the horizontal component of the earth's magnetic field $\mathbf{B}_h$, which plays the most important role in active electro-orientation. The induced voltage gradient $\mathbf{V} \times \mathbf{B}_h$ is ventro-dorsally directed. Since $\mathbf{V} \times \mathbf{B}_h$ is opposed by the ohmic voltage gradient $-\rho\mathbf{J}$, the potential difference φ_{DV} between the animal's dorsal (D) and ventral (V) surfaces is equal to

$$\varphi_{DV} = \int_V^D (\mathbf{V} \times \mathbf{B}_h - \rho\mathbf{J}) \cdot d\mathbf{S}$$

with S representing any ventro-dorsal path through the body tissues. As a result of the seawater loading

$$\int_v^D \rho J \cdot ds \quad \cong \quad \int_v^D (v \times B_h) \cdot ds$$

and φ_{DV} tends to zero.

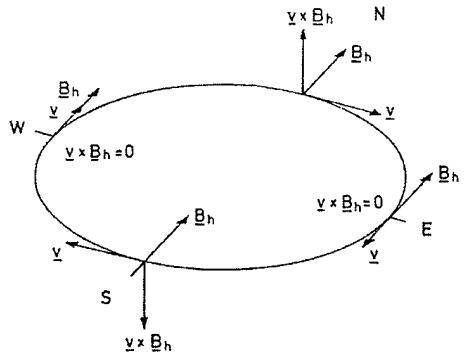

Fig. 9. Forces Induced during Circular Motion

Relative to the overall resistivity of the shark's body tissues, the wall of the ampullary electroreceptor offers an extremely high resistance and virtually no current flows through its jelly-filled canal. Essentially, therefore, it functions is a voltmeter. On the other hand the jelly is almost as conductive as seawater, and therefore the ohmic voltage drop in the ampullary canals must be negligibly weak. Accordingly, the buildup of electrical potential along the two ampullary canals shown in Fig. 10 equals

$$\int_{pore1}^{amp1} (v \times B_h) \cdot ds_1 \quad + \quad \int_{amp2}^{pore2} (v \times B_h) \cdot ds_2$$

Since the dorsal and ventral skin pores are nearly equipotential, the greater part of the potential buildup along the ampullary canals develops across the sensory epithelia that line the terminal ampule of the electroreceptors. In this way, $\mathbf{V \times B_h}$ may be detected by the shark.

The shark can easily recognize the information inherent in the electric field produced by its motion. Specifically, through interaction with the horizontal component of the geomagnetic field, the dorsal ampullae become **positive** with respect to the ventral ampullae when the shark swims *westwards* , and **negative** when the shark swims *eastwards*. No potential differences are induced when the shark swims either *northwards* or *southwards, i.e.* parallel to the magnetic field lines. If the shark, -or even more relevant, the robotic navigation system- can evaluate these differences in electrical potential, they can serve as the basis of a geographical compass.

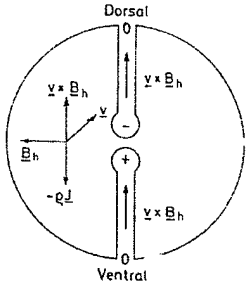

Fig. 10 Electric Field Detection

Interaction between the shark and the **vertical** component of the earth's magnetic field $\mathbf{B_v}$ induces similar potential differences in the horizontally-directed ampullary canals. With this additional information the shark might sense the inclination of the earth's magnetic field and hence the latitude of its position on the globe.

If sensitive enough, a swimming shark or a moving robot can utilize the electric fields generated by its own motion to sense its instantaneous compass heading. For example, when cruising at a modest speed of

100cm/sec $\approx$ 2 mi/hr, the vertical component of induced voltage gradient may be as high as 0.4 μV/cm, which is well within the shark's sensitivity range. Just how sensitive are marine animals to electric fields? Sharks and rays are known to show unconditioned cardiac responses to uniform fields of voltage gradients as low as 0.10 μV/cm. Therefore motional electric fields may be used by them -or by a robot equipped with suitable sensors- not only to seek out currents that afford energy-free transportation during long trips, but also to compensate for drift, or even to serve as a basis for measuring its instantaneous orientation. Even greater sensitivity to very weak electric fields has been exhibited by the American eel, *Anguilla rostrata* which, after accommodating itself to salt water at a concentration level of 40 ohm·cm, exhibited heartbeat decelerations when tested with DC voltage gradients as low as 0.067 μV/cm.

Although in theory seawater currents may be detected by their own motional electric fields, even the simplified case of a uniform surface stream in an otherwise stationary ocean presents its own complications. For example, an animal/robot in the stationary water lateral to or under the stream is subject to motional electric fields, even though neither it nor the water around it are moving. Actually, ocean streams are seldom uniform and the loading by the environment may vary along their course. Furthermore, surface gravity waves may render the top layers of oceans electrically quite noisy, and other electrical fields may compete with the motional electrical fields of oceanic streams.

It should be mentioned that the *vertical* component of the earth's magnetic field produces the electric fields detectable by marine animals. Nevertheless the voltage gradients induced by surface streams crossing the *horizontal* component of the geomagnetic field are *vertically* directed and, due to the character of the air-water interface, they are not sufficiently short-circuited to produce appreciable ohmic voltage gradients. Therefore the electrical detection of passive drift in open-ocean streams breaks down towards the magnetic equator, where the earth's magnetic field is horizontal in direction. Nevertheless, we emphasize here that electro-orientation does indeed depend on the horizontal component of the earth's electrical field, and therefore the strongest electrical signals are obtained when swimming near the magnetic equator. To summarize, the strongest electrical signals pertinent to electro-orientation are obtained when traveling near the magnetic equator, while the strongest electrical signals pertinent to the detection of passive drift are found at high magnetic latitudes.

Finally let us mention a fundamental distinction between detecting ohmic gradients produced by electrochemical emf's, and the direct detection of the electrochemical emf's themselves. In the former case the animal/robot senses fields produced by phenomena , which arise at some distance from it, but in the latter case it is in direct contact with the generator, or it may even be part of it. In particular, the latter case applies to instances when an electrosensitive organism moves into a volume of different chemical composition, salinity, oxygen, pH, or temperature. In such cases, its electrosensor may serve not only as a navigation aid, but also as a detector of environmental change.

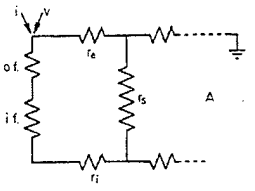

Fig.11. Skin Equivalent Circuit

The anatomical layout of the elasmobranch (marine fish) canal system is well suited to serve an electroreceptive function. The elasmobranch skin has a relatively low resistance and the body tissues are less conductive than seawater, so the voltage gradient extends throughout the body. Under these circumstances the ampullary canals constitute insulated conductors which reach along the electrical gradient and allow voltage comparisons to be made. Fig. 11 has been proposed as an equivalent circuit to represent the electrical properties of the ampullary electroreceptor. Probably it should be augmented by electrical capacitances to provide lateral leakages for high-frequency components of the stimulating current.

An Electrical Cable Analog. Looking ahead towards possible future implementation in terms of artificial devices, the ampullary canal can be represented functionally as a uniform electric waveguide, *viz.* a cable of length ℓ, having a conducting core and a thin surface wall with resistance and capacitance, the cable being immersed within a large volume of conducting medium that is effectively at zero potential everywhere. The transmural flow of potential **V** can then be shown to obey the relationship

$$\lambda^2 \frac{\partial^2 V}{\partial x^2} - \tau_m \frac{dV}{dt} - V = 0$$

where x is the distance along the canal, t is the time, and λ represents a canal space constant expressible as $\sqrt{(aR_m/2R_i)}$, R_i being the resistivity of the core and R_m the mural resistance. At $x = 0$ the canal is terminated by the ampulla, from which the following boundary conditions obtain for all t:

$$\frac{\partial V}{\partial x} = 0 \qquad x = 0$$

Ultimately, the solution for V may be expressed as follows, defining $T = t/\tau_m$

$$V = \frac{E\cosh(x/\lambda)}{\cosh \ell/\lambda} - \frac{4E}{\pi}\sum_{n=0}^{\infty} \frac{(-1)^n e^{-T[1+(2n+\ell)^2]\pi^2\lambda^2/4\ell^2} \cos(2n+1)\pi x/2\ell}{(2n+1)[1+\{2\ell/(2n+1)\pi\lambda\}^2]}$$

where the first term is the steady-state component of the solution and the second term expresses the time course of the response to a voltage step at $x = \ell$.

Exhibiting the characteristics of highly selective low-pass filters, the ampullæ are insensitive even to intense short pulses. They respond to weak electric fields as well as to small changes in salinity of the ambient seawater. In many experiments it has been shown that the strongest responses occur when the voltage gradient of the electric field is parallel to the jelly-filled ampullary canals.

In the laboratory, the most sensitive units, whose canals measure about 2 cm in length, show a 10% frequency change to voltage gradients of 1 μV/cm at a seawater resistivity of approximately 20-22 ohm-cm. A series of unidirectional current pulses spaced 200 ms or less apart was found to be as effective as a dc field of equivalent charge displacement per unit time. The obvious conclusion is that the ampullæ are essentially low-frequency receptors, and as such they are well equipped to detect slow changes in the geomagnetic field vector as the fish/robot moves forward in the water.

Insofar as their ability to detect small changes of salinity in their environment, laboratory tests have shown that seawater concentrations differing as little as 2.5% from normal seawater produced 10% changes in frequency in the afferent nerve fibers of electrosensitive fish, *viz.* transmitting signals *towards* the central nervous system. In fact, other research has reported the ability of isolated organs to detect even a 0.5% variation in seawater content of sodium chloride. In those tests the response time was so short that there was insufficient time for the diffusion of ions down the ampullary tubes, therefore it was concluded that the ampullary sense organ was stimulated by electric currents produced by electrochemical potentials generated across the various interfaces in the ampullary circuitry.

4. SENSING THE DIRECTION OF SOLAR POLARIZATION.

Sunlight Intensity Under Water. The optical properties of natural water bodies restrict underwater visual navigation far more acutely than those of the atmosphere. This is largely because of the much greater absorption and scattering of light that occurs in water. For while horizontal visibility in the atmosphere may extend for many kilometers -over 300 km. in ideally clear air- it is often restricted to 10m or less in turbid coastal zones and about 50m even in clear oceanic water. Correlated with this is the rapid attenuation of daylight with depth. Indeed, even in clear, well-illuminated water volumes the possibilities for using visible landmarks are sharply limited in much the greater part of the sea because both the bottom and the shore are far beyond visible range.

In very shallow depths where the sun's disc may still be visible as such aquatic animals can use it, and perhaps even the moon, for determining compass direction as do many terrestrial animals. Indeed, a sun-compass has been demonstrated by the movements of displaced white bass in a lake, as well as by training experiments with sunfishes in an aquarium. These and other laboratory studies yielded good evidence that the fish's directional sense is regulated by an internal clock mechanism which compensates for the sun's movement through the sky. Some suggestive evidence for a sun-compass among crustaceans has been obtained from observations of the course-holding abilities of swimming prawns after their release out of sight of any landmarks.

Underwater Polarization of Sunlight. In addition to direct effects of the sun's image, the polarization pattern of natural underwater illumination is known to provide a second and probably much more accurate kind of sun-compass, as it does for many terrestrial insects, crustaceans and arachnids. Readily detectable fractions of underwater illumination are known to be linearly polarized in patterns that are systematically related to the sun's position. Not only is this phenomenon present in superficial water layers, but it has also been found to occur down to at least 200m, and it probably extends even deeper under favorable circumstances. The advantage of sensing the polarization angle is that it is much more precisely defined than the solar disc, and so a system of underwater navigation based on the solar polarization angle is in principle capable of yielding greater accuracy in location and heading than the solar position alone can provide.

Polarization, in addition to absorption and scattering, is a manifestation of the interaction of light with matter. Furthermore, since polarization occurs in the processes of reflection and refraction at interfaces, it is not surprising to find that it also arises from the more complicated processes of scattering. Consideration of the scattering of light yields the following formula, first derived by Lord Rayleigh, for the total intensity of light scattered through an angle θ, the azimuth to the solar bearing:

$$p = \frac{1 - \cos^2\theta}{1 + \cos^2\theta} = \frac{\sin^2\theta}{1 + \cos^2\theta}$$

where p, the degree of polarization, is defined as the mean between the amount of light scattered parallel to, and perpendicular to, the plane formed by the incident an scattered portions of the light beam. In general, p is maximal near the surface, decreases rapidly in the first 10-40m, and then diminishes more gently toward some intermediate level. The maximal value of p, the extent of its rapid decrease and the equilibrium value all depend strongly on the turbidity of the water, on the cloud cover , on the proximity of the bottom, and the bottom albedo. Polarization increases rapidly with transparency in turbid or moderately clear waters, but more slowly in extremely clear water. Thus, in water that is quite clear far from the bottom, p may reach 60% or more near the surface, decrease rapidly at greater depths to about 40m, then slowly level off to 30% in deep water. Under such conditions, and with the solar zenith angle i not too small, p is maximal for $\theta = \pm 0°$, less for $\theta = 180°$ and least for $\theta = 0°$. With i smaller, or with greater turbidity, p at $\theta = 180°$ may equal p at $\theta = \pm 90°$; and under extreme conditions of this sort p may not vary with θ at all. The influence of wavelength λ on p is small but definite, with p_{min} occurring at blue or blue-green wavelengths. In fact, both ends of the visible spectrum, particularly the longer wavelengths, polarize more strongly. The amplitude of the effect of λ on p and Δp is small when p is small, but $\Delta p/p$ is relatively constant. Most of these findings -largely experimental- are consistent with the scattering origin of underwater linear polarization. And finally, the degree of polarization decreases when the diffuseness of *underwater* lighting increases; that is, it decreases mainly with cloudiness, with depth , with turbidity, and with the wavelength of greatest penetration.

Anecdotal Evidence for Polarization Sensitivity among Underwater Animals. Discrimination of the plane of polarization is a consequence of the structure of the animal's optic photoreceptors, as we shall discuss presently. Marine creatures whose ability to determine the solar polarization angle has been demonstrated in published reports include: cephalopods (octopus, squid and at least two species of Hawaiian decapods); the freshwater branchiopod *Daphnia magna*; the rainbow trout *Salmo gairdneri*; the freshwater teleost *Dermogenys*; the marine crustacean *Mysidium gracile*; the sockeye salmon *Oncorhyncus nerka*, the Pacific herring *Clupea palasii*; the Japanese crayfish *Procambarus clarkii*, and even the common goldfish, *Carassius auratus*.

When exposed to two horizontal light beams normal to one another, *Daphnia* aggregate predominantly at the brighter of the two. However when one beam is linearly polarized and the other is not, the polarized beam attracts two to three times more *Daphnia* than the non-polarized one. Further, when in the presence of vertical beams of polarized light *Daphnia* will on average orient themselves perpendicularly to the plane of polarization, *viz.* the e-vector. And this seems to be the general rule for other aquatic arthropods as well.

The orientation of the marine crustacean *Mysidium* while swimming in a vertical beam of polarized light seems to depend on an extra-ocular analyzer that functions through the differential scattering of polarized light by the aqueous medium. Like the other aquatic arthropods tested, *Mysidium* demonstrates preferential alignment of its swimming direction perpendicular to the plane of polarization in seawater. However, when the seawater is carefully filtered of suspended matter the swimming directions show less correlation with the plane of vertically-incident polarized light. The *Mysidium* tests also suggested that the predominant clue for orientation is not the polarized direct light itself, but rather the differential intensities of light scattered horizontally in various directions relative to the plane of polarization. In turbid water this intensity shows a strong maximum perpendicular to the plane; on the other hand, although in clear water there would be definite maxima in those directions they would be much less pronounced.

The Invertebrate Compound Eye. The perception of polarized light is a function of the invertebrate compound eye. Insects flying in the air, ants walking on the ground, use their compound eyes to navigate even in overcast weather, and squid swimming in the sea use their compound eyes in the depths of the sea, where the general glare makes light appear to vertebrate eyes to come from all directions. It is a scientific rule of thumb that the larger the eye the sharper the its resolving power ("acuity").

Nature has evolved three different ways of forming an image. (1) The first is a camera-like eye that brings an image into focus on a continuous receptor surface or screen, *viz.* the retina. The human eye works on this principle, as do all other eyes in the vertebrate world. (2) The compound eye is nature's second solution; it is found in invertebrates as diverse as the insect, the crustacean and the mollusc. It is a fixed-focus eye with individual refractive units called ommatidia (Gr. *omma, atos* "eye" + Lat. *-idium,* a diminutive

suffix). Each ommatidium is responsible for a portion of the visual field. The dragonfly, for example, has some 28,000 individual ommatidia, which give it an almost spherical field of view. In the case of the compound eye, lens and cornea are combined, and the light is focused by many small crystalline cones, one for each ommatidium. Fig. 12 presents Swammerdam's original 1737 drawing cutaway view of the honeybee eye, the right-hand portion illustrating the array of corneal lens facets and the left-hand portion illustrating the placement of the ommatidia within the eye socket. (3) The third type of eye is comparatively rare. It scans like a television camera and builds a picture from successive impressions. The smallest known creature capable of forming a visual image is *copilia*, which possesses this third type of eye. This tiny marine copeopod has an eye which is believed to be the link between the primitive photosensitive eyespot and the more complex image-forming eye. Building an image by repeated scans may take anywhere between 0.2 sec to 2.0 seconds, and only then can *copilia*'s brain construct a complete image.

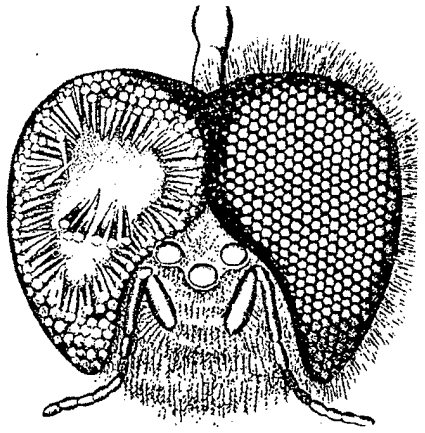

Fig. 1 Head of the honey bee showing the ommatidia of compound eyes according to Swammerdam, *Bijbel der Natu* Leyden 1737.

Fig. 12. Ommatidia within the Honeybee's Head

To resolve light means to discern changes in brightness at microscopic levels, and it has been estimated that a compound eye would have to be at least one meter in diameter in diameter to match the overall resolving power of the human eye. The compound eye is the eye of smaller creatures and does not support distant vision, but its near-field vision characteristics are superb. The insect has no need to see clearly at great distances but it does need to distinguish fine detail close-up. For example, the butterfly *Colias* can distinguish two points separated by as little as 30 microns, while the human eye even at its best cannot distinguish separations of less than 100 microns. To detect the presence of a predator the insect must therefore rely on indirect cues, e.g. a suspicious noise, a sudden shadow, a dangerous odor. The compound eye is a fixed-focus eye and there is no accommodation for near and far vision. That is, if an insect wants to see an object better it must move closer to it. However, it is completely free of both the color distortion and the spherical aberration that plague the larger vertebrate eye. Each lens facet transmits light to its own photoreceptors or those close by, so the eye receives an equally sharp picture from all directions. By contrast the vertebrate eye has high resolution only in the area of greatest photoreceptor concentration, *i.e.* the fovea; the greater the lateral distance from the fovea, the greater the visual aberrations. We are unaware of this because our eyes are constantly shifting, but the area we see clearly at any given time is no larger than the tip of our thumb. If you concentrate your vision on a word in the center of this page you will become aware of the lack of clarity in the area around it.

Components of the Compound Eye. The ommatidia of all compound eyes have the same functional components: the cornea, a crystalline cone, a rhabdom and a more or less complex pigment screen. Fig. 13

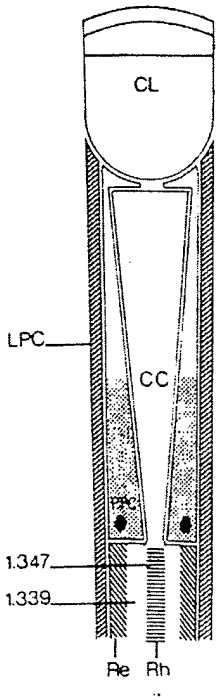

Fig. 13. Bee Ommatidium

displays a cross-section of a single bee ommatidium, illustrating the three components just mentioned. The cornea is a specialized part of the cuticle, which in most invertebrate animals is formed into a grid of corneal lenses. Each ommatidium has its own group of individual photoreceptors, called retinula cells; and the entire group of retinula cells is simply called a retinula. Among insects and higher crustaceans the number of retinula cells per ommatidium is basically eight, although exceptions are common in both groups. Lower crustaceans have fewer retinula cells, -typically five or six; in *Scutigera* and *Limulus* the number varies, commonly between 12-15 in the former, and commonly between 10-13 in the latter. The rhabdom, which is the photosensitive structure, is formed into microvillar extensions of the retinula cells, called rhabdomeres. The way in which rhabdomeres are organized into a rhabdom is a matter of great variation, which depends on the optical type of eye as well as factors that include spectral discrimination and polarization sensitivity.

Most compound eyes have several types of screening pigment cells. The number of these cells, their positions and their pigment content are so variable that a common plan cannot bediscerned. Depending on their position, it is usually possible to define distal, proximal and basal cells, however the terminology is far from consistent. Only a few definable cells are found repeatedly. In insects these are the two primary pigment cells and in the malacostracan crustaceans there are six distal pigment cells, shared by neighboring ommatidia, so that there are twice as many pigment cells as ommatidia. The crustacean ommatidium is also characterized by a pair of corneagenous cells which, although devoid of pigment, show similarities with the primary pigment cells of insects.

Structure of the Compound Eye. It is not intended here to present a detailed anatomical and functional description of the compound eye. Nor are we interested in its spectral sensitivity as a means of detecting and identifying objects in the field of view. Rather we will discuss only those features which govern its polarization sensitivity, that is, (a) its ability to sense the presence of polarized sunlight, and (b) its ability to discern the plane of polarization for purposes associated with navigation and position determination.

The compound eye is the most prominent and most important visual organ in both insects and crustaceans. (Compound eyes are also known from a handful of other animals, but these are always isolated exceptions in groups where other types of eye are dominant.) The ommatidia of compound eyes all possess the same three functional components mentioned above: a cornea, a cone and a rhabdom, whose functionalities vary widely from one species to another. The cornea is a specialized part of the cuticle, which in most animals is formed into a lens. In insects, crabs and stomatopods the ommatidial lens is formed by the cornea, either by its curved outer surface, by a graded refractive index within it, or by a combination of both.

But in truth although the curved outer surface of the cornea serves as a useful lens in air, among aquatic animals graded refractive index lenses ("lens cylinders") within the cornea or the crystalline cone provide both the most sensible and the most common solution. Amphibious animals in particular have a flat cornea so that the focal distance remains the same in air and in water. In fact, among amphipods and all lower crustaceans the crystalline cone even contains the entire ommatidial lens; here, the cornea seems to function simply as a protective cover over the eye. Conversely, in some cases the crystalline cone merely becomes an optical spacer that allows the cornea to focus on the distal tip of the rhabdom; in fact, among the apposition eyes of some taxa (*Limulus* and some beetles) the facets themselves project directly into the ommatidia as corneal cones and no crystal cones are formed at all. The isopod crustaceans assume an intermediate position because for them both the cornea and the crystalline cone may both take part in the focusing

Afocal Optics. But in still other species -in particular among butterflies- the crystalline cone has evolved differently, to a point where into the combination of corneal lens and crystalline cone forms a rather powerful afocal ("without focus") astronomical telescope. The system is called "afocal" because -in contrast with astronomical telescope- the recollimation is performed without the use of a second focusing lens Anatomically, this type of eye is indistinguishable from the simple apposition eye discussed above: as before, the ommatidia are optically isolated and the fused rhabdom behaves as a single lightguide. But here the variation lies in the remarkable optics of the crystalline cone. Parallel light incident on the cornea is focused to an image inside the crystalline cone, well above the rhabdom. Then in the proximal (narrow) stalk of the cone the beam is recollimated into a parallel pencil of rays which enters the rhabdom (Fig. 14).

If light from a distant source reaches the rhabdom as a narrow parallel beam, then slightly tilting the incident beam will cause a tilt six to seven times more severe, *viz.* an appreciable angular magnification, which is the essential physical characteristic of the optical telescope. It follows that the diameter of the incident beam, which is set by the facet diameter, becomes considerably reduced within the cone stalk so that the exit beam fits the size of the rhabdom tip even when the incident beam is tilted. This in turn leads to the quite remarkable conclusion that the corneal facet is imaged onto the corneal tip *and vice versa*. The field of view of the rhabdom will then be determined by the critical angle for total internal reflection within the rhabdom. In point of fact, the cone-stalk lens is actually an optical waveguide, which has been shown to be superior in many respects to a conventional focal system.

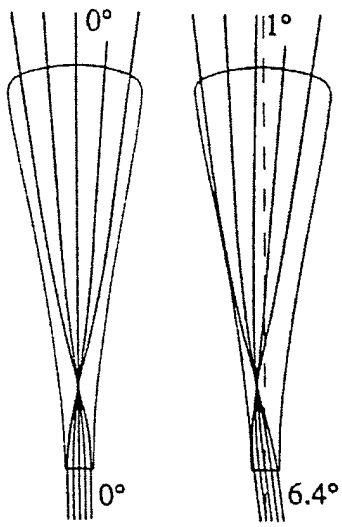

Fig. 14. Afocal Optics of the Crystalline Cone.

Treating the cone-stalk as part of the waveguide it can be shown both theoretically and experimentally (i) that such a system is superior by about 10% to a conventional focal system; (ii) that the resolution can reach very close to the diffraction limit set by the corneal lens; (iii) that the optical system can be interpreted as a refinement of a simple focal system.

The Rhabdom. The distal tip of each rhabdom lies in the focal plane of its corneal lens, and since the rhabdom only measures the intensity in that part of the image that falls on the distal tip (without resolving it) the ommatidium becomes the functional unit for spatial vision. As in all compound eyes the global image is erect even though the tiny unresolved image behind each lens is inverted.

The simplest type of apposition optics might be termed "simple apposition". It is by far the most common, and it is found *inter alia* in bees, locusts, mantids, cockroaches, dragonflies; among marine creatures it is also found in many types of crabs, stomatopods, amphipods, isopods and all lower crustaceans. It requires only two components: a positive lens and a single, sensitive lightguide, namely, the rhabdom. Rhabdoms of apposition eyes are frequently so narrow that geometrical optics fails to account for their behavior, and such cases must be treated according to the principles of dielectric waveguide theory, which treats the propagation of light in terms of discrete interference patterns modes called waveguide modes. These modes make the rhabdom waveguide behave as if it had diffuse borders, that is, some of the power propagates outside the rhabdom and by this means the distal tip of the ommatidium can also catch some light from outside its physical diameter. Together with the diffraction of the lens these waveguide effects render the ommatidium's angular sensitivity function bell-shaped, and neighboring ommatidia will therefore experience some overlap among their visual fields. The optimal amount of overlap depends on tradeoffs among contrast, resolution and sensitivity.

The simple apposition principle is in many respects a poor solution to the problem of spatial vision, Rhabdoms of insect apposition eyes are usually one or a few microns in diameter and 100 microns or more in length. But among many small crustaceans' eyes where inter-ommatidial angles are large, the rhabdoms are typically wider and considerably shorter, and in the extreme case their widths can be equal to their lengths, Among such simple apposition eyes with very short rhabdoms it has repeatedly been found that the ommatidial lens is not focused on the distal tip but much deeper, -sometimes, as in *Cirolana,* even below the rhabdom.

Rhabdomeres. As mentioned above, the rhabdom, which is the photosensitive element of the compound eye, is formed into microvillar extensions of the retinula cells, called rhabdomeres (Fig. 15). Embedded in the rhabdomeres are dioptric photopigment particles, which form the ultimate site of transduction from light energy to neuronal signals. The specific way in which rhabdomeres are organized into a rhabdom is a matter of great variation, which depends on the optical type of eye as well as species-specific factors that involve performance factors such as spectral discrimination and polarization sensitivity. For the sake of illustration

we shall consider three fundamentally different systems of rhabdomeres, one for the fly, the second for the worker-bee, and the third for crustaceans. Our purpose is to investigate the influence of the rhabdom's fine structure, and in particular its rhabdomeres, on both photodetection and navigation.

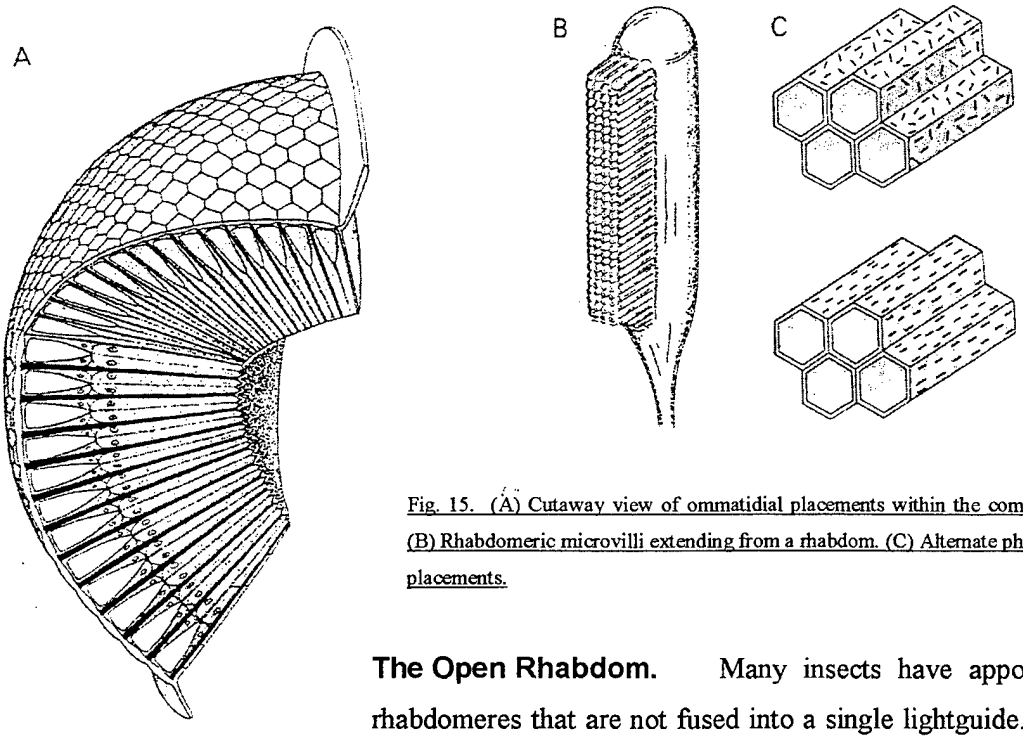

Fig. 15. (A) Cutaway view of ommatidial placements within the compound eye. (B) Rhabdomeric microvilli extending from a rhabdom. (C) Alternate photopigment placements.

The Open Rhabdom. Many insects have apposition eyes with rhabdomeres that are not fused into a single lightguide. These so-called "open rhabdom" eyes are found in dipteran flies, hemipteran bugs, earwigs and many beetles; among crustaceans, this most primitive kind of eye is known only from the isopod genus *Ligia*. Fig. 16 semi-schematically illustrates the open rhabdom arrangement at several descending levels within the ommatidium of a brachyceran fly.

The ommatidial optics of all eyes with open rhabdoms operate on the same principle, *viz.* a lens -usually the cornea- is focused on the distal tip of the rhabdom. The crystalline cone is frequently not crystalline at all (nor is it always cone-shaped!) but it forms a watery space between the cornea and the rhabdom's distal tip.

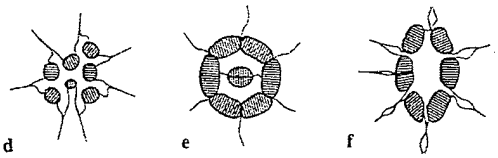

Fig. 16. The Fly's Open Rhabdom at Several Descending Levels.

However, the unifying feature among all such taxa is the open rhabdom, and so this type is sometimes designated as "focal apposition with an open rhabdom". The physical separation of the rhabdomeres has a drastic negative effect on spatial vision because the retinula cells of the ommatidium do not share the same visual field. In higher dipteran flies the rhabdomeres act as separate lightguides, all "looking" in different directions.

In each ommatidium there is a central lightguide surrounded by six wider ones in an asymmetric trapezoidal pattern. Although the six peripheral lightguides are each formed as an unbroken rhabdomere, the central lightguide is composed of two rhabdomeres, one positioned above the other, end to end. The central

pair are aimed in the same direction as one of the peripheral rhabdomeres in each of the six neighboring ommatidia. In this way the same spatial information reaches all of these rhabdomeres, and below the basement membrane the axons of their cells converge to one cartridge in the lamina. These rhabdomeres obey the principle of "neural superposition" because the information from one point in space is collected through several corneal facets, then superimposed neurally. The convergence of seven equivalent signals provides the same result as if the light were collected through a lens with an area seven times larger than any of the actual ones. This will of course reduce photon noise and thereby increase sensitivity, however diffraction is not reduced. The peripheral rhabdoms are often not separate from each other but form a ring around the two central ones. This kind of open rhabdom cannot resolve much spatial information within the ommatidium, and the peripheral rhabdomeres, *with high sensitivity and poor resolution*, simply experience a larger acceptance angle than the two central ones.

Polarization Sensitivity. But the central lightguide, which is composed of two rhabdomere cells stacked longitudinally one above the other, is narrower than the six surrounding ones. These two central cells do not take part in the neural superposition process described above but send their axons straight through the lamina cartridge without forming synaptic connections. and the central rhabdomeres constitute a separate system which lacks increased sensitivity but gains in increased resolution. What, then, is the functional significance of this central pair of rhabdomeres, having *low sensitivity and high resolution*, if they are not associated with neural superposition? The answer is that they are agents for detecting the polarization angle of the solar e-vector, and thereby they constitute the seat of the dipteran navigation function. The effect of containing a photosensitive material within a rhabdomere of small cross-sectional area is to increase the UV absorption relative to the visible, and also to shift the visible absorption peak to a shorter wavelength. For while the six peripheral receptors are maximally sensitive to the green (~486 nm), the two stacked rhabdoms are more than 2½ times more sensitive to the UV (350 nm).

It can be shown that because the two central rhabdomeres are thinner and shorter than the six peripheral, they have greater polarization sensitivities. Furthermore the upper rhabdomere acts like a polarization filter, and enhances the polarization sensitivity of the lower one; the longer the upper one, the greater the polarization enhancement effect.

Fused Rhabdoms. In the case of the dipteran species discussed above the microvilli were physically separated from one other, and this primitive type of structure is usually referred to as an "open" rhabdom. More numerous by far among invertebrate species are photoreceptor structures in which microvilli of different spectral type interact directly with one another in a more-or-less circular arrangement. These are referred to as "fused" rhabdoms, which in extreme cases may incorporate as many as eleven rhabdomeres within the rhabdom complex. Fig 17 illustrates this principle using a cross-sectional view of the ant *Formica*

polyctena in which the fused rhabdoms are evident at the center of the retinula. A growing body of evidence suggests that the fused rhabdom is in general formed by rhabdomeres with differing absorption characteristics. Presuming the necessary neural interconnections, an individual ommatidium is therefore capable of spectral discrimination.

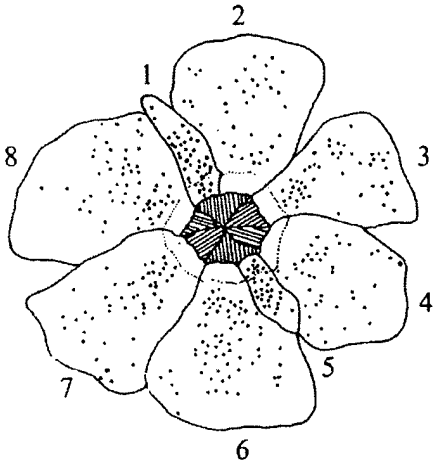

Fig. 17. *Formica* Rhabdom with Fused Rhabdomeres at Center

Because rhabdomeres of different spectral types are fused into a common light guide, the light-absorption properties of each type influence the manner in which light is transmitted along the composite rhabdom. The following conclusions apply to all fused rhabdom structures:

1. The rhabdomeres function as lateral absorption filters, consequently each rhabdom acts as if it were an absorption filter in front of all others in line. As a consequence of this filtering, the shape of the spectral sensitivity curve for each retinula cell is almost independent of the amount of light it absorbs, *viz.* independent of rhabdomere length and photopigment concentration. This is in direct contrast with the retinula cells of the dipteran flies described above, whose spectral sensitivity curves become progressively flatter as they absorb more and more light energy.
2. Therefore, one functional advantage of the fused rhabdom configuration is that optical coupling allows each retinula cell to have a high level of absolute sensitivity while still preserving its spectral identity, *viz.* narrow spectral sensitivity curves. The same receptors can operate at high sensitivity within a color vision system. Since all spectral types are included together in one rhabdom, the animal maintains faithful hue discrimination within a small field of view, *i.e.* fine-grain color vision.

The honeybee, *Apis mellifera*, is a commonly studied species which we shall use to illustrate the features and principles which characterize fused rhabdom structures. An important preliminary point to note is the functional analogy between the eighth cell of the dipteran retinula and the ninth cell of the honeybee retinula, for each of these has been shown to be responsible for UV detection within the species it supports. But the two species provide UV detection by different means: (1) the dipteran retinula's six separate rhabdoms are sensitive only to blue, green or yellow-green, and therefore a seventh (central) rhabdom is responsible for providing the first stage of UV detection. On the other hand, (2) the honeybee retinula's eight rhabdoms specifically do include two UV-sensitive rhabdoms which furnish the first stage of UV detection. But disregarding these configurational differences, in both of these cases the first detection stage embodies a high polarization sensitivity that allows it to act as a filter for the subsequent (basal) UV stage which in turn

measures the local *orientation* of the solar electric field vector, thereby providing the underlying basis for the animal's navigation.

Now insofar as the fused rhabdom configuration is concerned, the rhabdomeres of the two distal UV-sensitive rhabdoms can be seen to be oriented parallel rather than perpendicular to each other. This parallel configuration of microvilli allows the distal rhabdomeres to act as polarization enhancers for the ninth cell. This effect would be significantly reduced if the microvilli of the distal retinula cells were perpendicular to one another.

With only one polarization sensing cell per retinula it would appear that unambiguous determination of the polarization plane is impossible. However, two possible mechanisms do exist, the first based on interaction among ninth cells from neighboring ommatidia with overlapping fields of view; and the second based on the interaction between ninth cells pointing in the same direction within the two separate eyes. The first approach is generally possible because the inter-ommatidial angle in the dorsal-frontal eye region is only 0.8-1.6°, whereas the acceptance angle of retinula cells is in the range of 2.5°; furthermore the spatial arrangement of microvilli within the ninth cells do support this mechanism since in the dorsal and frontal eye region between twenty and fifty ommatidia are always looking at a 10° field of view. This in turn means that several pairs of neighboring ninth cells are looking at the same field at any given time. The second approach is based on the fact that each eye is the mirror image of the other. That is, *e.g.* microvilli in one eye which lie at 135° to the horizontal head axis appear to be at 45° relative to this axis in the contralateral eye. As the dorsal and frontal eye parts have a binocular field of view there are always ommatidia in both eyes that look at the same dorsal and frontal part of the visual field, *cf.* Fig. 12. Coordination would then be achieved by neuronal means.

Finally we consider a third type of fused rhabdom, which in marked contrast to flies and honeybees has a theoretical polarization sensitivity that is completely independent of their absolute sensitivity; furthermore the polarization sensitivity is very large owing to the rhabdom's characteristic structure. Its morphology is especially interesting for present purposes because it is naturally adapted to underwater navigation. To illustrate this specific point we choose the swimming crab, *Callinectes ornatus*, whose rhabdomeres are characteristically fused. As in the example of the honeybee described above, only seven of the eight retinula cells contribute a rhabdomere to the rhabdom. Here, however the microvilli of the rhabdomeres are arranged in alternating layers as depicted in Fig 18 , their longitudinal axes regularly aligned in a given direction for one

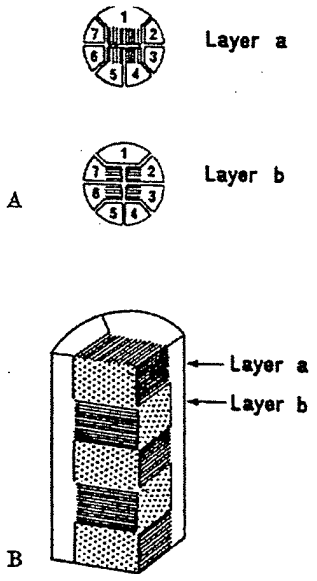

Fig. 18 Interleaved Crustacean-Like Rhabdom

where λ is the wavelength in vacuum, d is the diameter of the rhabdomere and n_1, n_2 are the indices of refraction of the rhabdomere and its surrounding medium, respectively. In the wavelength interval under present consideration, $300\text{ nm} < \lambda < 600\text{ nm}$. Adopting typical values for the refractive indices yields $1.74 > V > 0.87$ for the central pair of rhabdomeres, and so at most only two mode types can propagate down the length of the rhabdomere that detects polarization direction.

Two sustainable modes are associated with J_0, an ordinary Bessel function of the first kind which results from solving the electric field wave equation in cylindrical coordinates. It can alternatively -and here more usefully- be expressed in terms of the so-called LP_{lm} system of notation[5], a system of superimposed transverse fields of modes in a degenerate set. For J_0 the corresponding degenerate modes are TE_{01}, TM_{01} and HE_{21}. The first two terms refer to electric fields in the transverse plane, *i.e.* transverse to the rhabdomere fiber, and the third term to the magnetic field. In each of these three terms the first subscript designates the order of the mode, and the second is the rank of the mode. Also, the degenerate mode HE_{11} should be included, for it represents a sort of "constant" term in the illumination and is by definition always present in any solution of Bessel's equation in cylindrical coordinates.

The net result of all this is that HE_{11} plus the group of three terms noted above, *viz.* TE_{01}, TM_{01} and HE_{21} combine to form the linearly polarized (LP) modes LP_{01} and LP_{11}, whose intensity distributions along the rhabdomere fiber are displayed in Fig. 19. The electric field pattern for LP_{01} is simply a circular pattern, while the pattern for LP_{11} is shown in Fig. 20.

The challenge to the designer of an artificial photooptical sensor that emulates the rhabdom structure is to find a way of measuring the parameters of the modal pattern, and from the results to extract useful information about the direction of the incoming light as well as the direction of the plane of polarization. This point will be treated in a future report.

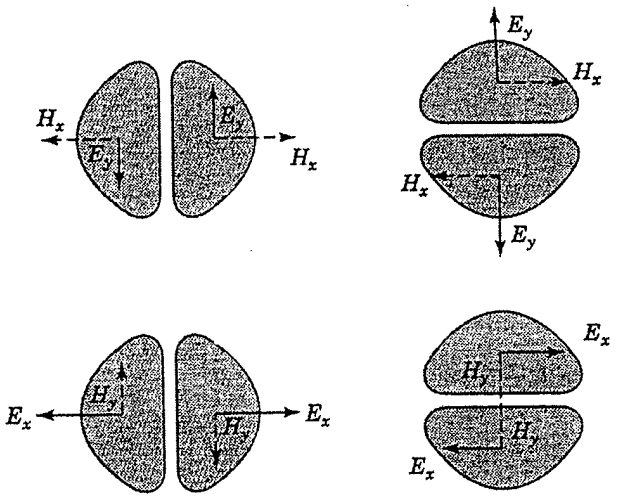

Fig.20. Electric Field Pattern for Mode LP_{11}

[5] "LP" stands for "Linearly Polarized"

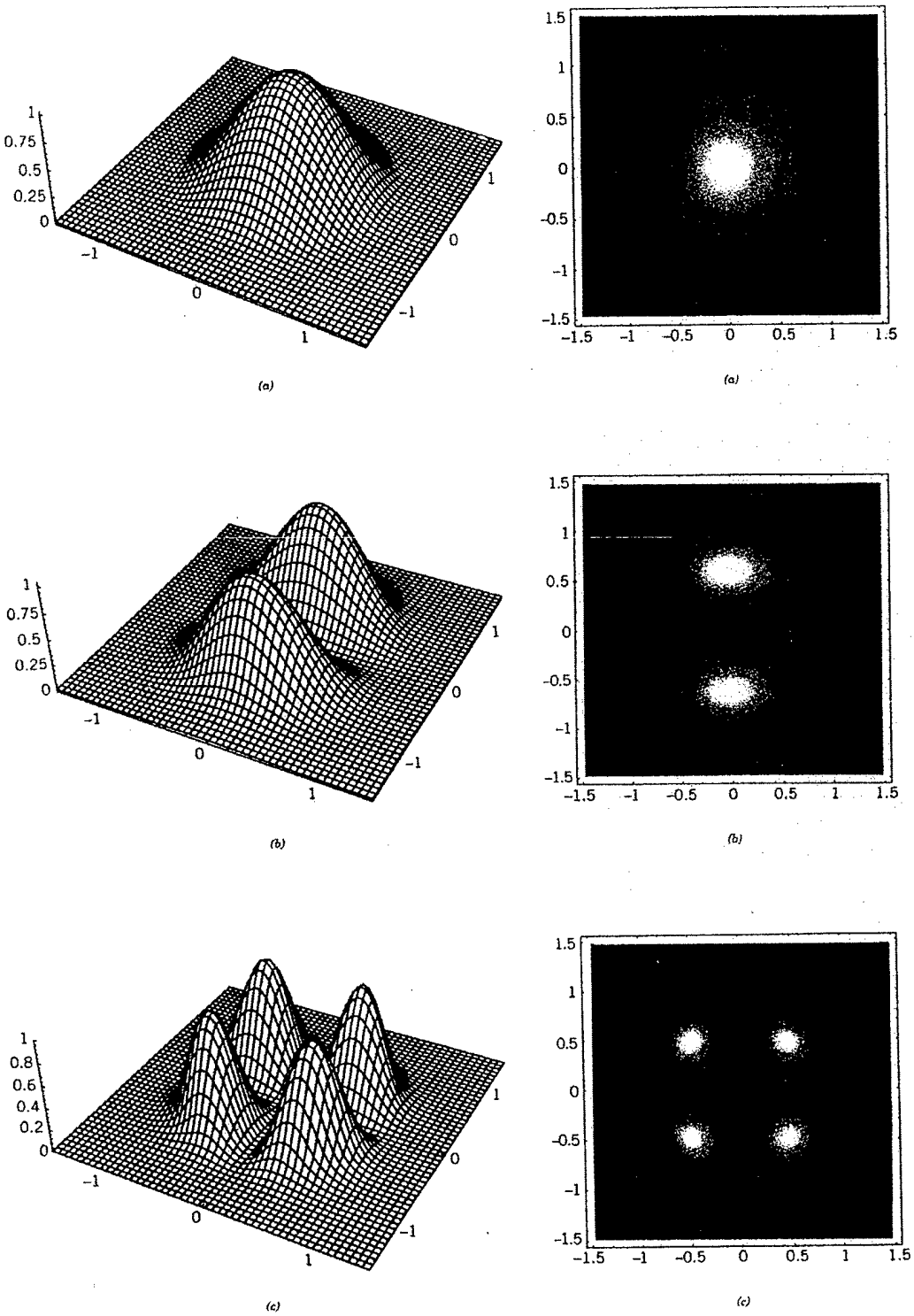

Figure 19. Intensity plots for the six LP modes, with $a = 1$. (a) LP_{01}: $u = 2$. (b) LP_{11}: $u = 3$. (c) LP_{21}: $u = 4.5$. (d) LP_{02}: $u = 4.5$. (e) LP_{31}: $u = 5.6$. (f) LP_{12}: $u = 6.3$.

5. REFERENCES

Geomagnetic Sensing.

Skiles, Durward D., *The Geomagnetic Field: Its Nature, History and Biological Relevance*, in: Magnetite Mineralization and Magnetoreception in Organisms, J.L. Kirschvink (ed.), Plenum Press, New York & London, 1985

Wiltschko, R. and Wiltsdchko, W., *Magnetic Orientation in Animals*, Springer, Berlin, New York, 1995

Gould, James L., *Magnetic Field Sensitivity in Animals,* Ann. Rev. Physiol.. 46: 585-98, 1984

Kalmijn, Ad. J., *The Electric and Magnetic Sense of Sharks, Skates and Rays*, Oceanus, 20: 45-52, 1977

Dijkgraaf, S. und Kalmijn, Ad. J., *Untersuchungen ηber die Funktion der Lorenzinischen Ampullen an Haifischen*, Z. v. Physiologie, 47: 438-456, 1963

Loewenstein, W.R. and Ishiko, N., *Sodium Chloride Sensitivity and Electrochemical Effects in a Lorenzinian Ampulla*, Nature 194: 4825, 21 April 1962, pp. 292-294

Murray, R.W. *Electrical Sensitivity of the AmpullΦ of Lorenzini*, Nature 187: 4741, 10 Sept. 1960, pg. 957.

Heiligenberg, W., *Electrolocation of Objects in the Electric Fish Eigenmanni*Φ *(Ramphichthydiae, Gymnotoidei*), J. comp. Physiol. 87: 137-164 (1973)

Kalmijn, Ad. J., *Electric and Magnetic Field Determination in Elesmobranch Fishes*, Science 218, 26 Nov. 1962, pp. 916-918

Waltman, B., *Electrical Properties and Fine Structure of the Ampullary Canals of Lorenzini*, Acta Physiologica Scandinavica, vol. 66, suppl. 264, 1966

Fessard, A. (Ed.), Handbook of Sensory Physiology, Vol III, No. 3, Electroreceptors and Other Specialized Receptors in Lower Vertebrates, Springer-Verlag, Berlin / Heidelberg / New York 1974

Bernd Kramer, Electroreception and Communication in Fishes, Progress in Zoology, Vol 42, publ. Gustav Fischer Stuttgart-Jena-L(beck-Ulm, 1996

Sensing the Direction of Solar Polarization.

Jerlov, N.G., Marine Optics, (Elsevier Oceanography Series, 5), 1976, Elsevier Scientific Publishing Co., Amsterdam-Oxford-New York

Ivanoff, A., *Polarization Measurements in the Sea*, in: Jerlov, N.G. and Nielsen, E.S. (eds,), Optical Aspects of Oceanography, Academic Press, London-New York, 1974

Timofeyeva, V.A., *Optical Characteristics of Turbid Media of the Seawater Type*, Izv. AN SSSR, Atm. Phys., 7, (12) 1971, pp. 1326-1329

Timofeyeva, V.A., *Plane of Vibrations of Polarized Light in Turbid Media*, Izv. AN SSSR, Atm. Phys., 7, (10) 1971, pp. 1049-1057

Ivanoff, A., and Waterman, T.H., *Factors, Mainly Depth and Wavelength, Affecting the Degree of Underwater Light Polarization*, Jour. Marine Res., 16 (3), 1958, pp. 283-307

Clarke, G.L., *Observations on the Penetration of Daylight into Mid-Atlantic and Coastal Waters*, Biol. Bull., LXV, Aug-Dec 1933, pp. 317-337

Oster, R.H., and Clarke, G.L., The Penetration of the Red, Green and Violet Components of Daylight into Atlantic Waters, JOSA 25 , Mar. 1935, pp 84-91

Waterman, T.H. and Westell, W.E., *Quantitative Effect of the Sun's Position on Submarine Light Polarization*, Jour. Marine Res., 15 (2), 1956, pp. 148-169

Waterman, T.H., *Polarization of Scattered Sunlight in Deep Water*, Deep Sea Research, vol .3 Suppl. (Papers on Marine Biology and Oceanography), pp.426-434

Clarke, G.L., *On the Depth at Which Fish can See*, Ecology, 17 (3) 1936, pp. 452-456

Waterman, T.H., *Visual Direction Finding in Fishes*, in: Animal Orientation and Navigation, Galler, S.R. (ed.), Session V. Sensory Mechanisms-Optical Senses, NASA SP-262, 1972

Waterman, T.H., *Interaction of Polarized Light and Turbidity in the Orientation of Daphnia and Mysidium*, Z. vergl. Physiologie, 43: 149-172 (1960)

Smith, K.C. and Macagno, E.R., *UV Photoreceptors in the Compound Eye of Daphnia magna (Crustacea, Branchiopoda). A Fourth Spectral Class in a Single Ommatidia*, Jour. Comp. Physiol. A, 166: 597-606, 1990

Hawyryshyn, C.W., *et al*, *Spatial Orientation of Rainbow Trout* to plane-Polarized Light: The Ontogeny of E0Vector Discrimination and Spectral Sensitivity Characteristics, J. Comp. Physiol. A (1990) 166: 565-574

Moody, M.F. and Parriss, *The Discrimination of Polarized Light by Octopus: A Behavioral and Morphological Study*, Z. vergl. Physiologie 44, 268-291 (1961)

Kleerekoper, H. *et al*, *Locomotor Response of the Goldfish to Polarized Light and its E-Vector*, J. Comp. Physiol., 86, 27-36 (1973)

Jander, R., et al., *Polarized Light.Orientation by Two Hawaiian Decapod Cephalopods*, Z. vergl. Physiologie 46, 383-394 (1963)

Saidel, W.M., et al., *Processing of Polarized Light by Squid Photoreceptors*, Nature, 304 11 Aug. 1963 (534–536)

Tasaki, K. and Karita, K., *Discrimination of Horizontal and Vertical Planes of Polarized Light by the Cephalopod Retina,* Jap. Jour. of Physiology, 16, pp. 205-216 (1966)

Williamson, R., et al., *Neuronal Circuits in Cephalopod Vision*, Netherlands Journal of Zoology, 44, 3/4, 272-283 (1994)

Duelli, P. and Wehner R., *The Spectral Sensitivity of Polarized Light Orientation in Cataglyphis bicolor (FormicidΦ, Hymenoptera)*, J. Comp. Physiol. 86, 37-53 (1973)

Nilsson, D.E. and Howard, J., *Intensity and Polarization of the Eyeshine in Butterflies*, J. Comp. Physiol A (1989) 166: 51-56

Von Helversen und Edrich, W., *Der Polarisationsempf≡nger in Bienenauge: ein Ultraviolettrezeptor*, J. Comp. Physiol. 94, 33-47 (1974)

Smakman, J.G.J. , *et al, Angular Sensitivity of Blowfly Receptors: Intracellular Measurements and Wave-Optical Predictions*, J. Comp. Physiol A (1984) 155: 239-247

Von Frisch, K. *et al, Øber die Wahrnehmung polarisierten Lichtes durch das Bienenauge*, Experientia, vol XVI, Fasc. 7 (289-336) 13 VII 1960

Horv<th, G. and Wehner, R., *Skylight Polarization as Perceived by Desert Ants and Measured by Video Polarimetry*, J. Comp. Physiol. A (1999) 184: 1-7

Alerstam, T. *et al.*, *Migration Along Orthodromic Sun Compass Routes by Arctic Birds*, Science, 291, 12 Jan 2001 (300-303)

Rossel, S. and Wehner, R., *How Bees Analyze the Polarization Patterns in the Sky*, J. Comp. Physiol A, (1984) 154:607-615

Labhart, T., *The Electrophysiology of Photoreceptors in Different Eye Regions of the Desert Ant, Cataglyphis bicolor*, J. Comp. Physiol. A (1986) 158:1-7

Wehner, R., *Dorsoventral Asymmetry in the Visual Field of the Bee, Apis mellifica*, J. Comp. Physiol. 77, 256-277 (1972)

Labhart, T., *Specialized Photoreceptors at the Dorsal Rim of the Honeybee's Compound Eye*: Polarizational and Angular Sensitivity, J. Comp. Physiol., 141, 19-30 (1980)

Hardie, R.C., *Properties of Photoreceptors R7 and R8 in Dorsal Marginal Ommatidia in the Compound Eyes of Musca and Calliphora*, J. Comp. Physiol A (1984) 154:157-165

Aepli, F., *et al, Structural Specializations of the Cornea and Retina at the Dorsal Rim of the Compound Eye in Hymenopteran Insects*, Cell Tissue Res. (1985) 239:19-24

Nilsson, D-E., *et al, Photoreceptor Design and Optical Properties Affecting Polarization Sensitivity in Ants and Crickets*, J. Comp. Physiol. A, (1987) 161:645-658

Wunderer, H. and Smola, U., *Fine Structure of Ommatidia at the Dorsal Eye Margin of Calliphora Erythrocephala Meigen (Diptera, CalliphoridΦ), an Eye Region Specialised for the Detection of Polarized Light*, Int. J. Insect Morphol. & Embryol., vol. 11 (25-38) 1982

Kolb, G., *Retinal Ultrastructure in the Dorsal Rim and Large Dorsal Area of the Eye of Aglais urticΦ (Lepidoptera)*, Zoomorphology (1986) 106:244-246

Wehner, R. et al., *Twisted and non-Twisted Rhabdoms and their Significance for Polarization Detection in the Bee*, J. Comp. Physiol, 104, 225-245 (1975)

Laughlin, S.B. and G.A. Horridge, *Angular Sensitivity of the Retinula Cells of the Dark-Adapted Worker Bee*, Z. vergl. Physiologie 74, 329-335 (1971)

Smakman, *et al., Angular Sensitivity of Blowfly Receptors: Intracellular Measurements and Wave-Optical Predictions*, J. Comp. Physiol. A (1984) 155:239-247

Van Hateren, J.H., *Waveguide Theory Applied to Optically Measured Angular Sensitivities of Fly Receptors*, J. Comp. Physiol. A (1984) 154:761-771

Nilsson, D-E. *et al., Photoreceptor Design and Optical Properties Affecting Polarization Sensitivity in Ants and Crickets*, J. Comp. Physiol. A (1987) 161:645-658

Nilsson, D-E. *et al., Optics of the Butterfly Eye,* J. Comp. Physiol. A (1988) 162:341-366

Nilsson, D-E. *et al., Afocal Apposition Optics in Butterfly Eyes*, Nature 312, 561-563, 6 December 1984

Snyder, A.W., *Angular Sensitivity of the Bee Ommatidium*, Z. vergl. Physiologie 76 , 438-445 (1972)

Snyder, A.W., *Polarization Sensitivity of Individual Retinula Cells*, J. Comp. Physiol. 83, 331-360 (1973)

Snyder, A.W., *Acuity of Compound Eyes: Physical Limitations and Design*, J. Comp. Physiol. 116, 161-182 (1977)

Snyder, A.W., *et al, Structure and Function of the Fused Rhabdom*, J. Comp. Physiol. 87, 99-135 (1973)

Snyder, A.W., *et al., Failure of Geometric Optics for Analysis of Circular Optical Fibers*, J. Optical Soc. Amer., 64/5: 608- 614, May 1974

Snyder, A.W. and C. Pask, *Detection of Polarization and Direction by the Bee Rhabdom*, J. Comp. Physiol. 78, 346-355 (1972)

Menzel, R. and A.W. Snyder, *Polarized Light Detection in the Bee, Apis mellifera*, J. Comp. Physiol. 88, 247-270 (1974)

Land, M.L. and D. C. Osorio, *Waveguide Modes and Pupil Action in the Eyes of Butterflies*, Proc. R. Soc. Lond. B (1990) 241, 93-100

Van Hateren, J.H., Waveguide Theory Applied to Opticically Measured Angular Sensitivities of Fly Photoreceptors, J. Comp. Ohysiology A (1984) 154:761-771

Mazokhin-Porshnyakov, G, Insect Vision, (in English), Plenum Press, New York 1969

A.W. Snyder and Love, J.D. Optical Waveguide Theory, Kluwer, Amsterdam, New York, 1983

J.A. Buck, Fundamentals of Optical Fibers, John Wiley & Sons, New York-Chichester-Brisbane-Toronto-Singapore, 1995

G.A. Horridge (ed.), The Compound Eye and Vision of Insects, Clarendon Press, Oxford 1975

Sandra Sinclair, How Animals See: Other Visions of our World, Facts on File Publications, New York- Oxford, 1985

Sigmund Exner , The Physiology of the Compound Eyes of Insects and Crustaceans, (transl. Roger C. Hardie), Springer-Verlag, Berlin-Heidelberg, New York-London-Paris-Tokyo, 1989

Handbook of Sensory Physiology, Volume VII/1, Photochemistry of Vision, (ed. Herbert J.A. Dartnall), Springer-Verlag, Berlin-Heidelberg-New York 1972

Comparative Physiology and Evolution of Vision in Invertebrates, Part A: Invertebrate Photoreceptors, (ed. H. Autrum), Springer-Verlag Berlin-Heidelberg-New York, 1979

Comparative Physiology and Evolution of Vision in Invertebrates, Part C: Invertebrate Visual Centers and Behavior II, (ed. H. Autrum), Springer-Verlag Berlin-Heidelberg-New York, 1981

D.G. Stavenga and R.C. Hardie (Eds.)Facets of Vision, Springer-Verlag Berlin-Heidelberg-New York, 1989

Attachment 4 - Sonar Parametrics - Revised

This white paper is a Mathcad symbolic spreadsheet using basic principles of underwater sound equations found in Principles of Underwater Sound by Robert J. Urick. It's purpose is to calculate some parametric evaluations of acoustic power versus range from 1 to 15 meters. It also looks at parametrics of pulse width, cycle time, frequency and efficiency.

Revision 1:

The frequency for calculation of absoption loss is revised from 40 KHz to 3.75 MHz.

The pulse width (PW) is revised to represent a one bit pulse of 10^5 s for acoustic imaging, and two additional pulses for extension of design to include communications capability, a 1 ms PW (100 bits) and a 10 ms PW (1000 bits).

The Pulse Rep Rate is revised to include 1 sec, 5 sec, and 10 sec.

Calculations and plots are added for theoretical power required for a range of 15 meters

Calculations and plots are added for power parametrics vs PW and PRR variants

Basic Sonar Acoustic Concepts

$\rho c := 1.5 \cdot 10^5 \quad \frac{gm}{(cm^2) \cdot (s)}$ **ρc = Specific Acoustic Resistance for seawater**

ρ = fluid density

c = speed of sound in fluid

For a plane acoustic wave propagating in seawater, **acoustic pressure p**:

u = particle velocity of water

$u := 6.667 \cdot 10^{-6} \quad \frac{cm}{s}$

$p := \rho c \cdot u \quad \frac{dyne}{cm^2}$

$p = 1 \quad \frac{dyne}{cm^2}$

A propagating sound wave carries mechanical energy with it in the form of kinetic energy in the moving particles, and potential energy in stresses stored in the elasticity of the fluid. As the wave propagates a certain amount of energy per second or power will flow across a unit area boundary normal to the propagation. The **power per unit area** is the **acoustic intensity (I).**

$$I := \left(\frac{p^2}{\rho c}\right) \quad \frac{erg}{cm^2 s}$$ **Instantaneous Intensity**

Time averaging the acoustic pressure results in an **average intensity**:

$$pavg := 1 \quad \frac{dyne}{cm^2} \quad rms$$

$$Iavg := \left(\frac{pavg^2}{\rho c}\right) \cdot 10^{-7} \quad \frac{W}{cm^2}$$ Multiply by 1W/10^7ergs/s to convert to W/square cm

$$Iavg = 6.667 \times 10^{-13} \quad \frac{W}{cm^2}$$

DB Referenced to one MicroPascal

The **unit of intensity reference** in underwater acoustics is a plane wave having a rms pressure of **one Micro Pascal (1 uPa)**

$$\mu Pa := 10^{-5} \quad \frac{dyne}{cm^2}$$

1 uPa is equivalent to a power intensity of :

$$Power\_Intensity := 0.67 \cdot 10^{-22} \quad \frac{W}{cm^2}$$

The **Unit of Energy Flux Density** is the energy density of a 1 uPa plane wave integrated over one second

$$\text{Energy} := \int_0^1 I\,dt = \frac{1}{\rho c}\left(\int p^2\,dt\right)$$ **Energy Flux Density**

$$E1 := 0.64\,10^{-22}\ W\cdot\frac{s}{cm^2}$$

The **Level** of a sound wave is the is the number of decibels which its intensity or energy flux density differs from the reference sound wave having a sound pressure of 1 uPa.

If I1 and I2 are two intensities the number N denoting their ratio I1/I2 is:

N = 10 log10 I1/I2 dB

If I2 is the refernce wave then I1 has a level equal to N dB. which is written "N dB re 1 uPa"

Table Comparing dB to Pressure to Energy Flux

dB re 1uPa	Plane Wave rms Pressure dyne/square cm	Energy Density W/square cm
120	10	$6.667\,10^{-11}$
100	1	$6.667\,10^{-12}$
80	10^{-1}	$6.667\,10^{-13}$
60	10^{-2}	$6.667\,10^{-14}$
40	10^{-3}	$6.667\,10^{-15}$
20	10^{-4}	$6.667\,10^{-16}$
0	10^{-5}	$6.667\,10^{-17}$

Transmission Loss

Transmission loss (TL) describes the weakening of a sound between a refence point 1 meter from the source and some distance r2:

TL = 10 log I1/I2 DB

Since I1 and I2 are intensities a time average is implied. The sources of transmission loss is a summation of **spreading losses** in the medium, and **absorption** of energy by the medium. Several models exist for spreading losses based on acoustic environment and geometry.

Spherical Spreading Loss

Spherical spreading is a good approxamation for spreading losses in most cases. Spherical spreading assumes that the power generated by the source is radiated equally in all directions and is evenly distributed over the surface of a sphere. Assuming no loss in the medium, the power crossing all such spheres must be the same.

P = 4(pi)*(r1)squared = 4(pi)*(r2)squared = . . .

Since r1 is the reference and is taken as 1 yd the transmission loss to range r2 is:

$r1 := 1 \quad m$

$$r2 := \begin{pmatrix} 1 \\ 2 \\ 3 \\ 4 \\ 5 \\ 6 \\ 7 \\ 8 \\ 9 \\ 10 \\ 11 \\ 12 \\ 13 \\ 14 \\ 15 \end{pmatrix} \quad m$$

TL_spreading := 20·log(r2) dB

TL_spreading =

	0
0	0
1	6.021
2	9.542
3	12.041
4	13.979
5	15.563
6	16.902
7	18.062
8	19.085
9	20
10	20.828
11	21.584
12	22.279
13	22.923
14	23.522

dB

Absorption Loss

Absorption loss is due to the acoutic energy heating the medium, and is a true loss to the medium. When a plane wave travels through an absorbing medium a small amount of intensity is lost in each small distance traveled. For an intensity I traveling through a small distance dx a small intensity loss di is experienced. The relationship is

dI/I = -ndx

Integrating from radius r1 to radius r2 gives a relationship between the intensities at these two radiuses.

I2 = I1e

n := .5

r1 := 1 m

$I2 := I \cdot e^{-n \cdot (r2 - r1)}$ dB

$I2 =$

	0
0	$6.667 \cdot 10^{-6}$
1	$4.044 \cdot 10^{-6}$
2	$2.453 \cdot 10^{-6}$
3	$1.488 \cdot 10^{-6}$
4	$9.023 \cdot 10^{-7}$
5	$5.473 \cdot 10^{-7}$
6	$3.319 \cdot 10^{-7}$
7	$2.013 \cdot 10^{-7}$
8	$1.221 \cdot 10^{-7}$
9	$7.407 \cdot 10^{-8}$
10	$4.492 \cdot 10^{-8}$
11	$2.725 \cdot 10^{-8}$
12	$1.653 \cdot 10^{-8}$
13	$1.002 \cdot 10^{-8}$
14	$6.08 \cdot 10^{-9}$

dB

Taking 10 times the log of both sides

10 log I2 - 10 log I1 = -10n(r2-r1)log e

a = 10 n log e

The change in level between r2 and r1 becomes

10 log I2 - 10 log I1 = - a(r2 - r1)

Or TL_absorption = -ar

Absorption Coefficient as a Function of Intensity and Range

$I = 6.667 \times 10^{-6}$ dB

$I2 =$

	0
0	$6.667 \cdot 10^{-6}$
1	$4.044 \cdot 10^{-6}$
2	$2.453 \cdot 10^{-6}$
3	$1.488 \cdot 10^{-6}$
4	$9.023 \cdot 10^{-7}$
5	$5.473 \cdot 10^{-7}$
6	$3.319 \cdot 10^{-7}$
7	$2.013 \cdot 10^{-7}$
8	$1.221 \cdot 10^{-7}$
9	$7.407 \cdot 10^{-8}$
10	$4.492 \cdot 10^{-8}$
11	$2.725 \cdot 10^{-8}$
12	$1.653 \cdot 10^{-8}$
13	$1.002 \cdot 10^{-8}$
14	$6.08 \cdot 10^{-9}$

dB

$i := 0, 1 .. 14$

$$\alpha_i := \frac{\left(10 \cdot \log(I) - 10 \cdot \log\left(I2_i\right)\right)}{\left(r2_i - r1\right)}$$

logarithmic absorption coefficient in dB/Km

$\alpha =$

0
2.171
2.171
2.171
2.171
2.171
2.171
2.171
2.171
2.171
2.171
2.171
2.171
2.171
2.171
2.171

$\frac{dB}{K \cdot m}$

Absorption Coefficient as Function of Frequency

$f := 1 \quad KHz$

$$\alpha(f) := \frac{0.1 \cdot (f^2)}{(1 + f^2)} + \frac{40 \cdot f^2}{(4100 + f^2)} + 2.75 \cdot 10^{-4} \cdot f^2 + 0.003$$

$\alpha(f) = 0.063 \quad \frac{dB}{K \cdot m}$

Total Transmission Loss

The total transmission loss is equal to the spreading transmission loss plus absorption transmission loss.

$$TL := 20 \cdot \log(r2) + \alpha(f) \cdot r2 \cdot 10^{-3} \quad dB$$

$TL =$

	0
0	$6.303 \cdot 10^{-5}$
1	6.021
2	9.543
3	12.041
4	13.98
5	15.563
6	16.902
7	18.062
8	19.085
9	20.001
10	20.829
11	21.584
12	22.28
13	22.923
14	23.523

dB

Changing the frequency from 1kHz to 3.75 MHz and recalculating absorption loss and Transmission Loss.

$f := 3.75 \cdot 10^3$ KHz

$$\alpha(f) := \frac{0.1 \cdot (f^2)}{(1 + f^2)} + \frac{40 \cdot f^2}{(4100 + f^2)} + 2.75 \cdot 10^{-4} \cdot f^2 + 0.003$$

$$\alpha(f) = 3.907 \times 10^3 \frac{dB}{K \cdot m}$$

$TL := 20 \cdot \log(r2) + \alpha(f) \cdot r2 \cdot 10^{-3}$ dB

$TL =$

	0
0	3.907
1	13.835
2	21.264
3	27.67
4	33.516
5	39.007
6	44.253
7	49.32
8	54.25
9	59.073
10	63.808
11	68.471
12	73.073
13	77.624
14	82.131

dB

This parametric of frequency, shows that the change in absorption does not significantly effect the total transmission loss in the range of interest (1 - 15 meters). It is typically an impact in the Km range.

Relating Source Level to Radiated Acoustic Power

$pr := 10 \ \frac{dyne}{cm^2}$ Assuming an rms plane wave pressure of 10 dyne/square cm based on Table 1.2 from Urick.

$Ir := 5.58\,10^{-9} \cdot pr^2 \quad \frac{W}{m^2}$

$Ir = 5.58 \times 10^{-7} \quad \frac{W}{m^2}$

$Pr_{10} := 70.0\,10^{-9} \cdot pr^2 \cdot r2^2 \quad W$ $Pr_{plus15} := (70.0\,10^{-9} \cdot pr^2 \cdot r2^2) \cdot 1.15 \quad W$

$Pr_{minus15} := (70.0\,10^{-9} \cdot pr^2 \cdot r2^2) \cdot .85 \quad W$

We considered the possibility that our analysis might have some error. In order to bracket the error we assumed +/- 15% error.

$Pr_{10} =$

	0
0	$7 \cdot 10^{-6}$
1	$2.8 \cdot 10^{-5}$
2	$6.3 \cdot 10^{-5}$
3	$1.12 \cdot 10^{-4}$
4	$1.75 \cdot 10^{-4}$
5	$2.52 \cdot 10^{-4}$
6	$3.43 \cdot 10^{-4}$
7	$4.48 \cdot 10^{-4}$
8	$5.67 \cdot 10^{-4}$
9	$7 \cdot 10^{-4}$
10	$8.47 \cdot 10^{-4}$
11	$1.008 \cdot 10^{-3}$
12	$1.183 \cdot 10^{-3}$
13	$1.372 \cdot 10^{-3}$
14	$1.575 \cdot 10^{-3}$

$Pr_{plus15} =$

	0
0	$8.05 \cdot 10^{-6}$
1	$3.22 \cdot 10^{-5}$
2	$7.245 \cdot 10^{-5}$
3	$1.288 \cdot 10^{-4}$
4	$2.013 \cdot 10^{-4}$
5	$2.898 \cdot 10^{-4}$
6	$3.945 \cdot 10^{-4}$
7	$5.152 \cdot 10^{-4}$
8	$6.52 \cdot 10^{-4}$
9	$8.05 \cdot 10^{-4}$
10	$9.741 \cdot 10^{-4}$
11	$1.159 \cdot 10^{-3}$
12	$1.36 \cdot 10^{-3}$
13	$1.578 \cdot 10^{-3}$
14	$1.811 \cdot 10^{-3}$

$Pr_{minus15} =$

	0
0	$5.95 \cdot 10^{-6}$
1	$2.38 \cdot 10^{-5}$
2	$5.355 \cdot 10^{-5}$
3	$9.52 \cdot 10^{-5}$
4	$1.488 \cdot 10^{-4}$
5	$2.142 \cdot 10^{-4}$
6	$2.916 \cdot 10^{-4}$
7	$3.808 \cdot 10^{-4}$
8	$4.819 \cdot 10^{-4}$
9	$5.95 \cdot 10^{-4}$
10	$7.2 \cdot 10^{-4}$
11	$8.568 \cdot 10^{-4}$
12	$1.006 \cdot 10^{-3}$
13	$1.166 \cdot 10^{-3}$
14	$1.339 \cdot 10^{-3}$

$p1 := 1 \quad \frac{dynes}{cm^2}$ p1 is the rms pressure at 1 meter

$P1 := 70.0\,10^{-9} \cdot p1^2$ W

$P1 = 7 \times 10^{-8}$ W

Converting to decibels and remembering that 10 log p1 squared is the source level SL
If p1 is the reference pressure and is 1 μPa

10 log P = -171.5 + SL, or SL = 171.5 + 10 log P

If the projector is directional it will have a directivity index DIT

$DIT := 15$ From figure 3.6 Directivity Index Nomogram in Urick

$SL_{10} := 171.5 + 10 \cdot \log(Pr_{10}) + DIT$

$SL_{10} =$

	0
0	134.951
1	140.972
2	144.493
3	146.992
4	148.93
5	150.514
6	151.853
7	153.013
8	154.036
9	154.951
10	155.779
11	156.535
12	157.23
13	157.874
14	158.473

dB

This is a reasonable source level when compared tc commercialy available transducers.

Parametrics on Radiated Pressure

$pr_1 := 1 \ \frac{dyne}{cm^2}$ Assuming an rms plane wave pressure of 1 dyne/square cm based on Table 1.2 from Urick.

$Ir_1 := 5.58\,10^{-9} \cdot pr_1^{\,2} \quad \frac{W}{m^2}$

$Ir_1 = 5.58 \times 10^{-9} \quad \frac{W}{m^2}$

$Pr_1 := 70.0\,10^{-9} \cdot pr_1^{\,2} \cdot r2^2 \quad W$

$Pr_1 =$

	0
0	$7 \cdot 10^{-8}$
1	$2.8 \cdot 10^{-7}$
2	$6.3 \cdot 10^{-7}$
3	$1.12 \cdot 10^{-6}$
4	$1.75 \cdot 10^{-6}$
5	$2.52 \cdot 10^{-6}$
6	$3.43 \cdot 10^{-6}$
7	$4.48 \cdot 10^{-6}$
8	$5.67 \cdot 10^{-6}$
9	$7 \cdot 10^{-6}$
10	$8.47 \cdot 10^{-6}$
11	$1.008 \cdot 10^{-5}$
12	$1.183 \cdot 10^{-5}$
13	$1.372 \cdot 10^{-5}$
14	$1.575 \cdot 10^{-5}$

$p1 := 1 \quad \frac{dyne}{cm^2}$

$P1 := 70.0\,10^{-9} \cdot p1^2 \quad W$

$P1 = 7 \times 10^{-8} \quad W$

Converting to decibels and remembering that 10 log p1 squared is the source level Sl

10 log P = -171.5 + SL, or SL = 171.5 + 10 log P

If the projector is directional it will have a directivity index DIT

$DIT := 15$ From figure 3.6 Directivity Index Nomogram ref (1)

$SL_1 := 171.5 + 10 \cdot \log(Pr_1) + DIT$

$SL_1 =$

	0
0	114.951
1	120.972
2	124.493
3	126.992
4	128.93
5	130.514
6	131.853
7	133.013
8	134.036
9	134.951
10	135.779
11	136.535
12	137.23
13	137.874
14	138.473

dB

$$pr_5 := 5 \ \frac{dyne}{cm^2}$$

$$Ir_5 := 5.58 \cdot 10^{-9} \cdot pr_5^{\ 2} \quad \frac{W}{m^2}$$

$$Ir_5 = 1.395 \times 10^{-7} \quad \frac{W}{m^2}$$

$$Pr_5 := 70.0 \cdot 10^{-9} \cdot pr_5^{\ 2} \cdot r2^2 \quad W$$

$Pr_5 =$

	0
0	$1.75 \cdot 10^{-6}$
1	$7 \cdot 10^{-6}$
2	$1.575 \cdot 10^{-5}$
3	$2.8 \cdot 10^{-5}$
4	$4.375 \cdot 10^{-5}$
5	$6.3 \cdot 10^{-5}$
6	$8.575 \cdot 10^{-5}$
7	$1.12 \cdot 10^{-4}$
8	$1.417 \cdot 10^{-4}$
9	$1.75 \cdot 10^{-4}$
10	$2.118 \cdot 10^{-4}$
11	$2.52 \cdot 10^{-4}$
12	$2.957 \cdot 10^{-4}$
13	$3.43 \cdot 10^{-4}$
14	$3.938 \cdot 10^{-4}$

$p1 := 1 \quad \frac{dyne}{cm^2}$

$P1 := 70.0\,10^{-9} \cdot p1^2 \quad W$

$P1 = 7 \times 10^{-8} \quad W$

Converting to decibels and remembering that 10 log p1 squared is the source level SL

10 log P = -171.5 + SL, or SL = 171.5 + 10 log P

If the projector is directional it will have a directivity index DIT

$DIT := 15$ From figure 3.6 Directivity Index Nomogram ref (1)

$SL_5 := 171.5 + 10 \cdot \log(Pr_5) + DIT$

$SL_5 =$

	0
0	128.93
1	134.951
2	138.473
3	140.972
4	142.91
5	144.493
6	145.832
7	146.992
8	148.015
9	148.93
10	149.758
11	150.514
12	151.209
13	151.853
14	152.452

dB

Source Level related to Electrical Power

P is the acoustic power radiated by the transducer. P is less than the electrical power input into the transducer by a factor of efficiency of the transducer.

$$\eta = P/Pe$$

Where η = transducer efficiency
P = Radiated Acoustic Power
Pe = Electrical Power

Therefore, $P = \eta Pe$ Substituting into the Source Level equation:

Bracketing efficiency from $\eta = .2$ to $\eta = 1$

$\eta e := .2$

$Pe := 25 \cdot 10^{-6}$

$SLe := 171.5 + 10 \cdot \log(Pe) + 10 \cdot \log(\eta e) + DIT$

$SLe = 133.49$ dB

$\eta e := 1$

$Pe := 25 \cdot 10^{-6}$

$SLe := 171.5 + 10 \cdot \log(Pe) + 10 \cdot \log(\eta e) + DIT$

$SLe = 140.479$ dB

Active Sonar Equation

SL - 2TL + TS - (NL - DI) = DT

SL = Source Level

TL = Transmission Loss

TS = Target Strength

NL = Noise Level

DI = Directivity Index

DT = Detection Threshold

For equal probability of detection Echo level = Noise masking or

SL - 2TL +TS = NL - DI + DT

Where Echo Level is the left side of the equation and noise masking background \ is the right side of the equation.

Transient form of Sonar Equation

The previous discussion was in terms of the acoustic intensity or average acoustic power per unit area of sound transmitted or received. This discussion implied time averaged. For a pulsed or transient sonar a more general approach is to write the equations in terms of the energy flux density (E). For a plane wave with a time varying pressure p(t):

$$E := \frac{1}{\rho c}\left(\int_0^{\infty} pt(t)^2\,dt\right) \qquad \frac{erg}{cm^2}$$

Intensity is the mean square pressure divided by ρc and averaged over an interval of time T

$$It := \frac{E}{T}$$

Parametrics on Pulse Width and Cycle Time

Pulse Width = τo = Transmit pulse duration.

$\tau_{o1} := 1 \cdot 10^{-5}$ s

$\tau_{o2} := 1 \cdot 10^{-3}$ s

$\tau_{o3} := 10 \cdot 10^{-3}$ s

Cycle Time τe = Time allowed for echo return

$\tau_{e1} := 1.00$ s Starting τe based on the Poloroid 6500 sonar ranging module

$\tau_{e2} := 5.00$ s

$\tau_{e3} := 10.00$ s

SLecho = 10*log(E) - 10 log(τe)

SLpulse = 10 log(E) - 10 log(τo)

$SLpulse := SL_{10}$ dB

$SLeff_{11} := SLpulse + 10 \cdot \log\left(\frac{\tau_{o1}}{\tau_{e1}}\right)$ Effective Source Level

$$SLeff_{l2} := SLpulse + 10 \cdot \log\left(\frac{\tau_{o1}}{\tau_{e2}}\right)$$

$$SLeff_{l3} := SLpulse + 10 \cdot \log\left(\frac{\tau_{o1}}{\tau_{e3}}\right)$$

$SLeff_{l1} =$

	0
0	84.951
1	90.972
2	94.493
3	96.992
4	98.93
5	100.514
6	101.853
7	103.013
8	104.036
9	104.951
10	105.779
11	106.535
12	107.23
13	107.874
14	108.473

dB

$SLeff_{l2} =$

	0
0	77.961
1	83.982
2	87.504
3	90.002
4	91.941
5	93.524
6	94.863
7	96.023
8	97.046
9	97.961
10	98.789
11	99.545
12	100.24
13	100.884
14	101.483

dB

$SLeff_{l3} =$

	0
0	74.951
1	80.972
2	84.493
3	86.992
4	88.93
5	90.514
6	91.853
7	93.013
8	94.036
9	94.951
10	95.779
11	96.535
12	97.23
13	97.874
14	98.473

dB

$$SLeff_{21} := SLpulse + 10\cdot\log\left(\frac{\tau_{o2}}{\tau_{e1}}\right)$$

$$SLeff_{22} := SLpulse + 10\cdot\log\left(\frac{\tau_{o2}}{\tau_{e2}}\right)$$

$$SLeff_{23} := SLpulse + 10\cdot\log\left(\frac{\tau_{o2}}{\tau_{e3}}\right)$$

$SLeff_{21} =$

	0
0	104.951
1	110.972
2	114.493
3	116.992
4	118.93
5	120.514
6	121.853
7	123.013
8	124.036
9	124.951
10	125.779
11	126.535
12	127.23
13	127.874
14	128.473

dB

$SLeff_{22} =$

	0
0	97.961
1	103.982
2	107.504
3	110.002
4	111.941
5	113.524
6	114.863
7	116.023
8	117.046
9	117.961
10	118.789
11	119.545
12	120.24
13	120.884
14	121.483

dB

$SLeff_{23} =$

	0
0	94.951
1	100.972
2	104.493
3	106.992
4	108.93
5	110.514
6	111.853
7	113.013
8	114.036
9	114.951
10	115.779
11	116.535
12	117.23
13	117.874
14	118.473

dB

$$SLeff_{31} := SLpulse + 10 \cdot \log\left(\frac{\tau_{o3}}{\tau_{e1}}\right)$$

$SLeff_{31} =$

	0
0	114.951
1	120.972
2	124.493
3	126.992
4	128.93
5	130.514
6	131.853
7	133.013
8	134.036
9	134.951
10	135.779
11	136.535
12	137.23
13	137.874
14	138.473

dB

$$SLeff_{32} := SLpulse + 10 \cdot \log\left(\frac{\tau_{o3}}{\tau_{e2}}\right)$$

$$SLeff_{33} := SLpulse + 10 \cdot \log\left(\frac{\tau_{o3}}{\tau_{e3}}\right)$$

$SLeff_{23} =$

	0
0	94.951
1	100.972
2	104.493
3	106.992
4	108.93
5	110.514
6	111.853
7	113.013
8	114.036
9	114.951
10	115.779
11	116.535
12	117.23
13	117.874
14	118.473

dB

$SLeff_{33} =$

	0
0	104.951
1	110.972
2	114.493
3	116.992
4	118.93
5	120.514
6	121.853
7	123.013
8	124.036
9	124.951
10	125.779
11	126.535
12	127.23
13	127.874
14	128.473

dB

$TS := 10$ dB for a Beam aspect mine from Table 9.3 in Urick.

$Echo := SL_{10} - 2 \cdot TL + TS$

A return echo = Left side of Sonar Equation assuming 50% probability of detection
Ehco = SL-2TL + TS = Noise Masking

Echo =

	0
0	137.136
1	123.301
2	111.965
3	101.652
4	91.899
5	82.501
6	73.347
7	64.373
8	55.535
9	46.805
10	38.163
11	29.593
12	21.083
13	12.625
14	4.211

dB

$Rsens := -44$ dB Receiver Sensitivity for typical transducer looked at.

Transducer_level := Echo + Rsens

Transducer_level =

	0
0	93.136
1	79.301
2	67.965
3	57.652
4	47.899
5	38.501
6	29.347
7	20.373
8	11.535
9	2.805
10	-5.837
11	-14.407
12	-22.917
13	-31.375
14	-39.789

dB re 1V

These are reasonable echo return levels on the transducer.

Power vs Effective Source Level Parametrics for pulse width and cycle time variations.

$$Pe_{11} := 10^{\frac{(SLeff_{11} - 171.5 - 10\cdot\log(\eta e) - DIT)}{10}}$$

$$Pe_{12} := 10^{\frac{(SLeff_{12} - 171.5 - 10\cdot\log(\eta e) - DIT)}{10}}$$

$Pe_{11} =$

	0
0	$7 \cdot 10^{-11}$
1	$2.8 \cdot 10^{-10}$
2	$6.3 \cdot 10^{-10}$
3	$1.12 \cdot 10^{-9}$
4	$1.75 \cdot 10^{-9}$
5	$2.52 \cdot 10^{-9}$
6	$3.43 \cdot 10^{-9}$
7	$4.48 \cdot 10^{-9}$
8	$5.67 \cdot 10^{-9}$
9	$7 \cdot 10^{-9}$
10	$8.47 \cdot 10^{-9}$
11	$1.008 \cdot 10^{-8}$
12	$1.183 \cdot 10^{-8}$
13	$1.372 \cdot 10^{-8}$
14	$1.575 \cdot 10^{-8}$

$$Pe_{13} := 10^{\frac{(SLeff_{13} - 171.5 - 10 \cdot \log(\eta e) - DIT)}{10}}$$

$Pe_{12} =$

	0
0	$1.4 \cdot 10^{-11}$
1	$5.6 \cdot 10^{-11}$
2	$1.26 \cdot 10^{-10}$
3	$2.24 \cdot 10^{-10}$
4	$3.5 \cdot 10^{-10}$
5	$5.04 \cdot 10^{-10}$
6	$6.86 \cdot 10^{-10}$
7	$8.96 \cdot 10^{-10}$
8	$1.134 \cdot 10^{-9}$
9	$1.4 \cdot 10^{-9}$
10	$1.694 \cdot 10^{-9}$
11	$2.016 \cdot 10^{-9}$
12	$2.366 \cdot 10^{-9}$
13	$2.744 \cdot 10^{-9}$
14	$3.15 \cdot 10^{-9}$

$Pe_{13} =$

	0
0	$7 \cdot 10^{-12}$
1	$2.8 \cdot 10^{-11}$
2	$6.3 \cdot 10^{-11}$
3	$1.12 \cdot 10^{-10}$
4	$1.75 \cdot 10^{-10}$
5	$2.52 \cdot 10^{-10}$
6	$3.43 \cdot 10^{-10}$
7	$4.48 \cdot 10^{-10}$
8	$5.67 \cdot 10^{-10}$
9	$7 \cdot 10^{-10}$
10	$8.47 \cdot 10^{-10}$
11	$1.008 \cdot 10^{-9}$
12	$1.183 \cdot 10^{-9}$
13	$1.372 \cdot 10^{-9}$
14	$1.575 \cdot 10^{-9}$

$$Pe_{21} := 10^{\frac{(SLeff_{21} - 171.5 - 10\cdot\log(\eta e) - DIT)}{10}}$$

$$Pe_{22} := 10^{\frac{(SLeff_{22} - 171.5 - 10\cdot\log(\eta e) - DIT)}{10}}$$

$$Pe_{23} := 10^{\frac{(SLeff_{23} - 171.5 - 10\cdot\log(\eta e) - DIT)}{10}}$$

$Pe_{21} =$

	0
0	$7\cdot10^{-9}$
1	$2.8\cdot10^{-8}$
2	$6.3\cdot10^{-8}$
3	$1.12\cdot10^{-7}$
4	$1.75\cdot10^{-7}$
5	$2.52\cdot10^{-7}$
6	$3.43\cdot10^{-7}$
7	$4.48\cdot10^{-7}$
8	$5.67\cdot10^{-7}$
9	$7\cdot10^{-7}$
10	$8.47\cdot10^{-7}$
11	$1.008\cdot10^{-6}$
12	$1.183\cdot10^{-6}$
13	$1.372\cdot10^{-6}$
14	$1.575\cdot10^{-6}$

$Pe_{22} =$

	0
0	$1.4\cdot10^{-9}$
1	$5.6\cdot10^{-9}$
2	$1.26\cdot10^{-8}$
3	$2.24\cdot10^{-8}$
4	$3.5\cdot10^{-8}$
5	$5.04\cdot10^{-8}$
6	$6.86\cdot10^{-8}$
7	$8.96\cdot10^{-8}$
8	$1.134\cdot10^{-7}$
9	$1.4\cdot10^{-7}$
10	$1.694\cdot10^{-7}$
11	$2.016\cdot10^{-7}$
12	$2.366\cdot10^{-7}$
13	$2.744\cdot10^{-7}$
14	$3.15\cdot10^{-7}$

$Pe_{23} =$

	0
0	$7\cdot10^{-10}$
1	$2.8\cdot10^{-9}$
2	$6.3\cdot10^{-9}$
3	$1.12\cdot10^{-8}$
4	$1.75\cdot10^{-8}$
5	$2.52\cdot10^{-8}$
6	$3.43\cdot10^{-8}$
7	$4.48\cdot10^{-8}$
8	$5.67\cdot10^{-8}$
9	$7\cdot10^{-8}$
10	$8.47\cdot10^{-8}$
11	$1.008\cdot10^{-7}$
12	$1.183\cdot10^{-7}$
13	$1.372\cdot10^{-7}$
14	$1.575\cdot10^{-7}$

$$Pe_{31} := 10^{\frac{(SLeff_{31} - 171.5 - 10\cdot\log(\eta e) - DIT)}{10}}$$

$$Pe_{32} := 10^{\frac{(SLeff_{32} - 171.5 - 10\cdot\log(\eta e) - DIT)}{10}}$$

$$Pe_{33} := 10^{\frac{(SLeff_{33} - 171.5 - 10\cdot\log(\eta e) - DIT)}{10}}$$

$Pe_{31} =$

	0
0	$7\cdot10^{-8}$
1	$2.8\cdot10^{-7}$
2	$6.3\cdot10^{-7}$
3	$1.12\cdot10^{-6}$
4	$1.75\cdot10^{-6}$
5	$2.52\cdot10^{-6}$
6	$3.43\cdot10^{-6}$
7	$4.48\cdot10^{-6}$
8	$5.67\cdot10^{-6}$
9	$7\cdot10^{-6}$
10	$8.47\cdot10^{-6}$
11	$1.008\cdot10^{-5}$
12	$1.183\cdot10^{-5}$
13	$1.372\cdot10^{-5}$
14	$1.575\cdot10^{-5}$

$Pe_{32} =$

	0
0	$1.4\cdot10^{-8}$
1	$5.6\cdot10^{-8}$
2	$1.26\cdot10^{-7}$
3	$2.24\cdot10^{-7}$
4	$3.5\cdot10^{-7}$
5	$5.04\cdot10^{-7}$
6	$6.86\cdot10^{-7}$
7	$8.96\cdot10^{-7}$
8	$1.134\cdot10^{-6}$
9	$1.4\cdot10^{-6}$
10	$1.694\cdot10^{-6}$
11	$2.016\cdot10^{-6}$
12	$2.366\cdot10^{-6}$
13	$2.744\cdot10^{-6}$
14	$3.15\cdot10^{-6}$

$Pe_{33} =$

	0
0	$7\cdot10^{-9}$
1	$2.8\cdot10^{-8}$
2	$6.3\cdot10^{-8}$
3	$1.12\cdot10^{-7}$
4	$1.75\cdot10^{-7}$
5	$2.52\cdot10^{-7}$
6	$3.43\cdot10^{-7}$
7	$4.48\cdot10^{-7}$
8	$5.67\cdot10^{-7}$
9	$7\cdot10^{-7}$
10	$8.47\cdot10^{-7}$
11	$1.008\cdot10^{-6}$
12	$1.183\cdot10^{-6}$
13	$1.372\cdot10^{-6}$
14	$1.575\cdot10^{-6}$

$$P_{10} := 10^{\frac{(SL_{10}-171.5-10\cdot\log(\eta e)-DIT)}{10}}$$

$P_{10} =$

	0
0	$7\cdot10^{-6}$
1	$2.8\cdot10^{-5}$
2	$6.3\cdot10^{-5}$
3	$1.12\cdot10^{-4}$
4	$1.75\cdot10^{-4}$
5	$2.52\cdot10^{-4}$
6	$3.43\cdot10^{-4}$
7	$4.48\cdot10^{-4}$
8	$5.67\cdot10^{-4}$
9	$7\cdot10^{-4}$
10	$8.47\cdot10^{-4}$
11	$1.008\cdot10^{-3}$
12	$1.183\cdot10^{-3}$
13	$1.372\cdot10^{-3}$
14	$1.575\cdot10^{-3}$

Transducer Power for several commercially available transducers

The following power levels were calculated from commercially available transducer data sheets assuming a 2% duty cycle.

$P_{KT08} := 1.923 10^{-3}$ W

$P_{KT18} := 3.82 \times 10^{-3}$ W

$P_{KR18} := 2.714 \times 10^{-3}$ W

$P_{KT25} := 4.825 \times 10^{-3}$ W

$P_{P9000} := 7.481 \times 10^{-4}$ W

$P_{ww.\mu AUV} := 9.00 10^{-5}$ W Wulrich Wave Acoustics Comms Variant

Plot of Acoustic Power versus Range Parametrics

The plot in Figure 1 compares the Power for several different radiated acoustic pressures. Pr is the primary curve with its +/- 15% error curves plotted. Pr is calculated at a p=10dynes/square cm. It is compared against the Pr5 (p=5 dynes/square cm and Pr1 (p=1 dyne/square cm. The commercial transducers cited above have power levels consistent with the Pr levels. The source levels for these transducers are also consistent with the calculated source levels plotted in Figure 2.

Figure 1 - Acoustic Power vs Range

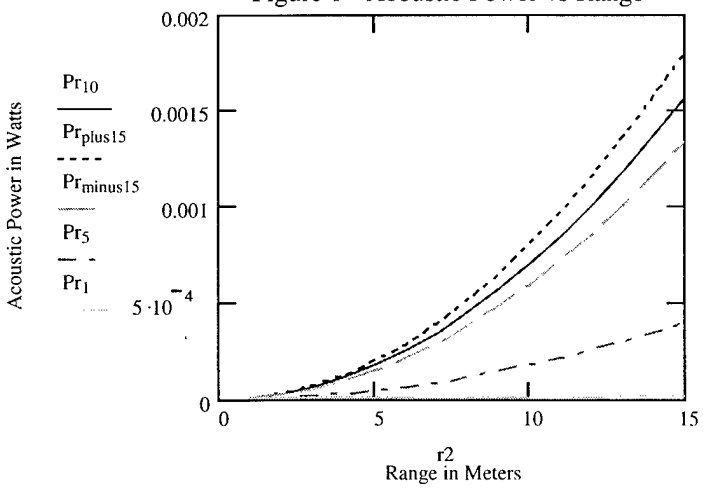

Source Level for Commercially Available Transducers

The following are source levels for commercially available transducers in seawater.

$SL_{KT08} := 162$ dB

$SL_{KT18} := 170$ dB

$SL_{KT25} := 177$ dB

$SL_{P9000} := 162$ dB

Figure 2 - Radiated Pressure Parametric

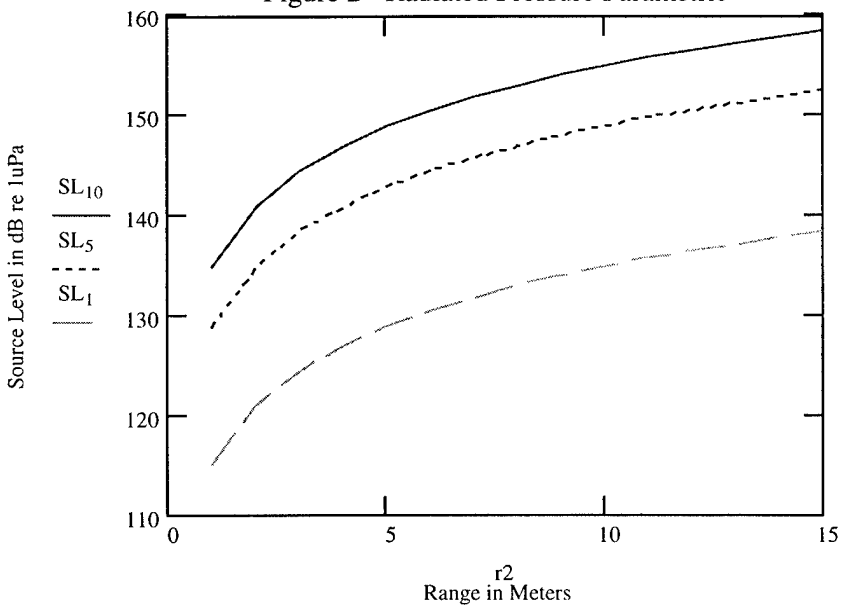

The source level curves plotted below is the source level for the primary curve SL compared to the effective source levels for parametrics of Pulse Width and Cycle Time. The plot SLeff11 is for pulse width $\tau o1$ and cycle time $\tau e1$. Figure 3, 4, and 5 holds pulse width (τo) constant and varies cycle time (τe). Figure 6, 7, and 8 varies pulse width (τo) and holds cycle time (τe) constant.

Figure 3 - Cycle Time Parametric 1

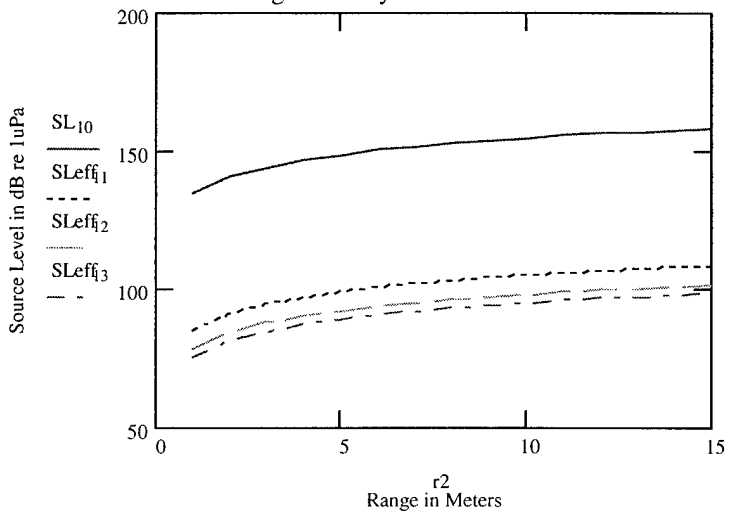

Figure 4 - Cycle Time Parametric 2

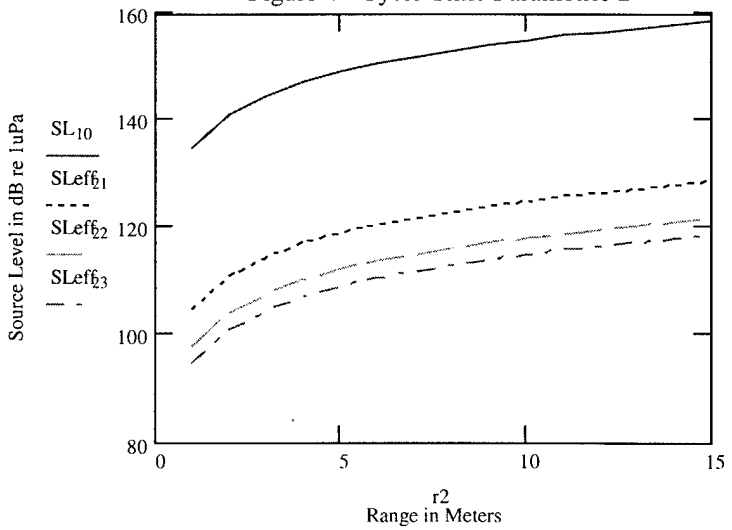

Figure 5 - Cycle Time Parametric 3

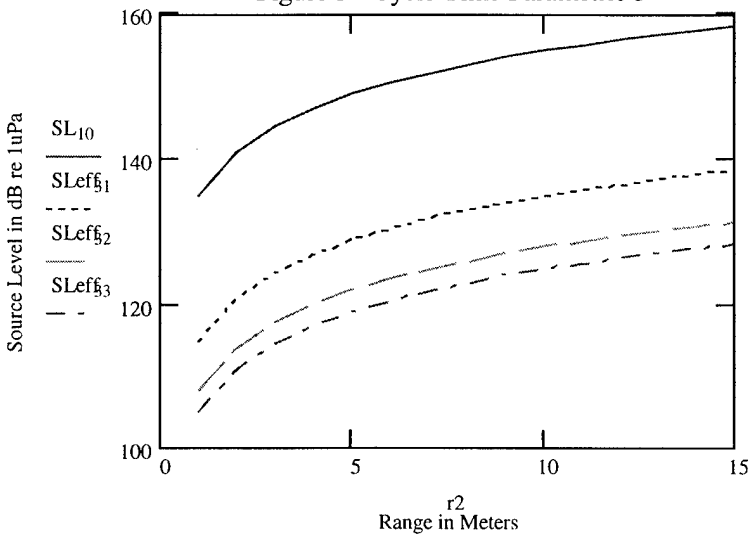

Figure 6 - Pulse Width Parametric1

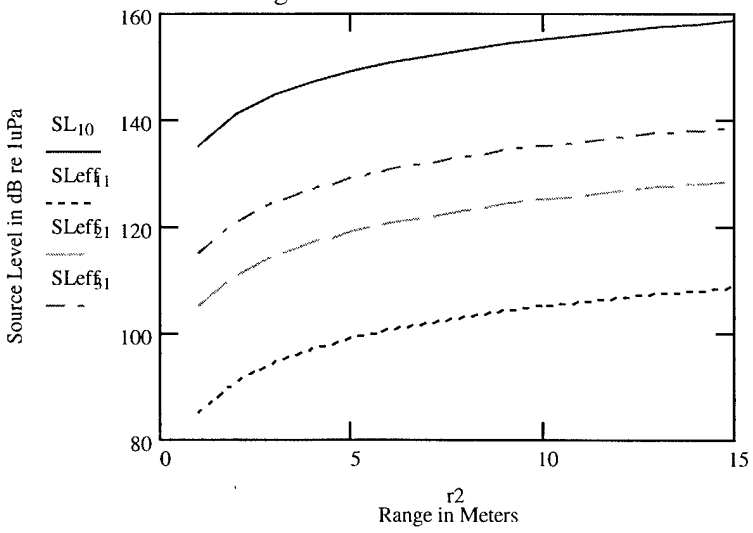

Figure 7- Pulse Width Parametric 2

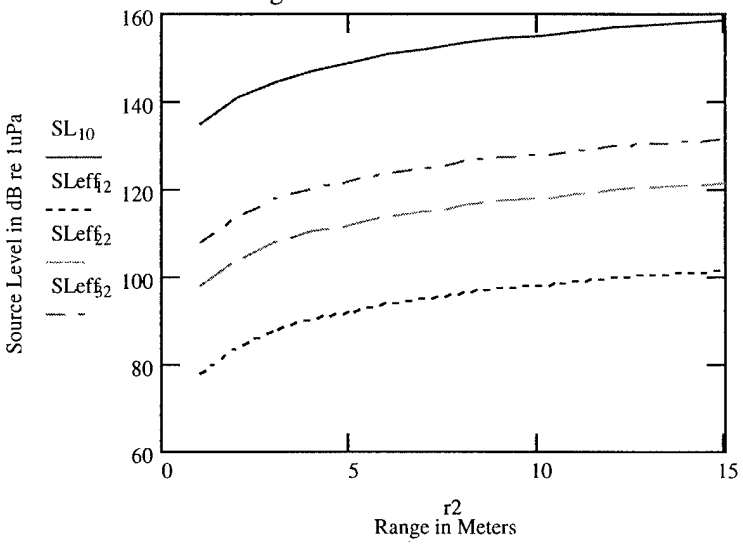

Figure 8 - Pulse Width Parametric 3

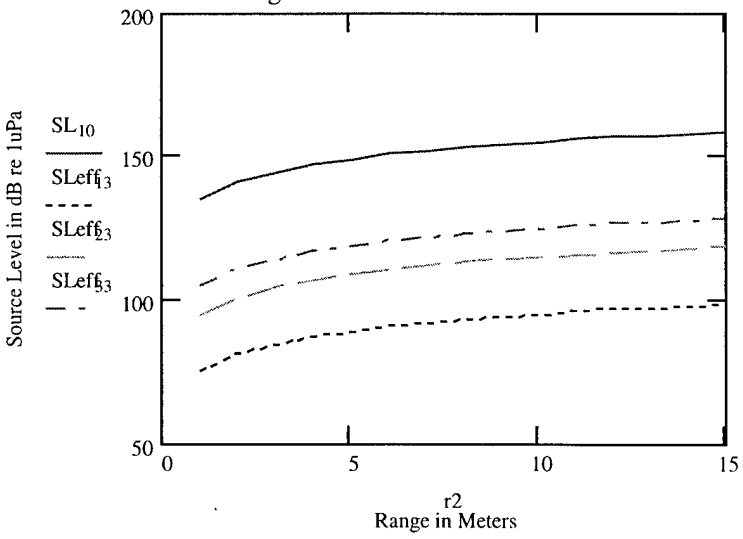

Figure 9: Theoretical Power - 15 m Range

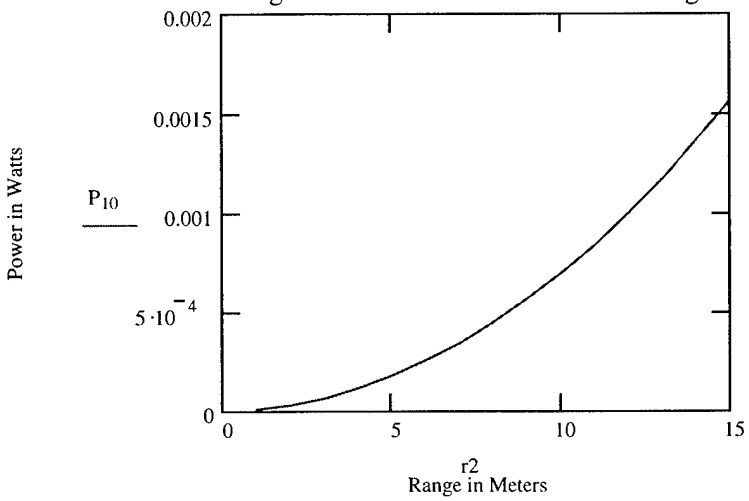

Figure 10: Power for 1 bit & vary PRR

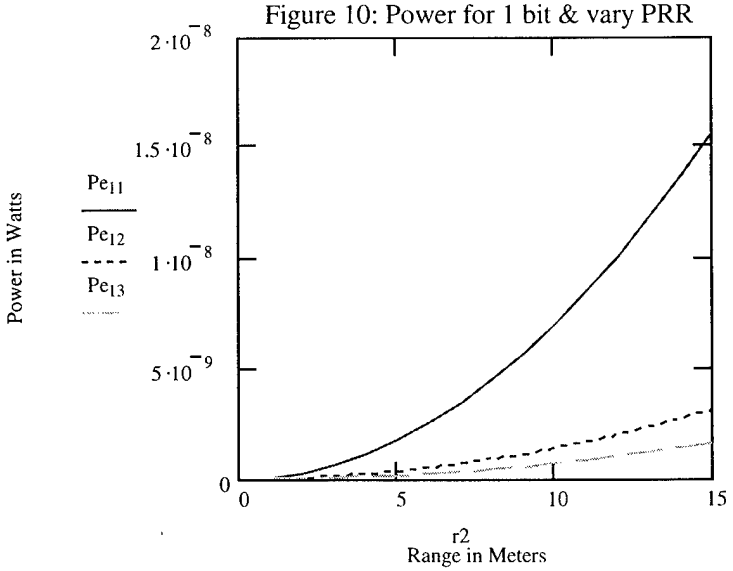

Figure 11: Power for 100 bits vary PRR

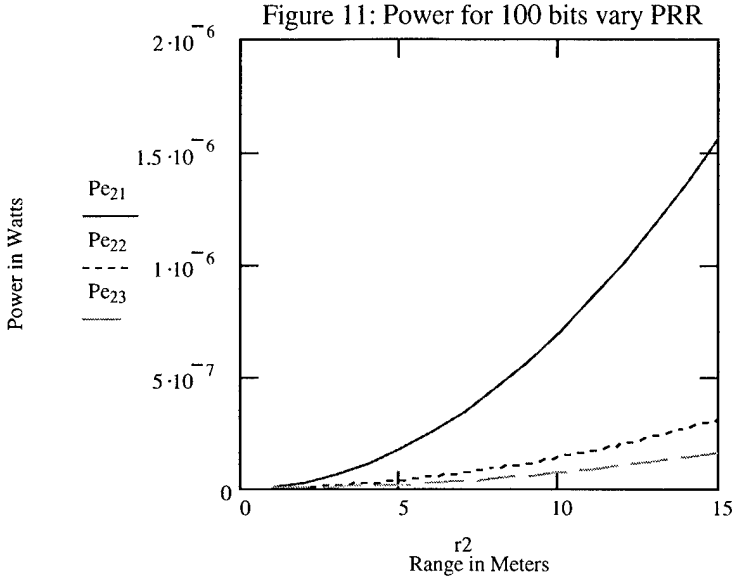

Figure 12: Power for 1000 bits vary PRR

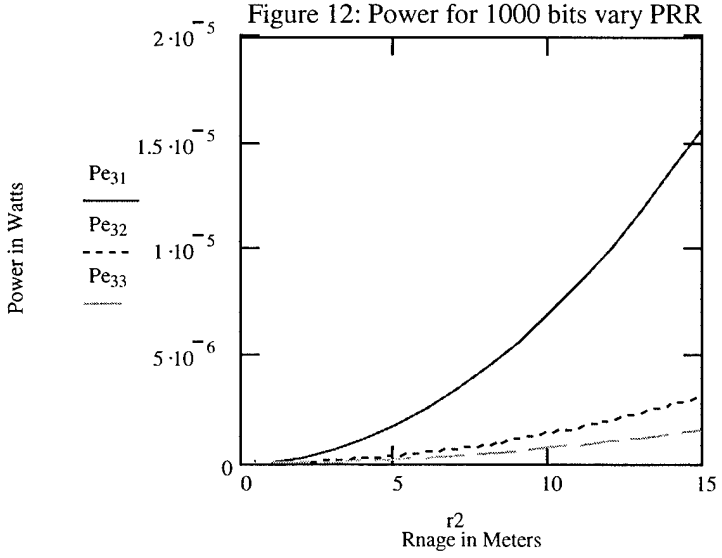

Figure 13: Power for 1 sec PRR vary PW

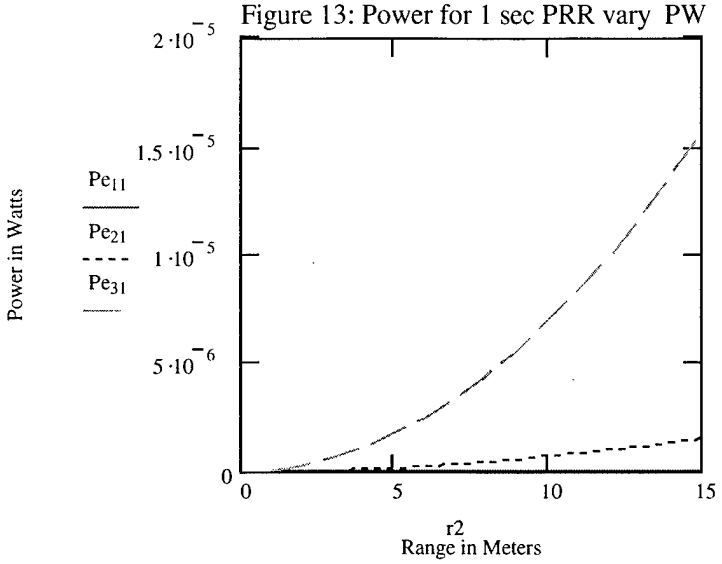

Figure 14: Power for 5 sec PRR vary PW

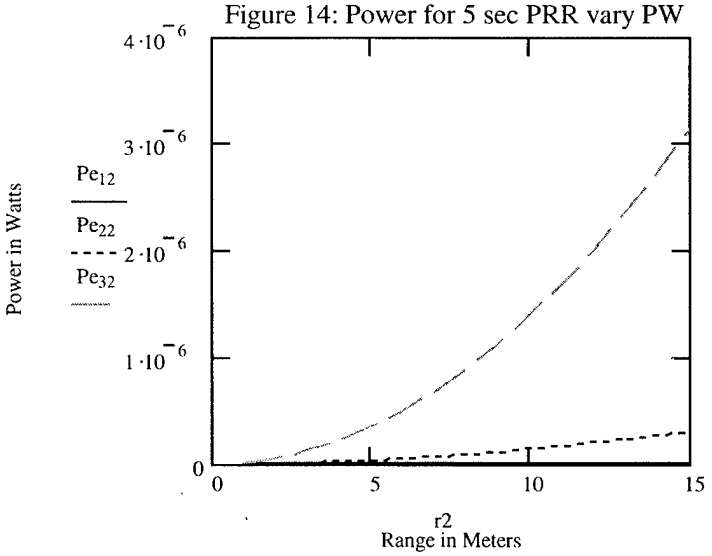

Figure 15: Power for 10 sec PRR vary PW

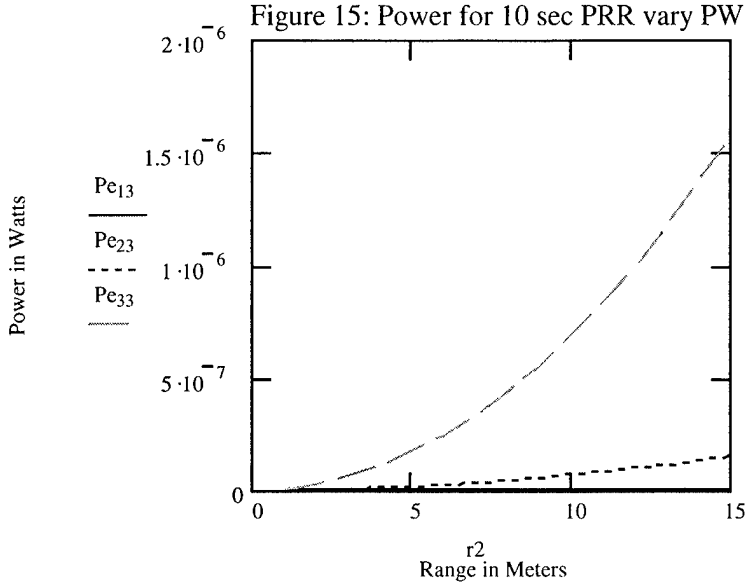

Commercial Transducer Power Calculations

AIRMAR ATK200 Transducer

operating Frequency 200 kHz +/- 4%

$c := 5700$ pF

$f := 200\,10^3$ Hz

$Rp := 300$ Ω

$Vpp := 500$ V peak to peadk

$E := \frac{Vpp}{2.83}$ V rms

$E = 176.678$ V rms

$Po := \frac{E^2}{Rp}$

$Po = 104.051$ W Not suitable for our application

Polaroid 6500 Sonar Ranging Module

$Vdc := 7$ V

$i := 100$ mA

$ip := 2000$ mA

$Ppulse := Vdc \cdot ip \cdot 10^{-3}$

$Ppulse = 14$ W

$P := Vdc \cdot i \cdot 10^{-3}$

$P = 0.7$ W

Average continuous power 1.15 W from 0 - 25 degrees C

Polaroid Closed Face Piezoelectric K series Transducers

40KT08

$C_{KT08} := 1700\,10^{-12}$ F

$f_{KT08} := 40 \cdot 10^{3}$ Hz

$E_{KT08} := 15$ V rms

$I_{KT08} := 2 \cdot \pi \cdot f_{KT08} \cdot C_{KT08} \cdot E_{KT08}$

$I_{KT08} = 6.409 \times 10^{-3}$ A

$P_{KT08} := I_{KT08} \cdot E_{KT08} \cdot .02$ Assuming a 2% duty cycle

$P_{KT08} = 1.923 \times 10^{-3}$ W

40KT18

$C_{KT18} := 1900\,10^{-12}$ F

$f_{KT18} := 40\cdot 10^{3}$ Hz

$E_{KT18} := 20$ V rms

$I_{KT18} := 2\cdot\pi\cdot f_{KT18}\cdot C_{KT18}\, E_{KT18}$

$I_{KT18} = 9.55\times 10^{-3}$ A

$P_{KT18} := I_{KT18}\cdot E_{KT18}\cdot .02$

$P_{KT18} = 3.82\times 10^{-3}$ W

40KR18

$C_{KR18} := 2400\,10^{-12}$ F

$f_{KR18} := 40\cdot 10^{3}$ Hz

$E_{KR18} := 15$ V rms

$I_{KR18} := 2\cdot\pi\cdot f_{KR18}\cdot C_{KR18}\cdot E_{KR18}$

$I_{KR18} = 9.048\times 10^{-3}$ A

$P_{KR18} := I_{KR18}\cdot E_{KR18}\cdot .02$

$P_{KR18} = 2.714\times 10^{-3}$ W

40KT25

$C_{KT25} := 2400 \cdot 10^{-12}$

$f_{KT25} := 40 \cdot 10^{3}$ Hz

$E_{KT25} := 20$ V rms

$I_{KT25} := 2 \cdot \pi \cdot f_{KT25} \cdot C_{KT25} \cdot E_{KT25}$

$I_{KT25} = 0.012$ A

$P_{KT25} := I_{KT25} \cdot E_{KT25} \cdot .02$

$P_{KT25} = 4.825 \times 10^{-3}$ W

Poloroid 9000

$C_{P9000} := 2.7 \cdot 10^{-9}$

$f_{P9000} := 45 \cdot 10^{3}$ Hz

$E_{P9000} := 7$ V rms

$I_{P9000} := 2 \cdot \pi \cdot f_{P9000} \cdot C_{P9000} \cdot E_{P9000}$

$I_{P9000} = 5.344 \times 10^{-3}$ A

$P_{P9000} := I_{P9000} \cdot E_{P9000} \cdot .02$

$P_{P9000} = 7.481 \times 10^{-4}$ W

Wulich Wave Dolphin Diver Wrist Watch Acoustic Comm Unit

Homing Range 1000m

Comms Range 500m (calm seas)

$E_{ww} := 6$ four AA 1.5 volt Alkaline Batteries - 9 hour life

$I_{ww} := 150 \cdot 10^{-3}$ A

$P_{ww} := I_{ww} \cdot E_{ww}$

$P_{ww} = 0.9$ W This could be reduced by reducing the range 1000m down to 10m consistent with the MicroAUV

$$P_{ww.\mu AUV} := \frac{10^2 \cdot P_{ww}}{1000^2}$$

$P_{ww.\mu AUV} = 9 \times 10^{-5}$ W